

NAVAL POSTGRADUATE SCHOOL

Monterey, California



THESIS

**RESPONSE OF THE SOUTH CHINA SEA
TO FORCING BY TROPICAL CYCLONE
ERNIE (1996)**

by

Joseph M. Veneziano

March 1998

Thesis Advisor:

Peter C. Chu

Co-Advisor:

Michael J. Carron

19980526 024

Approved for public release; distribution is unlimited.

REPORT DOCUMENTATION PAGE

Form Approved OMB No. 0704-0188

Public reporting burden for this collection of information is estimated to average 1 hour per response, including the time for reviewing instruction, searching existing data sources, gathering and maintaining the data needed, and completing and reviewing the collection of information. Send comments regarding this burden estimate or any other aspect of this collection of information, including suggestions for reducing this burden, to Washington Headquarters Services, Directorate for Information Operations and Reports, 1215 Jefferson Davis Highway, Suite 1204, Arlington, VA 22202-4302, and to the Office of Management and Budget, Paperwork Reduction Project (0704-0188) Washington DC 20503.

1. AGENCY USE ONLY <i>(Leave blank)</i>	2. REPORT DATE	3. REPORT TYPE AND DATES COVERED Master's Thesis	
4. TITLE AND SUBTITLE Response of the South China Sea to Forcing by Tropical Cyclone Ernie (1996)			5. FUNDING NUMBERS
6. AUTHOR(S) Joseph M. Veneziano			
7. PERFORMING ORGANIZATION NAME(S) AND ADDRESS(ES) Naval Postgraduate School Monterey CA 93943-5000			8. PERFORMING ORGANIZATION REPORT NUMBER
9. SPONSORING/MONITORING AGENCY NAME(S) AND ADDRESS(ES)			10. SPONSORING/MONITORING AGENCY REPORT NUMBER
11. SUPPLEMENTARY NOTES The views expressed in this thesis are those of the author and do not reflect the official policy or position of the Department of Defense or the U.S. Government.			
12a. DISTRIBUTION/AVAILABILITY STATEMENT Approved for public release; distribution is unlimited.			12b. DISTRIBUTION CODE
13. ABSTRACT <i>(maximum 200 words)</i> The South China Sea (SCS) response to forcing by Tropical Cyclone Ernie (1996) was studied numerically using the Princeton Ocean Model (POM) with 20 km horizontal resolution and 23 sigma levels conforming to a realistic bottom topography. A fourteen day experiment was conducted using a wind model that allowed for temporal variations of its translational speed, size and intensity. Restoring type salt and heat fluxes were used along with seasonal inflow/outflow at the open boundaries. The POM adequately simulated ocean responses to tropical cyclone forcing. Near-surface ocean responses simulated by the POM included strong asymmetrical divergent currents with near-inertial oscillations, significant sea surface temperature cooling, biased to the right of the storm track, and sea surface depressions in the wake of the storm. Subsurface responses included intense upwelling and cooling at the base of the mixed layer to the right of the storm track. Several unique features, caused by coastal interactions with storm forcing, were also simulated by the model. Along the coast of Luzon a subsurface alongshore jet was formed, a warm anomaly off the northern tip of Luzon was significantly enhanced by surface layer convergence and storm surges simulated along the coasts of Luzon and Vietnam.			
14. SUBJECT TERMS South China Sea, numerical simulation, Tropical Cyclone Ernie (1996), ocean response to tropical cyclone forcing			15. NUMBER OF PAGES 181
			16. PRICE CODE
17. SECURITY CLASSIFICATION OF REPORT Unclassified	18. SECURITY CLASSIFICATION OF THIS PAGE Unclassified	19. SECURITY CLASSIFICATION OF ABSTRACT Unclassified	20. LIMITATION OF ABSTRACT UL

NSN 7540-01-280-5500

Standard Form 298 (Rev. 2-89)
Prescribed by ANSI Std. Z39-18 298-102

Approved for public release; distribution is unlimited.

**RESPONSE OF THE SOUTH CHINA SEA TO
FORCING BY TROPICAL CYCLONE ERNIE (1996)**

Joseph M. Veneziano

Lieutenant Commander, United States Navy

B.S., University of Florida, 1987

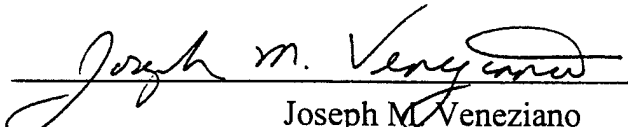
Submitted in partial fulfillment
of the requirements for the degree of

**MASTER OF SCIENCE IN PHYSICAL OCEANOGRAPHY AND
METEOROLOGY**

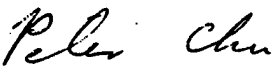
from the

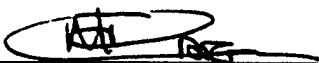
NAVAL POSTGRADUATE SCHOOL
March 1998

Author:


Joseph M. Veneziano

Approved by:


Peter C. Chu, Thesis Advisor


Michael J. Carron, Co-Advisor


Robert H. Bourke, Chairman
Department of Oceanography

ABSTRACT

The South China Sea (SCS) response to forcing by Tropical Cyclone Ernie (1996) was studied numerically using the Princeton Ocean Model (POM) with 20 km horizontal resolution and 23 sigma levels conforming to a realistic bottom topography. A fourteen day experiment was conducted using a wind model that allowed for temporal variations of its translational speed, size and intensity. Restoring type salt and heat fluxes were used along with seasonal inflow/outflow at the open boundaries. The POM adequately simulated ocean responses to tropical cyclone forcing. Near-surface ocean responses simulated by the POM included strong asymmetrical divergent currents with near-inertial oscillations, significant sea surface temperature cooling, biased to the right of the storm track, and sea surface depressions in the wake of the storm. Subsurface responses included intense upwelling and cooling at the base of the mixed layer to the right of the storm track. Several unique features, caused by coastal interactions with storm forcing, were also simulated by the model. Along the coast of Luzon a sub-surface alongshore jet was formed, a warm anomaly off the northern tip of Luzon was significantly enhanced by surface layer convergence and storm surges simulated along the coasts of Luzon and Vietnam.

TABLE OF CONTENTS

I. INTRODUCTION	1
II. THE SOUTH CHINA SEA	5
A. GEOGRAPHY	5
B. PHYSICAL OCEANOGRAPHY	6
1. Water Masses	6
2. Surface Current Systems	7
a. Summer Pattern	8
b. Winter Pattern	9
3. Eddies	10
4. Upwelling	11
III. CLIMATOLOGY	19
A. MONSOONAL WIND FLOW OVER THE SCS	19
1. Southwest Monsoon	19
2. Northeast Monsoon	20
B. MONSOONAL INFLUENCE ON SCS TROPICAL CYCLONES	22
1. Tropical Cyclone Formation	22
2. Tropical Cyclone Movement	25
IV. SCS WIND FIELD MODEL	31
A. TROPICAL STORM ERNIE (1996)	31
B. SCS TROPICAL CYCLONE WIND FIELD DECOMPOSITION	32
1. Carr and Elsberry Tropical Cyclone Wind Profile Model	33
2. SCS Tropical Cyclone Wind Field Model	37
3. Tropical Cyclone Parameters Determination	39
C. SCS WIND MODEL VERIFICATION	40
1. NSCAT and SCS Wind Model Comparisons	41
V. PRINCETON OCEAN MODEL	55
A. MODEL FEATURES	55
1. Sigma Coordinate System	56
2. Finite Differencing	57
3. Mode Splitting	59
4. Level Two Turbulence Closure	59
B. MODEL GOVERNING EQUATIONS	60
1. Continuity Equation	60
2. Momentum Equations	61
3. Temperature and Salinity Conservations Equations	61

4.	Subgrid Scale Horizontal Mixing Processes	62
C.	INITIAL CONDITIONS AND BOUNDARY CONDITIONS	63
1.	Initial Conditions and Initialization	63
2.	Bottom Boundaries	63
3.	Forcing	64
a.	Atmospheric forcing	64
b.	Lateral boundary forcing	66
VI.	OCEAN RESPONSE TO TROPICAL CYCLONE FORCING	69
A.	OBSERVATIONS OF OCEAN RESPONSES	69
1.	Ocean Thermal Structure	69
a.	Sea Surface Temperature (SST) Cooling	69
b.	Subsurface Thermal Structure Modification	70
2.	Upper Ocean Current	71
a.	Mixed Layer Currents	71
b.	Thermocline Currents	72
c.	Upwelling and Downwelling	73
3.	Sea Surface Elevation	74
a.	Inverse Barometer Effect	74
b.	Wind Stress Curl Effect	75
c.	Wind Stress Divergence Effect	76
d.	Barotropic Current Effect	76
e.	Baroclinic Current Effect	77
B.	NUMERICAL MODELING OF OCEAN RESPONSES	77
1.	Simulations of Ocean Responses Using Level Models	78
a.	Chang (1985) Ocean Model	79
b.	Shay et al. (1990) Ocean Model	79
c.	Price et al. (1994) Ocean Model	80
VII.	NUMERICAL SIMULATION OF SCS RESPONSE TO TROPICAL CYCLONE ERNIE (1996)	87
A.	NUMERICAL SIMULATION	88
1.	Pre-experimental Stage	88
a.	Model Initial State Verification	88
2.	Numerical Simulation	90
B.	ANALYSIS SCHEME	90
1.	Analysis Areas	91
a.	Area One	91
b.	Area Two	91
c.	Area Three	92
C.	SIMULATION RESULTS	92
1.	Overview	92
2.	Area One	95

3.	Area Two	100
4.	Area Three	103
D.	SENSITIVITY STUDY	106
VIII. CONCLUSIONS		157
LIST OF REFERENCES		161
APPENDIX. TROPICAL STORM ERINE (1996) DATA		167
INITIAL DISTRIBUTION LIST		169

I. INTRODUCTION

The South China Sea (SCS), and the nations on its borders, is a region of strategic political and military importance to the United States and its allies. As such, the United States Naval Oceanographic Office (NAVOCEANO) has been tasked with the development of an ocean forecasting capability for this region. Since the SCS is a semi-enclosed sea, with limited open boundaries, numerical modeling techniques are well suited to solve the forecasting problem. Also due to its semi-enclosed nature, the SCS is subject to high spatial and temporal variability from external forcing factors. One significant source of oceanic forcing is the tropical cyclones that routinely affect the region.

The major oceanic response produced by the passage of a tropical cyclone is a significant upper oceanic layer cooling, which researchers have observed in many temperature data sets (Fisher, 1958; Hazelworth, 1968; Black, 1983; Pudov et al., 1978) and numerical studies (Chang, 1985; Shay et al., 1990; Price et al., 1994). This cooling occurs primarily due to turbulent mixing in the upper oceanic layer, which produces mixed layer deepening by entraining cooler thermocline water. Other oceanic responses to tropical cyclones are strong currents and storm surges. All these processes have the potential to affect maritime and coastal operations dramatically. Being able to predict these oceanic responses is therefore critical. To predict these responses a thorough understanding of the processes that produce them is necessary. One means of accomplishing such an understanding is through the retrieval and thorough analysis of

oceanographic data.

The collection of that oceanographic data is difficult, expensive and usually accomplished on a limited spatial scale however. Additionally, the deployment of large arrays of instruments in the path of a tropical cyclone is not feasible due to the often erratic track of the storm. Therefore, the ocean processes which produce these effects are impossible to observe on a large enough scale to gain significant insight into their spatial structure and temporal variability. Ocean sensors have made chance sets of observations when tropical cyclones have fortuitously tracked over an already deployed array of instruments, such as Hurricane Eloise in the Gulf of Mexico (Johnson and Withee, 1978). Researchers have also accomplished limited sampling before and after the passage of a storm, as was done during the special project USSR TYPHOON '75 (Pudov et al., 1978). Satellite instruments also routinely retrieve ocean surface information, from which limited subsurface ocean data may be inferred. While these data sets are sparse, they have increased the knowledge of how tropical cyclones change the oceanic environment. This has allowed researchers to develop and partially verify theoretical models of tropical cyclone-forced oceanic processes. Nevertheless, they do not provide information on the broad area, three-dimensional, multi variable ocean structure. With such information and ocean modeling techniques, however, we can obtain an insight into that structure.

To that end, this thesis will evaluate the SCS Princeton Ocean Model's (POM) ability to capture the extreme dynamic responses produced by a moving tropical cyclone over the region. Previous studies have displayed the ability of the SCS POM to correctly model the SCS. Initial usage of the SCS POM includes Li (1994) and Chu et al. (1994,

1996), who successfully simulated the variability of the SCS circulation with the changing monsoonal regimes. This study will extend this prior work by forcing the SCS POM with a model wind field of Tropical Cyclone Ernie (1996). The study will examine the model's capability to simulate the ocean responses to tropical cyclone forcing. A detailed analysis of the modifications to the sea surface temperature, elevation and currents, as well as the subsurface temperature and current structure will be done. This analysis will be compared with previous observational and numerical modeling studies. Along with further validation of the SCS POM, a better insight into how a tropical cyclone modifies the ocean environment and the processes involved may be realized.

II. THE SOUTH CHINA SEA

Ocean responses to tropical cyclone forcing vary according to both the physical and thermal structure of the basin. The storm's effects are dependent on the water depth, the proximity to land barriers, the pre-storm water mass stability and, most significantly, nonlinear processes that occur in shelf regions. Therefore, an examination of ocean responses generated by the tropical cyclone requires an understanding of the bathymetry, normal water mass and velocity structures in the SCS.

A. GEOGRAPHY

The SCS is one of the largest marginal seas of the Western Pacific Ocean, extending across both tropical and subtropical zones and encompasses a total surface area of $3.5 \times 10^6 \text{ km}^2$. The region is located between the Asian landmass to the west, the Philippine Islands and Borneo to the east and China and Taiwan to the north (Figure 2.1).

Connections to the SCS with the East China Sea, the Pacific Ocean, the Sulu Sea, the Java Sea and the Indian Ocean are through the Taiwan Strait, Bashi Channel, Balabac Strait, Karimata Strait and Malacca Strait, respectively. All these connections are narrow and shallow, except the Bashi Channel whose maximum depth is about 2000 m. Consequently, the SCS is considered a semi-enclosed basin.

Bottom topography of the basin is quite complicated. Wide continental shelves

appear in the northwest and southwest of the basin and steep slopes in the central portion, framing a deep, bowl-shaped depression. Many reef islands and underwater plateaus are scattered throughout (Figure 2.2). The continental shelf that extends from the Gulf of Tonkin to the Taiwan Strait is consistently about 70 m deep, and averages 150 km in width from the shoreline. A central deep depression with depths greater than 4000 m, extends 1900 km along a northeast to southwest axis and is approximately 1100 km wide. The Sunda Shelf is the submerged connection between Southeast Asia, Malaysia, Sumatra, Java and Borneo and is 100 m deep in its center; the Gulf of Thailand is about 70 m deep in its central part (Li and Li, 1994).

B. PHYSICAL OCEANOGRAPHY

1. Water Masses

Data on water masses of the South China Sea is limited (Fan et al., 1988). Waters from the Western Pacific enter the northern SCS through the Bashi channel and after mixing and modification, form distinct water masses. Continental fresh water runoff is also very significant. Su and Weng (1994) classified eight water masses in the northern SCS. They grouped these water masses into three classes: (I) runoff diluted type of Nearshore Diluted Water Mass (F); (ii) the shallow sea modified type composed of Coastal Mixed Water (M), Warm Surface Water Mass (WS), Surface Water Mass (S) and Surface-Subsurface Mixed Water Mass (SU); and (iii) the deep sea type, composed of

Subsurface Water Mass (U), Subsurface-Intermediate Mixed Water Mass (UI) and Intermediate Water Mass (I). Distributions of these water masses at the surface are nearly parallel to the coastline (Figure 2.3).

WS and S both originate from West Pacific Surface Water. Various meteorological conditions modify this water and ultimately generate the high temperature and low salinity WS water and low temperature, low salinity S water. Mixing modifies the West Pacific Subtropical Subsurface Water to form SU water, which is similar to S water. U water, distributed at approximately 150 m depth, retains the high salinity layer of West Pacific water. UI is the interface between the deep high salinity layer and low salinity surface layer. I is an oceanic type water mass with the least modification from its source water mass. Low salinity, distributed down to 700 m, characterizes this water mass. F is a mixture of runoff and nearshore water. M undergoes the largest modification, mixing with SU, WS and S respectfully in varying seasons. Table 1.1 lists the characteristics of the water masses.

2. Surface Current Systems

The seasonally varying monsoonal wind predominately drives the SCS surface current circulation pattern.

Water Mass	Feb.	May	Aug.	Nov.
F T(°C) Salinity		25.5-27.8 <30.0	29.0-30.5 <30.0	
M T(°C) Salinity	13.2-16.0 31.20-33.60	22.5-27.6 31.16-33.80	28.9-30.3 33.03-32.91	21.3-24.4 31.32-34.02
WS T(°C) Salinity	22.3-24.4 34.08-34.67	26.2-30.0 33.90-34.69	28.0-30.1 33.03-34.40	25.5-26.1 33.68-33.93
S T(°C) Salinity	20.4-22.3 34.43-34.80	22.2-26.2 33.85-34.62	23.5-28.0 33.65-34.62	22.5-25.5 33.97-34.60
SU T(°C) Salinity	17.5-20.4 34.18-34.75	19.8-22.2 34.16-34.71	21.0-23.5 34.32-34.70	19.0-22.5 34.42-34.76
U T(°C) Salinity	15.5-17.5 34.28-34.78	14.5-19.8 34.44-34.88	15.2-21.0 34.35-34.81	14.5-19.0 34.50-34.78
UI T(°C) Salinity	11.0-15.5 34.46-34.60	10.0-14.5 34.40-34.70	11.0-15.2 34.41-34.79	11.0-14.5 34.42-34.62
I T(°C) Salinity		5.3-10.0 34.33-34.64	5.6-11.0 34.34-34.52	6.4-11.0 34.30-34.50

Table 2.1. Ranges of Temperature and Salinity of Water Masses in the northern South China Sea (from Su and Weng, 1994).

a. Summer Pattern

The summer (southwest) monsoon forces a wide, uniform northeasterly flowing surface current over most of the basin (Figure 2.4). Westward intensification generates a strong current along the western side of the basin, off the coasts of Thailand and Vietnam. The larger part of the surface flow passes south of Taiwan and merges with the northerly flowing Kurishio; a smaller amount flows north through the Taiwan Strait. Wyrtki (1961) reported the existence of a counter current on the eastern side of the basin, with a southwesterly flow along the Borneo coast. This flow turns back northerly in the region of Natuna Island, in the southern SCS, forming an anticyclonic gyre. Wyrtki

hypothesizes that an insufficient supply of water into the basin from the Java Sea produces this gyre. In September these movements decrease and in October the northeast monsoon begins blowing with considerable strength, resulting in the complete reversal of the current fields.

b. Winter Pattern

The mean northeast wind stress over the Western Pacific deflects the water masses of the North Equatorial Current to the south, causing them to enter the SCS through the Bashi Channel. Water from the East China Sea moves southerly through the Taiwan Strait and enters the SCS. This southerly moving water turns southwesterly and flows along the coast of China and Vietnam, with a remarkable westward intensification (Wyrtki, 1961). In the center of the SCS a northerly flowing counter current develops over about 10 degrees of latitude (Figure 2.5).

During the early part of the northeast monsoon not all of the southerly flowing water can flow into the Java Sea, since the southeast monsoon is still blowing weakly over this region. This situation produces a northward flowing counter current along the coast of Borneo. The water flows as far north as Luzon, where it turns southerly and merges into the main current, forming a closed cyclonic gyre.

During December the northwest monsoon is fully developed and the currents are their strongest, exceeding 100 cm/s off the coast of Vietnam. The northerly flowing counter current in the central SCS is located farther to the east, due to the

strength of the main current. A weak southerly flowing coastal counter current forms along the northwest coast of Borneo.

3. Eddies

The monsoonal flow regime also influences eddies in the SCS. Eddies are predominately cyclonic during the winter northeast monsoon and anticyclonic in the summer southeast monsoon. Studies from the South China Sea Institute of Oceanology (SCSIO) (1985) point out that during the early stages of the northeast monsoon there is a cold eddy, a cyclonic circulation, which forms off the central coast Vietnam. Many studies have reported that an anticyclonic eddy appears in the central SCS during the late spring season (Chu and Chang, 1995; Tseng, 1995). Soong et al., (1995) also detected a cyclonic eddy in the central SCS during December 29, 1994 to January 5, 1994, through analysis of TOPEX/Poseidon data.

A possible explanation for the seasonality of cyclonic and anticyclonic eddies is a combined wind-topography effect (Chu, 1997). Chu suggests that the bowl-type bottom topography of the SCS basin provides a favorable condition for the formation of anticyclonic eddies in the central SCS during the spring. From late winter to early spring a surface anticyclone appears over the SCS (Cheang, 1987). The anticyclonic wind stress generates Ekman downwelling in the central part of the bowl and mass balance causes upwelling near the boundaries. This circulation results in the warming of the central part of the bowl and a cooling of its boundaries. During the spring the northwest monsoon

decays and the SCS enters a period of generally clear sky conditions, bringing increased solar radiation that warms the sea surface. Surface air pressure lowers because of this enhanced warming, and a surface cyclone is produced. This cyclonic wind stress then generates Ekman upwelling in the central basin and the formation of a cold pool. Again, through mass balance, the boundaries of the bowl become warmed due to downwelling (Chu et al., 1997).

Tropical cyclones that move through the region also produce large scale eddies with significant energy. During the passage of Typhoon Georgia in 1983 an anchored buoy station south of Hong Kong recorded the only existing data of sub-surface currents generated during the passage of a tropical cyclone over the SCS. The analysis of this data (Ke et al., 1987) indicated that the maximum current speed occurred six to eight hours after the passage of the storm's maximum winds and that the influence of the tropical cyclone disappeared in three to four days.

4. Upwelling

Upwelling in the SCS occurs extensively, is strong in strength and is usually associated with cold cyclonic eddies that occur during the winter northwest monsoon. Huang and Wang (1994) reported that upwelling occurred in December 1984, during the winter northeast monsoon, in the coastal area of eastern Hainan Island. In summer, upwelling occurs more often in the nearshore areas near Hong Kong, off the eastern coast of Hainan Island, and off central Vietnam (Huang and Wang, 1994). The northeast

current flow along the coast produced by the summer southeast monsoon generates offshore water mass movement, due to Ekman transport and upwelling.

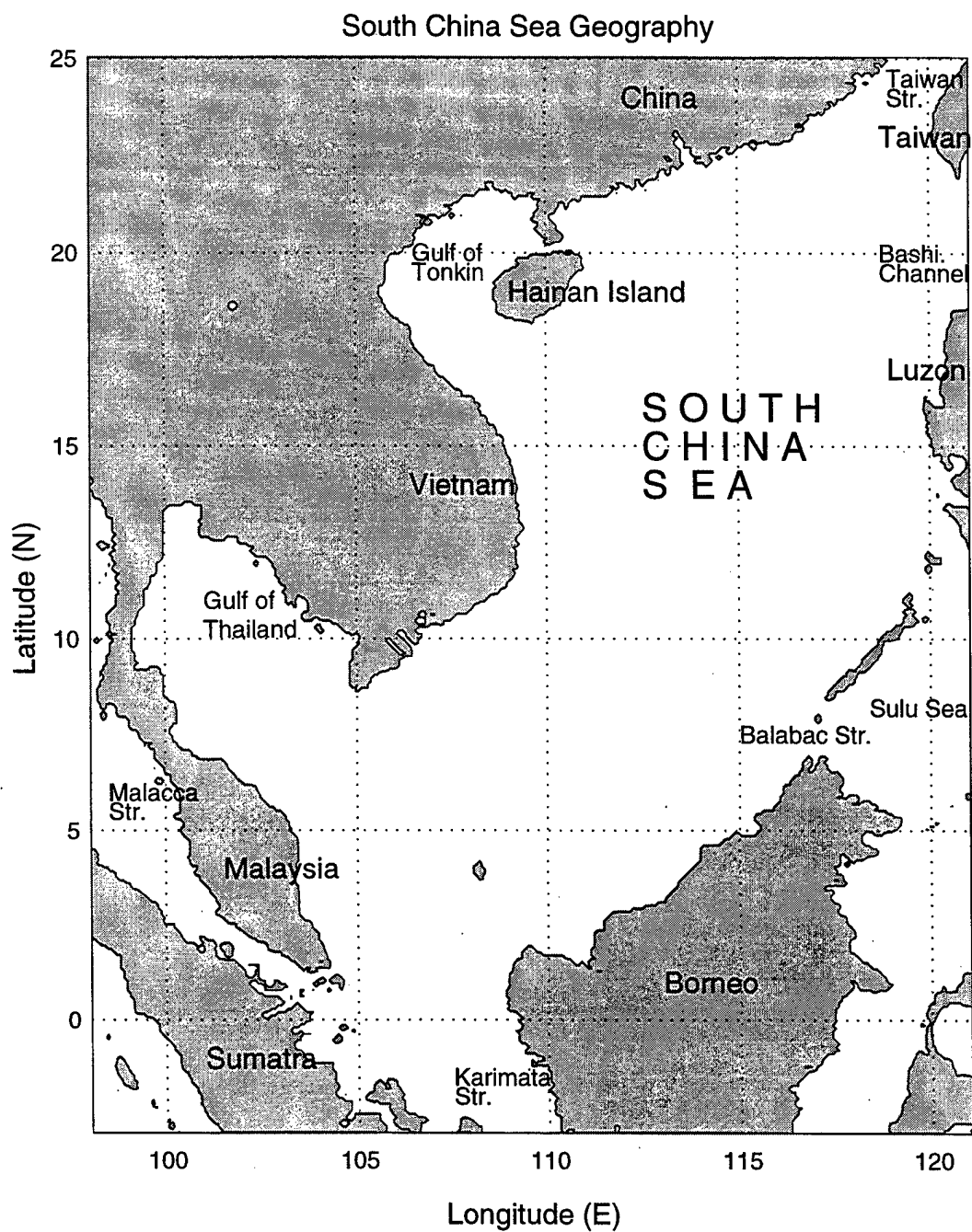


Figure 2.1. Geography of the South China Sea Basin.

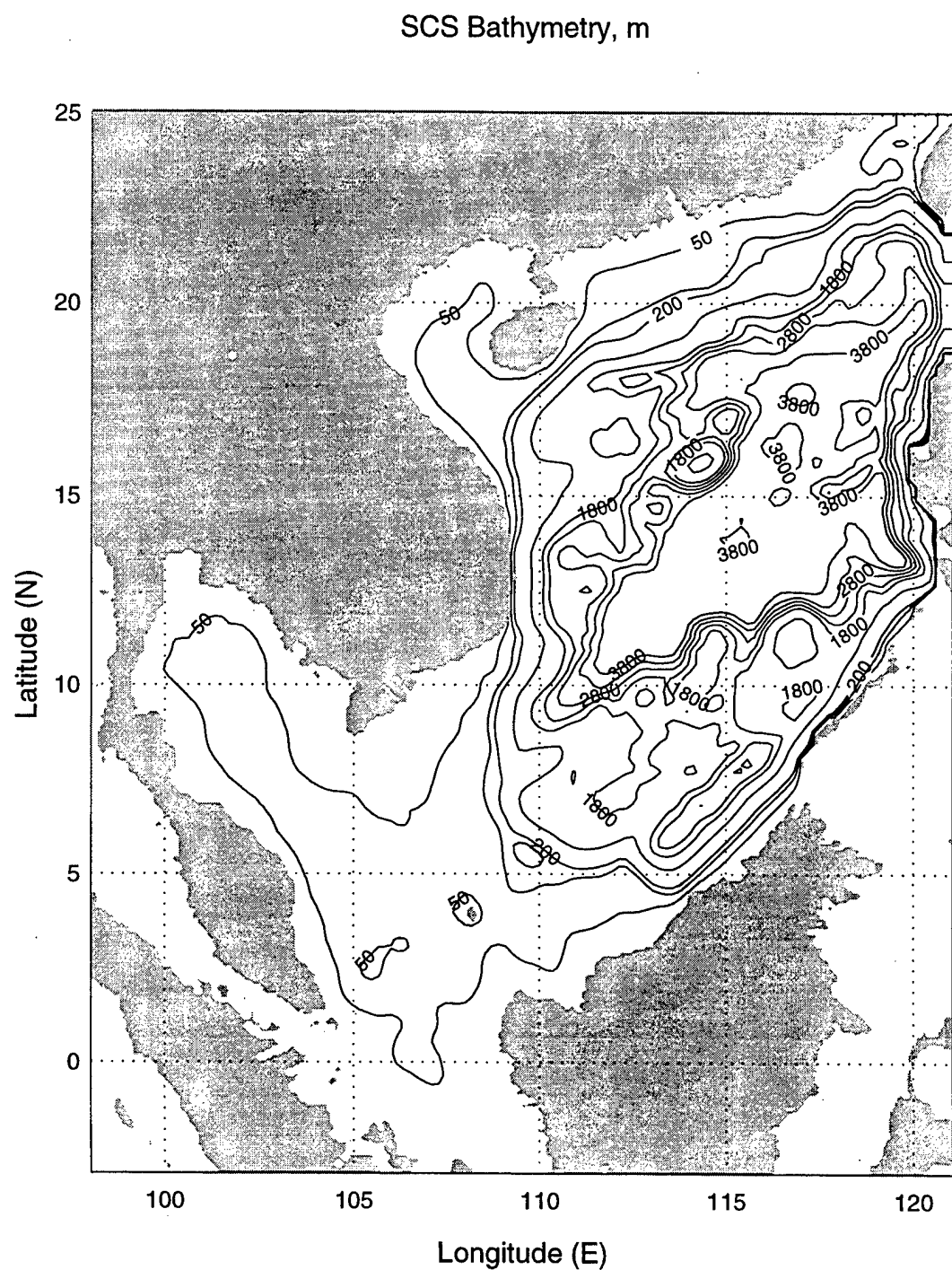


Figure 2.2. Bathymetry of the South China Sea basin. Contours in meters.

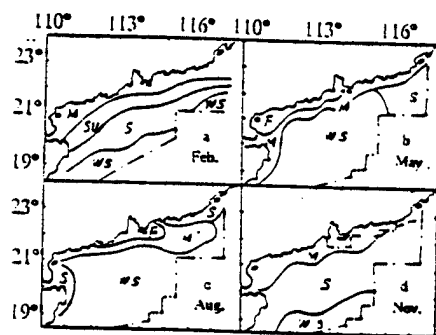


Figure 2.3. Water masses of the South China Sea. (From Su and Weng, 1994).

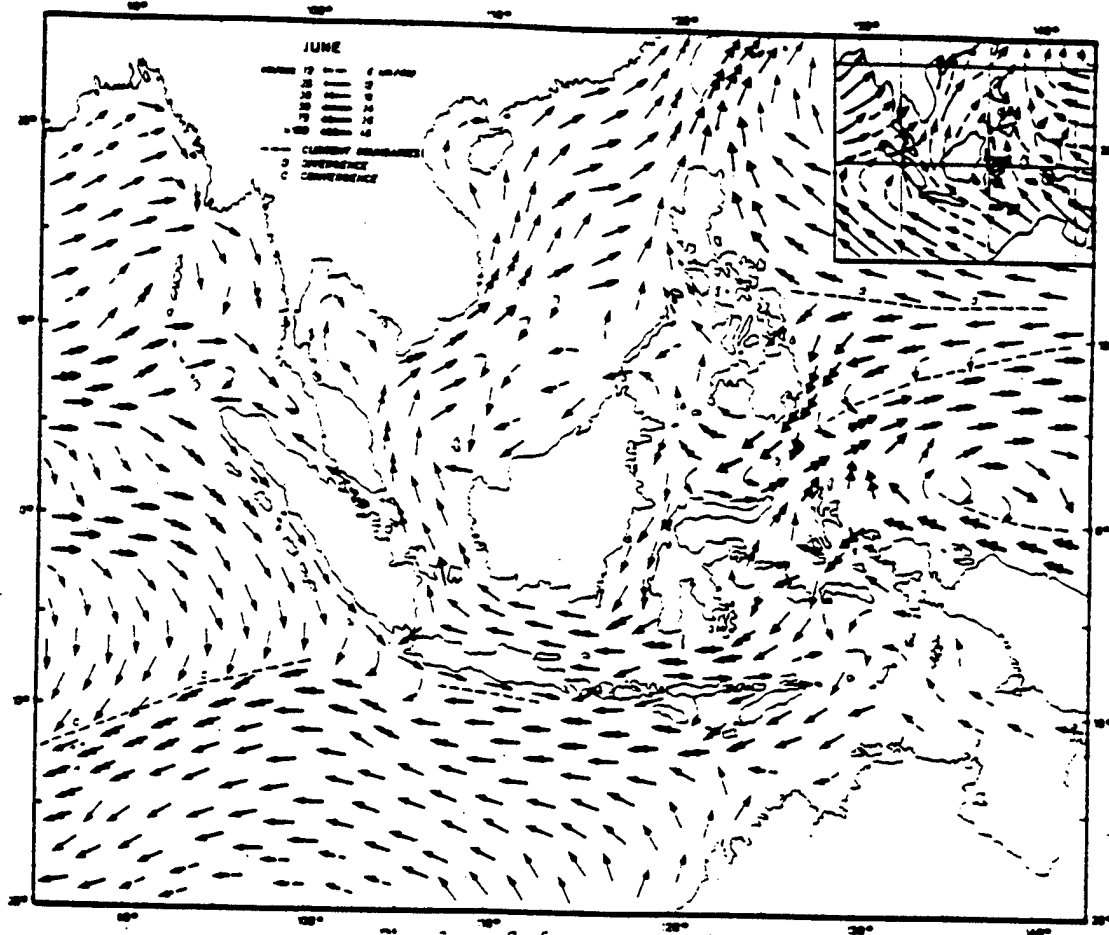


Figure 2.4. Summer surface current circulation pattern (From Wyrtki, 1961).

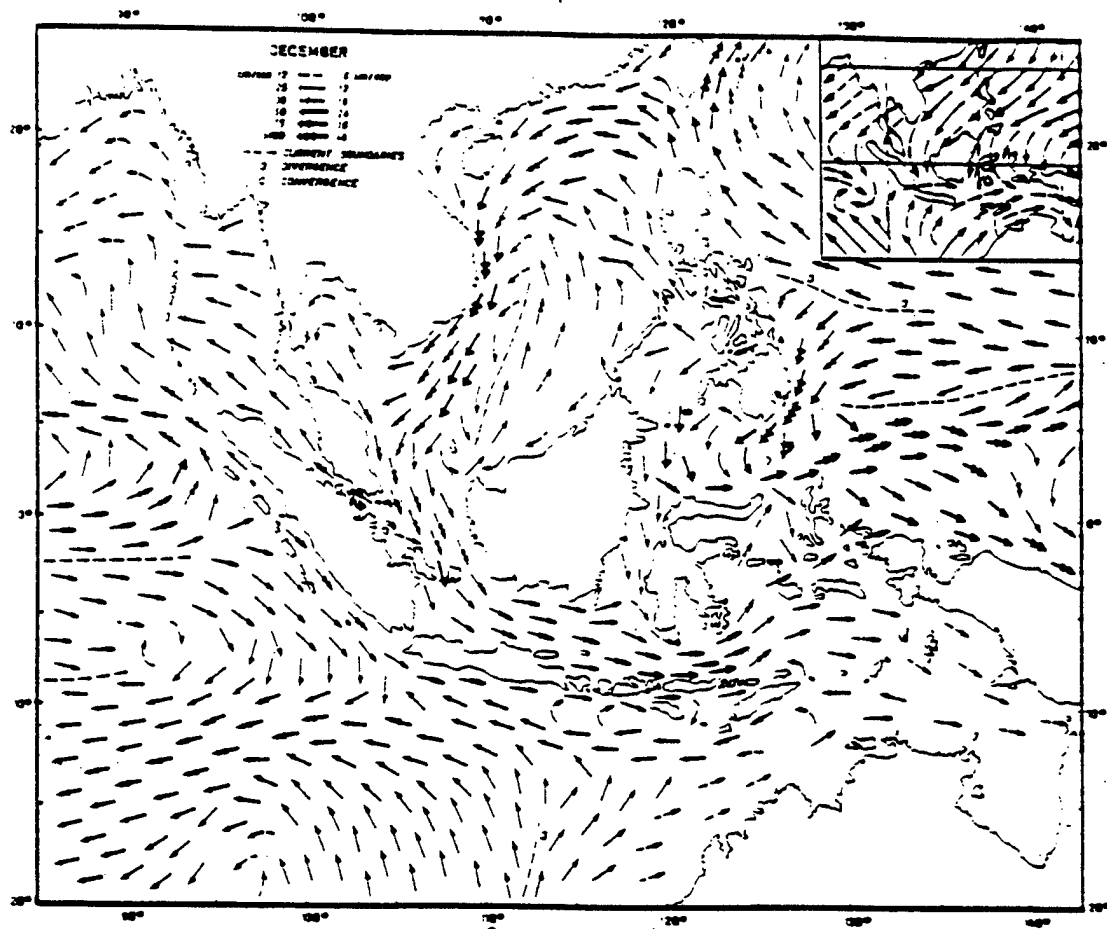


Figure 2.5. Winter surface current circulation pattern (From Wyrtki, 1961).

III. CLIMATOLOGY

Because of its geographic location between the Asian continent to the north, the oceanic regions to the south and its proximity to the equator, the SCS experiences a distinct seasonality in its climate. During the winter season winds are predominately out of the northeast and moderately strong, while during the summer season the winds completely reverse, becoming southerly and weak. A climate that experiences a directional shift of at least 120° between January and July and whose resultant wind speed exceeds 3 m/s during one of these months is known as a monsoon (Ramage, 1971). The monsoon climate of the SCS plays a vital role in the formation and movement of tropical cyclones in the region.

A. MONSOONAL WIND FLOW OVER THE SCS

The seasonal movement of the equatorial pressure trough, also known as the intertropical convergence zone (ITCZ), over the region produces this monsoonal wind flow over the SCS. Annual seasonal changes in synoptic conditions over the Asian continent control the movement of the ITCZ.

1. Southwest Monsoon

In July and August temperatures over the Asian continent, to the north of the SCS,

reach their annual maxima, producing lower pressure over the continental region. Cooler air over the SCS and oceanic regions to the south produce higher pressures over these regions. Between these regions lies the equatorial trough. The trough lies over the central Philippines and extends northwestward toward low pressure over the Tibetan Plateau. This pressure gradient between the warm continental regions to the north and cooler oceanic regions to the south causes air to flow southeasterly south of the equator. The air flow then turns southwesterly as it crosses the equator and flows over the SCS, producing the southwest monsoon (Ramage, 1971) (Figure 3.1a).

This pressure gradient is weak however. Cooler air brought south by the low pressure systems traveling over the continent and horizontal air mass mixing by tropical cyclones prevents a strong heat low from forming over the east Asian continent. The weak pressure gradient produces the light, averaging about 3 m/s, southwest monsoon winds over the SCS (Ramage, 1971).

2. Northeast Monsoon

The southwest monsoon pattern begins to retreat in September as the Asian continent begins to cool and high pressure starts to build over the region. Air temperatures over the oceanic regions remain warm and the pressure gradient begins to reverse. The first northeast winds are felt over the northern SCS, while over the rest of the region the southwest monsoon flow weakens slightly. In October the equatorial trough begins to move rapidly to the south. By the middle of the month the trough lies

along a line from the center of the Bay of Bengal to the north coast of New Guinea.

North of the trough northerly winds prevail as high pressure centered over central Asia continues to build, while south of the trough the southeast monsoon still dominates (Ramage, 1971).

The northeast monsoon begins to set up in November when the equatorial trough moves south of the equator. The northeast monsoon intensifies over the SCS and monthly mean wind speeds increase to 7 m/s. By December the equatorial trough lies near 5° S, just north of Australia. High pressure firmly established over the Asian continent intensifies the pressure gradient between the continent and the oceanic region. The northeast monsoon flow reaches its strongest force over the SCS at this time, averaging 8 to 10 m/s. The flow over the SCS north of the equator is predominately northerly to northeasterly. South of the equator, however, the reversal in the sign of the Coriolis force causes the flow to turn to the east and becomes northwesterly to westerly (Ramage, 1971) (Figure 3.1b).

The northeast monsoonal continues over the region until April when temperatures over the Asian continent start to increase and the equatorial trough begins to move to the north. Winds in the northern SCS remain northeasterly, but weaken. In May the northeast monsoon completely collapses, as the Asian continent continues to warm and the pressure gradient between the continental and oceanic regions reverses. The southeast monsoon begins to establish itself over the SCS. By June the southeast monsoon is fully established over the region (Ramage, 1971).

B. MONSOONAL INFLUENCE ON SCS TROPICAL CYCLONES

1. Tropical Cyclone Formation

More tropical cyclones form over the Western North Pacific and SCS regions than in any other ocean basin, with an average of 26 per year (McBride, 1995) (Table 3.1).

Season		North Atlantic	Eastern N Pacific	Western N Pacific	North Indian	Southwest Indian <100°E	Australia/ SE Indian 100-142°E	Australia/ SW Pacific >142°E	Totals
Y. Num	S. Num								
1968	1968-69	8(5)	18(6)	27(20)	7(4)*	8(6)*	4(0)*	7(3)*	79(42)
1969	1969-70	18(12)	10(4)	19(13)	6(2)*	13(8)*	4(2)*	7(3)*	77(44)
1970	1970-71	10(5)	19(4)	26(12)	7(4)*	15(10)*	7(6)*	7(3)*	89(44)
1971	1971-72	13(6)	18(12)	35(26)	7(6)*	8(5)*	6(3)*	16(11)*	103(65)
1972	1972-73	7(3)	14(9)	30(22)	7(6)*	13(8)*	8(6)*	10(2)*	89(56)
1973	1973-74	8(4)	12(7)	21(12)	6(1)*	8(1)*	9(6)*	13(3)*	77(34)
1974	1974-75	11(4)	18(11)	32(15)	7(2)*	10(3)*	9(5)*	5(3)*	92(43)
1975	1975-76	9(6)	17(9)	20(14)	7(3)*	8(3)*	8(3)*	11(5)*	80(43)
1976	1976-77	10(6)	15(9)	25(16)	10(4)*	9(5)*	6(5)*	13(3)*	88(46)
1977	1977-78	6(5)	8(4)	19(11)	6(5)*	14(2)*	6(3)*	10(4)*	69(36)
1978	1978-79	12(5)	19(14)	28(15)	6(3)*	9(4)*	7(3)*	8(3)*	89(47)
1979	1979-80	9(5)	10(6)	23(16)	5(3)*	12(5)*	9(7)*	9(4)*	77(44)
1980	1980-81	11(9)	14(7)	24(15)	3(0)*	12(2)*	10(6)*	10(4)*	86(43)
1981	1981-82	12(7)	15(8)	28(16)	6(3)*	11(4)*	11(4)*	2(2)*	85(44)
1982	1982-83	6(2)	23(12)	26(19)	5(4)*	6(0)*	4(1)*	12(10)*	82(48)
1983	1983-84	4(3)	21(12)	23(12)	3(1)*	11(4)*	7(4)*	7(3)*	76(39)
1984	1984-85	13(5)	21(13)	27(16)	3(2)*	8(1)*	10(2)*	8(6)*	90(45)
1985	1985-86	11(7)	23(13)	26(17)	7(0)*	12(5)*	8(2)*	8(5)*	95(49)
1986	1986-87	6(4)	17(9)	27(19)	1(0)*	7(3)	6(3)*	12(6)	75(43)
1987	1987-88	7(3)	20(10)	24(18)	5(1)*	14(7)	1(0)*	7(3)	79(43)
1988	1988-89	12(5)	15(7)	26(14)	3(1)*	12(9)	5(3)*	11(5)	85(45)
1989	1989-90	11(7)	17(9)	31(21)	3(2)*	8(5)*	7(1)*	6(3)*	80(47)
22-year totals		214(118)	364(195)	565(353)	120(55)	228(98)	152(75)	199(94)	1842(988)
Average		9.7(5.4)	16.5(8.9)	25.7(16.0)	5.4(2.5)	10.4(4.4)	6.9(3.4)	9.0(4.3)	83.7(44.9)
Stnd deviation		3.1(2.2)	4.1(3.0)	4.1(3.6)	2.1(1.7)	2.6(2.6)	2.4(2.1)	3.1(2.3)	7.8(6.4)
Global Total		11.6(12.0)	19.8(19.7)	30.7(35.7)	6.5(5.6)	12.4(9.9)	8.2(7.6)	10.8(9.5)	100.0%

Table 3.1. Annual tropical cyclone frequency during 1968 through 1989-90 season in seven basins, where left (right) entry is the number with maximum sustained surface wind exceeding 17 m/s (32 m/s) (From Neumann, 1993).

Although highly seasonal, this is the only region in the world where tropical cyclones have occurred in all months of the year. The primary reason for this high incidence of occurrence is the persistently warm sea surface temperature and the location of the ITCZ. When the ITCZ occurs as a convergence zone in the westerly monsoon flow, it is known as the monsoon trough (Gray, 1968). The trough is the shearline separating the monsoonal westerlies from the trade easterlies and is a preferred region for tropical cyclone development. Reviews of annual tropical cyclone reports produced by the United States Navy Joint Typhoon Warning Center (JTWC) at Guam show those initial disturbances that subsequently develop into tropical cyclones most frequently (80%) develop in the monsoon trough (McBride, 1995).

When monsoon westerlies are present, the upper-level subtropical high pressure ridge overlies the low-level monsoon shearline, in the mean seasonal pattern. This pattern (Figure 3.2) of trade easterlies overlain with westerlies and monsoon westerlies overlain with easterlies results in a seasonal-mean vertical wind shear close to zero. Westerly shear is on the poleward side and easterly shear on the equatorward side of the monsoon trough (McBride, 1995).

Not only does this situation produce low level cyclonic wind shear, but low values of vertical wind shear allows a disturbance on the trough to develop into a tropical cyclone, through the formation of a warm core. Cyclonic wind shear causes wind to flow inward toward the center of the disturbance. The underlying warm ocean will heat the inflowing air, causing it to rise. As the air parcels rise, they cool and convection takes

place, releasing latent heat and making the moist warm air unstable. These parcels subsequently expand, cool and sink. As the air parcels sink, they are warmed due to compression. Those parcels that sink in the center of the circulation begin to form an upper level warm core of air. This heating will then lower the air pressure, which will in turn induce more air flow into the circulation and produce further vertical lifting due to mass convergence. The generated positive feedback loop enables the formation of a tropical cyclone.

This environmental factor however is only one of six factors necessary for the formation of a tropical cyclone. The other five factors are (1) strong low-level cyclonic vorticity, (2) a location a few degrees poleward of the equator, (3) sea surface temperatures exceeding 26° C, (4) conditional instability through a deep atmospheric layer and (5) large values of relative humidity in the lower and mid troposphere (Gray, 1968, 1975, 1979).

The majority of these factors are routinely present in the Western Pacific and the SCS. Therefore, tropical cyclones may form and influence the Western Pacific and the SCS region throughout the year, as shown in historical data from 1945 to 1988 for the region (Figure 3.3). Examination of this data reveals that the region does however experience a peak frequency of occurrence from May through December, with a maximum in August. An examination of the SCS data separately reveals a slight double peak in storm frequency, with the first peak around May and the second peak around October. The location of the monsoon trough over the region during these periods causes

this distribution (U.S. Naval Pacific Meteorology and Oceanography Center/Joint Typhoon Warning Center Guam, 1991).

2. Tropical Cyclone Movement

Tropical cyclones that form in the SCS are not the only ones that affect the basin however. Those that form in the Western Pacific may also move into the SCS if the proper environmental steering flow exists (Figure 3.4).

Many factors affect the motion of tropical cyclones. To a first order, however, the largest influence on the storm's motion is the mean air flow that surrounds it (Elsberry, 1995). The changing synoptic pattern of the overall region continuously alters the motion of the cyclone. The tropical cyclone initially forms in the tropics, where the mean flow is easterly, causing the cyclone to move to the west. The cyclone may also gain latitude as it moves westward due to its motion over the rotating earth. On a rotating, spherical earth any cyclonic vortex will generate an additional advective flow. This flow is westward and poleward, because of the requirement to conserve absolute vorticity (Carr, 1989). The cyclone will therefore have a general tendency to move to the northwest. With no other influences the cyclone will usually continue to move northwesterly until it encounters the mid-latitude westerlies and its track recurses to the northeast.

The presence of a strong high pressure ridge to the north, over the southern Asian continent, prevents tropical cyclones that affect the SCS from moving northward

however. This strong pressure ridge not only prevents the storm from moving northward, away from the SCS region, but also provides the necessary easterly steering flow. The presence of this ridge allows tropical cyclones to remain near the equator and move to west over the SCS. This high pressure ridge is present during the winter months, when the Tibetan High ridges eastward and merges with the Western Pacific subequatorial ridge. The ridge, along with the orientation of the monsoon trough over the SCS, contributes to high occurrences of tropical cyclones over the region (Elsberry, 1995).

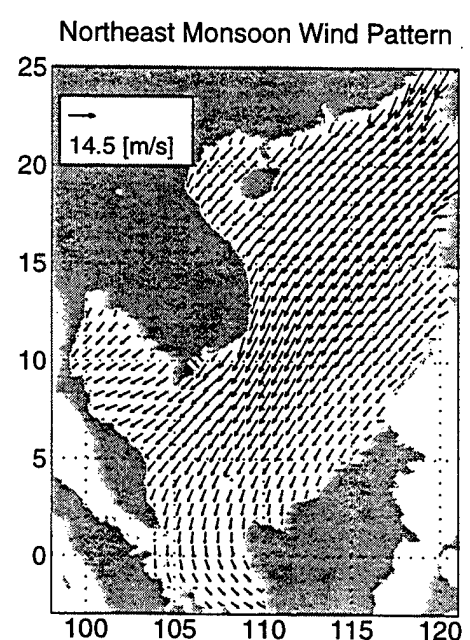
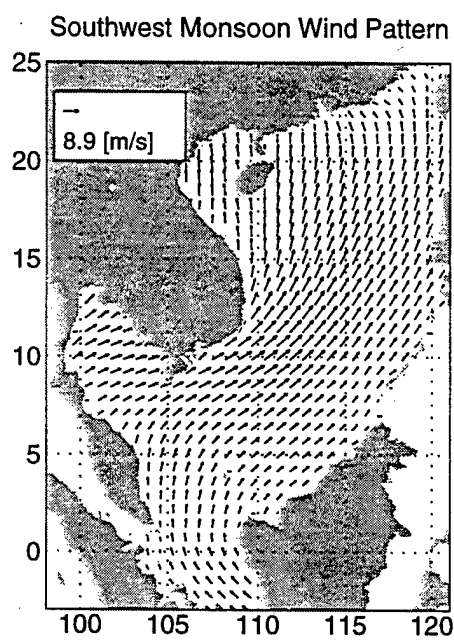


Figure 3.1. (a) Southwest monsoon wind pattern. (b) Northeast monsoon wind pattern (From Hellerman and Rosenstein, 1983).

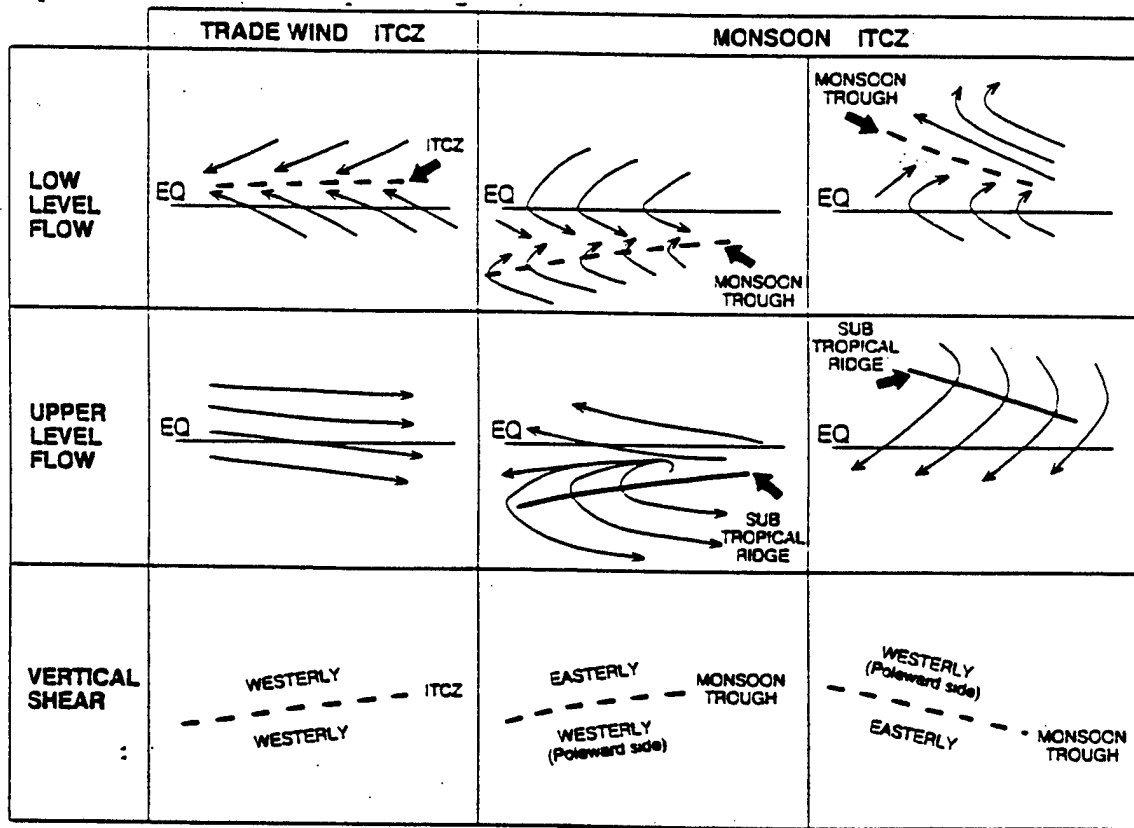


Figure 3.2. Schematics of tradewind (left) and monsoon type (right) ITCZ flow regimes typical of the western North Pacific basin during August. Vertical shear between the low-level and upper-level flow is indicated in the lower panels (From McBride, 1995).

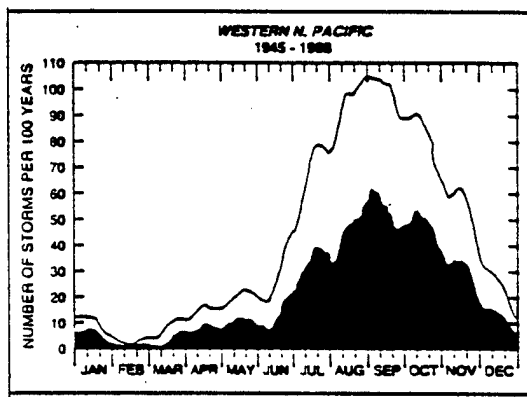


Figure 3.3. Seasonal tropical cyclone frequency for the Western North Pacific. Upper and lower bounds refer to maximum winds of at least 17 m/s and 33 m/s, respectfully. Data has been smoothed over a 15 day period (From Neumann, 1993).

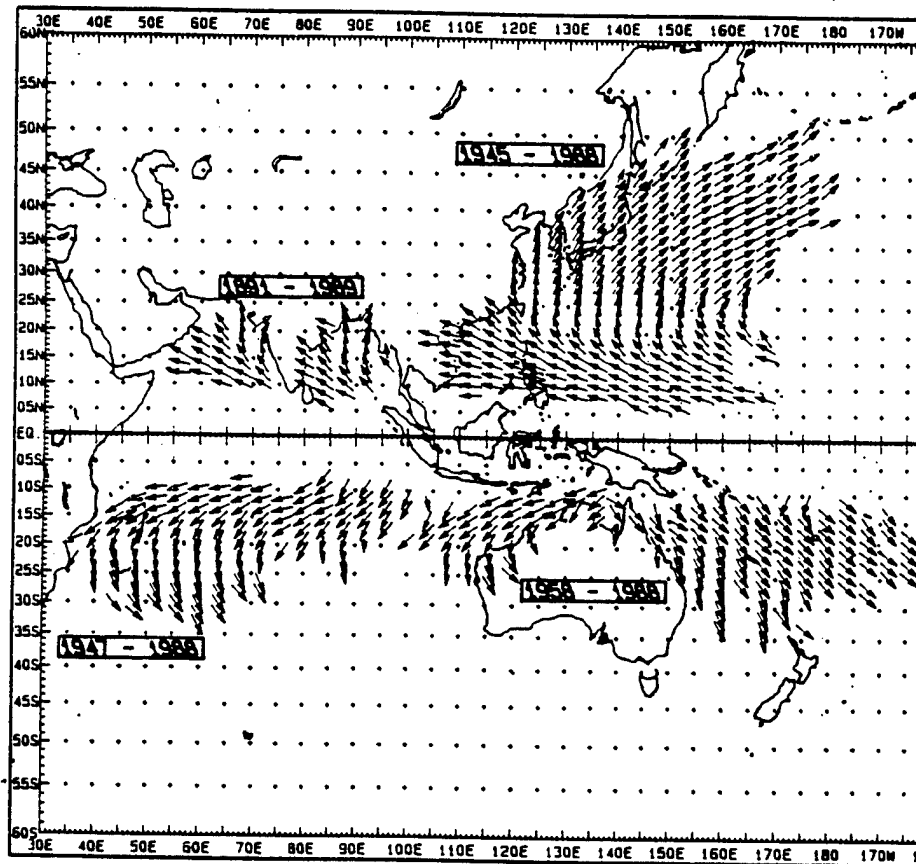


Figure 3.4. Annual average of tropical cyclone motion (vector heading) during the indicated periods for various regions. Only storms that reached 17 m/s are included (From Neumann, 1993).

IV. SCS WIND FIELD MODEL

A key aspect of this study was the selection of a tropical cyclone and the development of an atmospheric wind model of that storm. The tropical cyclone chosen was Tropical Storm Ernie, which affected the SCS during November 1996 (Figure 4.1).

A. TROPICAL STORM ERNIE (1996)

Tropical Storm Ernie initially formed about 1300 km to the east of the Philippine island of Mindanao on November 4, 1996. After formation, Ernie slowly intensified as it tracked westward through the Philippine Sea toward the central Philippine Islands. On November 6 Ernie made landfall over Mindanao and intensified to tropical storm strength, 18 m/s. Ernie continued moving westerly through the Philippine Islands, intensifying at a slow rate because of frictional interaction with the land. The storm entered the SCS on November 8 and reached an intensity of 25 m/s. Ernie began moving northerly toward a break in the mid-latitude ridge and Tropical Depression 39W (TD 39W), which had formed during the previous day over Luzon, to the northeast of Ernie. The storm merged with TD 39W and became quasi-stationary on November 11, as the mid-latitude ridge strengthened.

Late on November 11 Ernie commenced a slow southerly drift toward Luzon, approximately 270 km to the southeast. On November 12 Ernie was over Luzon and

mid-level easterly steering flow intensified, causing the system to begin moving to the west-southwest back into the SCS. Ernie continued moving to the west-southwest over the next four days, passing over the southern tip of Vietnam, and slowly weakening to 15 m/s. Ernie tracked into the Gulf of Thailand and then finally into the eastern Bay of Bengal where it dissipated over water on November 18.

B. SCS TROPICAL CYCLONE WIND FIELD DECOMPOSITION

The wind field, \bar{V} , of a moving tropical cyclone has three main components (Figure 4.2),

$$\bar{V} = \bar{V}_c + \bar{V}_t + \bar{V}_{bg}, \quad (4.1)$$

where \bar{V}_c is the wind vector produced by the tropical cyclone, \bar{V}_t is the tropical cyclone translational vector and \bar{V}_{bg} is the wind vector of the background wind surrounding the storm.

The best track storm course and speed, from post-storm analysis by the United States Navy Joint Typhoon Warning Center at Guam (JTWC) (Appendix), is used to determine the components of \bar{V}_t . This component of the storm wind produces the distinct asymmetrical wind structure of a moving tropical cyclone. The translational vector components cause enhanced wind flow on the right side of the moving storm and diminished wind flow on the left side. This asymmetrical forcing contributes

significantly to the production of the unique oceanic thermal and current patterns generated by the storm.

The background wind, \bar{V}_{bg} , used with this model was the November wind field of the Hellerman and Rosenstein (1983) global monthly wind model. During the model run a cubic spline interpolation scheme adjusts the November wind field at each time step of the run.

Components of \bar{V}_c , the tropical cyclone wind vector, are either a storm-centered tangential component, v_c , and radially directed inward component, u_c , or the usual earth centered north-south, v_y , and east-west, u_x , components. Carr and Elsberry (1997) developed the basic tropical cyclone wind profile model used to produce this tropical cyclone wind field. This model is a physically-meaningful storm-centered model of the tropical cyclone tangential wind field based on the approximate conservation of absolute angular momentum.

1. Carr and Elsberry Tropical Cyclone Wind Profile Model

In polar coordinate form equation (4.2) gives the absolute angular momentum, M_a , of a parcel, in a uniformly circular storm,

$$M_a(r,t) = rv + \frac{1}{2}f_o r^2 , \quad (4.2)$$

where r is the storm radius, v is the tangential wind speed and f_o is the Coriolis parameter

at the tropical cyclone's central latitude. The terms on the right side are the angular momentum contributions due to the storm's tangential velocity in an earth-relative polar coordinate system and the rotation of the earth coordinate system, respectively.

M_a has a pressure level dependence since the storm's tangential wind speed decreases with decreasing height due to a reduction in frictional effects. However, for the purposes of this study only the surface wind speed will be considered. Therefore, the wind profile equations do not denote a pressure level dependence.

In an asymmetrical vortex, such as a moving tropical storm, frictional torque reduces M_a of a parcel,

$$\frac{dM_a}{dt} = rF_\theta, \quad (4.3)$$

where F_θ is the frictional effect in the tangential direction. The frictional torque in the low-level inflow region of a tropical cyclone decreases the parcel's angular momentum as it spirals inward toward the center of the cyclone. Using the assumption that the tropical cyclone circulation does not change rapidly with time, M_a may be approximated as a steady function of only radii in a cyclone following coordinate system. Equation (4.1) may then be rewritten as,

$$v(r) = \frac{M_a(r)}{r} - \frac{1}{2}f_o r, \quad (4.4)$$

This equation provides a radius-dependent expression for the tropical cyclone tangential

wind field, which includes the frictional effect.

Frank (1984) showed that M_a decreases rapidly with a decreasing radius in the lower troposphere near the tropical cyclone center. The inward decrease of M_a , however, is slower at the outward radii where the wind speeds and frictional effects are less. Equation (4.5) may then approximate the lower tropospheric M_a in equation (4.3),

$$M_a(r) = Mr^{(1-X)} , \quad (4.5)$$

where X is a positive constant less than 1.0. Substituting equation (4.4) into equation (4.3) yields the following equation,

$$v(r) = \frac{M}{r^X} - \frac{1}{2}f_o r . \quad (4.6)$$

With suitable values of M and X specified, equation (4.6) models the tropical cyclone tangential wind field outside the radius of maximum winds.

M may be determined by making the assumption that there is a radius, R_o , at which the tropical cyclone winds reduce to zero,

$$v(R_o) = 0 . \quad (4.7)$$

After using equation (4.7) with equation (4.3), and equation (4.4) to relate $M_a(r)$ to M the following relationship is formed,

$$M = \frac{1}{2}f_o(R_o)^{(1+X)} . \quad (4.8)$$

Equation (4.8) determines the angular momentum of the tropical cyclone, given its central latitude and size. This equation, along with equation (4.5), may be used to calculate the tropical cyclone's tangential wind profile, given appropriate values of R_o and X .

The inward component of the tropical cyclone wind, $u(r)$, is computed from the tangential wind using the following relationship,

$$u(r) = \tan(\gamma)v(r) , \quad (4.9)$$

where γ is the inflow angle of the wind as it spirals into the center of the cyclone. The inflow angle profile used for this model study uses the form of the composite model hurricane compiled by NOAA/NWS (1979) for use in design studies. NOAA/NWS studies determined that they could form a relationship to relate the wind inflow angle, γ , to the ratio of the storm radius and the radius of maximum winds of the storm, R_m (Figure 4.3).

The derived tropical cyclone wind profile has an exponential form, where the profile wind speed approaches infinity at the storm center. However, a physical tropical cyclone's wind speed reduces to near zero at its center. As suggested by Carr and Elsberry (1997), multiplying the right side of equation (4.5) by equation (4.10) makes the tropical cyclone wind profile continuous at the storm center.

$$\varepsilon_1(i,j) = \frac{a^4}{1+a^4}, \quad (4.10)$$

where $a = \frac{r(i,j)}{0.75 * R_m}$. At large values of r , ε_1 is nearly 1; however as r approaches 0, ε_1 also approaches 0 (Figure 4.4a). This results in a smooth and continuous tangential tropical cyclone wind profile (Figure 4.5).

2. SCS Tropical Cyclone Wind Field Model

The SCS POM requires an earth centered coordinate system wind field. To provide this forcing the tropical cyclone centered tangential wind profile was converted to an earth centered longitude and latitude wind field using the following transformations,

$$u_x(i,j) = -|\bar{V}_c(r)| * \cos(\alpha(i,j)), \quad (4.11)$$

$$v_y(i,j) = |\bar{V}_c(r)| * \sin(\alpha(i,j)), \quad (4.12)$$

where $u_x(i,j)$ and $v_y(i,j)$ are the components of the tropical cyclone wind in the earth coordinate system at each model grid point. $|\bar{V}_c(r)|$ is the magnitude of the total tropical cyclone wind speed, computed using equations (4.6) and (4.9). α is the angle relating the tangential and radial storm wind components to these longitude and latitude wind components. Equation (4.11) determines α ,

$$\alpha(i,j) = \frac{\pi}{2} - (\theta(i,j) + \gamma(i,j)). \quad (4.13)$$

The final step in generating the SCS model wind field is to add the three main

components of the wind field together vectorially, equation (4.1). This equation calculates the components of $\bar{V}(i,j)$, the total model wind vector at each grid point.

To prevent a large discontinuity at the periphery of the storm however, the background wind field is blended into the tropical storm wind field. Adjustments made to the storm's translational speed, \bar{V}_t , and the background wind field, $\bar{V}_{bg}(i,j)$, near the storm's periphery smooth the transition between the background and storm wind fields. Multiplying the translational speed and the climatological wind components by the equations (4.14) and (4.15), respectfully, performs these adjustments.

$$\varepsilon_2(i,j) = \frac{b^4}{(1+b^4)} \quad (4.14)$$

$$\varepsilon_3(i,j) = \frac{c^4}{(1+c^4)} , \quad (4.15)$$

where $b = \frac{|\bar{V}_c|}{0.75 * |\bar{V}_t|}$ and $c = \frac{r}{0.9 * R_0}$ (Figures 4.4b and 4.4c). The effects of these adjustments are to increase the weighting on the storm translational speed gradually and decrease the weighting on the background winds as the radial distance to the storm center decreases. Both effects provide for a smoother transition between the storm wind field and the background wind field.

Finally, the surface wind stress components, τ_x and τ_y , which provided the forcing

to the SCS POM, are calculated at each model grid point (i, j) from the model wind field components using the standard bulk transfer formulas,

$$\tau_x(i,j) = \frac{\rho_a C_d \mu_x(i,j) |\bar{V}(i,j)|}{\rho_o} , \quad (4.16)$$

$$\tau_y(i,j) = \frac{\rho_a C_d \mu_y(i,j) |\bar{V}(i,j)|}{\rho_o} , \quad (4.17)$$

where ρ_a is the air density, which was set to 1.2 kg/m^3 , ρ_o is the sea water density, which was set to 1024 kg/m^3 and $|\bar{V}(i,j)|$ is the model wind speed at the surface. The drag coefficient, C_d , used with this study was the Large and Pond (1981) neutral form,

$$C_d = 1.14 \times 10^{-3} \text{ if } V_{tot} < 10 \text{ m/s} \quad (4.18)$$

or

$$C_d = (0.49 + 0.065 V_{tot}) \times 10^{-3} \text{ if } V_{tot} \geq 10 \text{ m/s} \quad (4.19)$$

This C_d is very similar to that inferred from hurricane wind observations using the geostrophic methods by Miller (1964).

3. Tropical Cyclone Parameters Determination

Calculations of the surface values of τ_x and τ_y during the model simulation require the determination of appropriate values of R_o , R_m , and X , the tropical cyclone

parameters, along with the radial distance from each model grid point to the storm center.

To determine the appropriate tropical cyclone parameters at each six hour storm analysis time X was set to a constant value and $|\bar{V}(r)|$ calculated using equations (4.6) and (4.9). $|\bar{V}(r)|$ was iteratively calculated, adjusting R_o at each iteration to minimize the RMS error between the model and analyzed profiles. R_m was then determined from the calculated wind profile. The minimum value of R_m was set to 20 km to enable the wind field to be adequately resolved on the SCS POM grid. A time series of the storm parameters (X, R_o, R_m), in addition to the storm's central latitude and longitude, and translational course and speed, was then produced for later input into the tropical cyclone wind field model (Appendix). During the model run linear interpolation of the storm parameters was done between each six-hour storm data set at every 900 second ocean model time step.

The result was a smooth, temporally varying wind field representing the undisturbed wind flow outside the tropical cyclone's influence and the variable intensity asymmetrical vortex of the tropical cyclone (Figures 4.6 and 4.7).

C. SCS WIND MODEL VERIFICATION

Comparing the model wind fields with the JTWC analyzed wind profiles and archived NASA Scatterometer (NSCAT) winds validated the SCS Wind Field Model of Ernie.

1. NSCAT and SCS Wind Model Comparisons

Varying X , the tropical cyclone wind profile coefficient, alters both the size of the storm and the shape of the wind profile. To determine what value of X was most appropriate to use to model Ernie the tropical cyclone wind model was run with four different values of X , 0.15, 0.26, 0.35 and 0.45. These wind fields were then compared with the analyzed profiles from JTWC and the retrieved NSCAT wind fields.

A verification of the SCS Tropical Cyclone Wind Model's ability to simulate wind profiles that were consistent with the JTWC analyzed wind profiles was done. This was accomplished by calculating the RMS error between the model and JTWC wind profiles at the 18 m/s wind radius. The 18 m/s radius was used as JTWC analyzes and reports this radius. Although JTWC reports the storm's maximum wind speed, the radius at which that wind speed occurs is not. This wind comparison was done for the 26 six-hour periods during which Ernie had wind speeds greater than or equal to 18 m/s. Table 4.1 lists the relevant statistical information from this analysis.

Storm coef. X :	0.15	0.26	0.35	0.45
Avg RMS error, m/s	1.05	1.54	1.96	2.47
Max RMS error, m/s	2.04	4.03	5.00	5.78
RMS std dev., m/s	0.57	0.75	1.05	1.37

Table 4.1. Tropical cyclone wind distribution model profile errors, compared with JTWC analyzed storm wind profile.

Although the average RMS errors are low for these four model runs, increasing

from 1.05 m/s for $X = 0.15$ to 2.47 m/s for $X = 0.45$, the 135% increase in these errors is high. The maximum error difference during the period is even larger, increasing 183% from 2.04 m/s to 5.78 m/s. These large error increases are a direct result of the structure of the storm profile, which X determines. The tropical cyclone wind profile has an exponential profile that is flatter for lower values of X than for larger values. The storm size, R_o , is larger for lower values of X . Figure 4.5 is a plot of the tropical cyclone wind profile for November 13 at 1200Z. Depicted are the four model profile plots produced by each tested value of X .

This analysis suggests that when lower values of X are used the wind profiles produced by the SCS Tropical Cyclone Wind Field Model are more consistent with the analyzed storm profiles. Few actual observations of the storm's wind field were available however. Therefore, the wind profile was primarily derived utilizing subjective satellite cloud signature analysis techniques. Errors in these reported wind profiles are therefore very difficult to quantify.

A verification of the wind model with retrieved NSCAT winds was also done. While wind profile comparisons were performed for the entire history of Tropical Storm Ernie, model wind field comparisons with NSCAT winds (Figures 4.8 and 4.9) were only conducted for the SCS POM domain, 98° W to 121° W and -3° S to 25° N.

Comparisons were made once per day from November 4 to 18. Both u and v wind components were examined, since the wind stress curl and divergence fields are major factors in how the ocean responds to tropical cyclone forcing. A time series of the

RMS errors for all four wind model runs indicates that both **u** and **v** model wind components agreed very well with the NSCAT data. RMS errors were all less than 6 m/s for the entire period (Figure 4.10). The largest errors were noted during the November 11 to 13 period. During this period the storm was moving over Luzon and significant modifications to the wind field was occurring. The wind model used in this study does not account for land interaction however, and this aspect of the model appears to be causing these large errors. This error is also apparent in the scaled RMS errors, the RMS error divided by the standard deviation of the NSCAT observation. For the majority of the run the scaled error was less than 1. However, scaled **u** and **v** errors did increase to 1.4 and 1.6, respectfully, on November 12 when Ernie was over Luzon. A strong decrease in the correlation coefficients for this period was also noted.

This error analysis of the wind field suggests that, with the exception of the period that Ernie was moving over Luzon, the wind model was successful in simulating the observed wind field. There is some uncertainty in this analysis as the NSCAT instrument cannot observe the entire SCS in one pass. Although, on average, the instrument observed 40% of the SCS each day, the only pass where the entire storm field was observed was on November 4, when the system was outside the SCS. Therefore, verifying the total model wind field is not possible.

A review of the combined wind profile and NSCAT error analysis indicates that a low value of X will best simulate the observed wind field. Although NSCAT error analysis shows that any values of X will produce a consistent wind field, lower values of

X produced a wind profile that was closer to the analyzed JTWC profile. A value of $X = 0.15$ was therefore used in the wind model for this study.

Tropical Storm Ernie (Nov 1996) Best Track

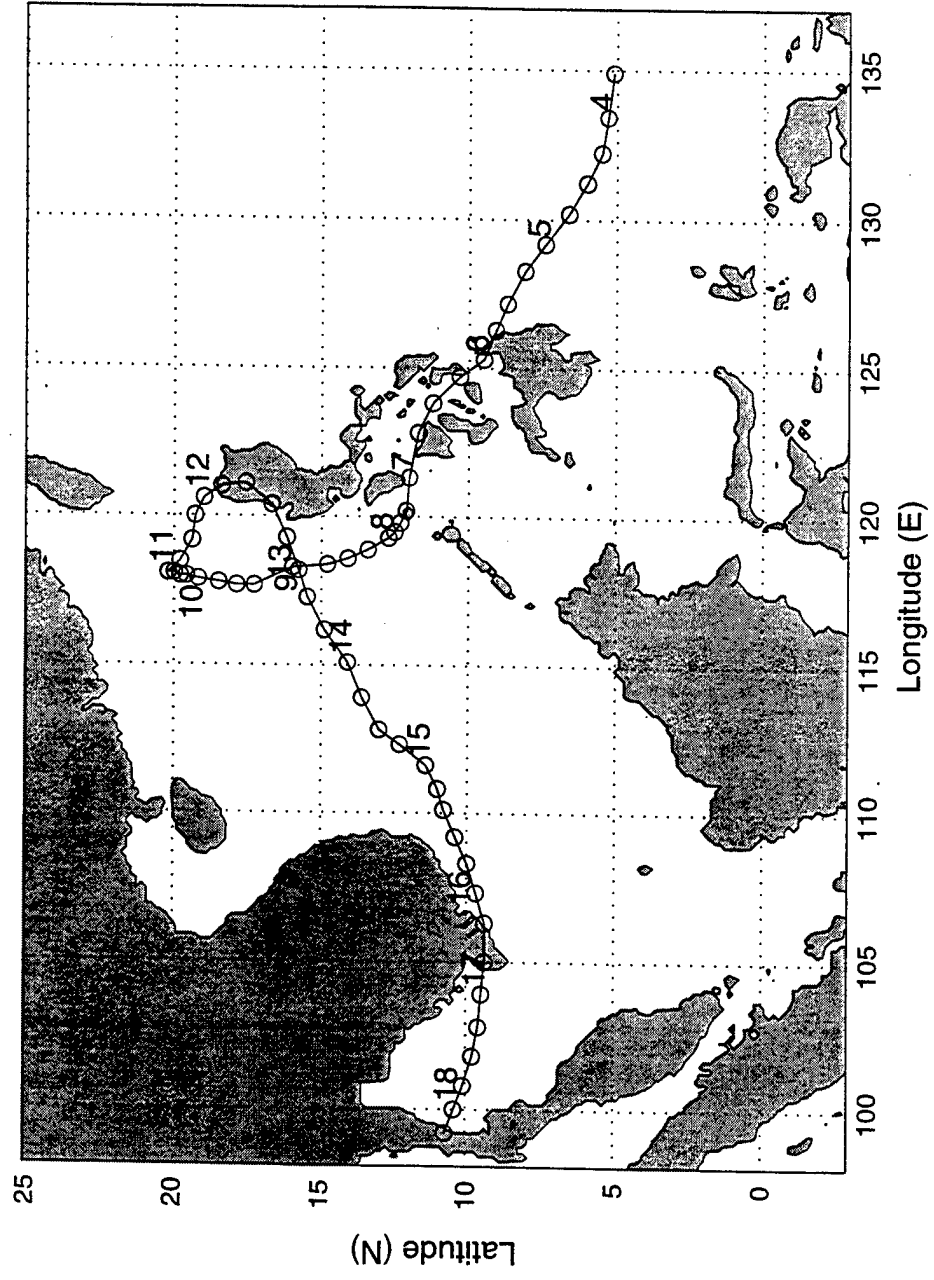


Figure 4.1. Tropical cyclone Ernie (1996) best track. Storm positions plotted at six hour intervals. Numbers next to storm position indicate day of November, 1996.

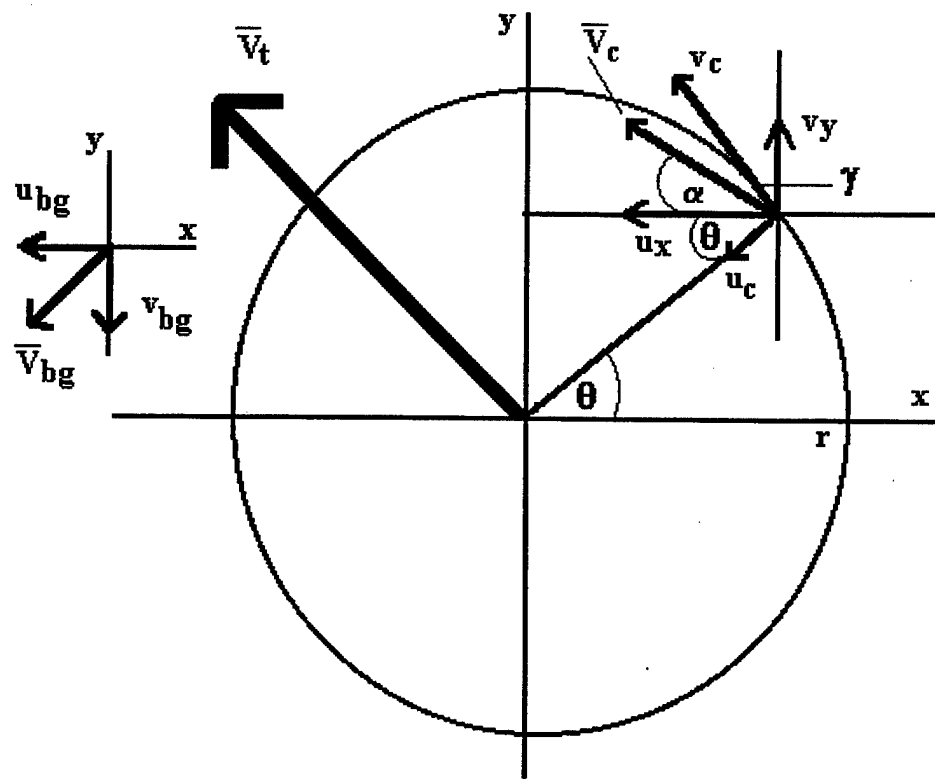


Figure 4.2. Tropical cyclone wind field decomposition. The angle θ is the usual directed angle in the storm center polar coordinate system and γ is the wind inflow angle, spiraling inward toward the storm's center.

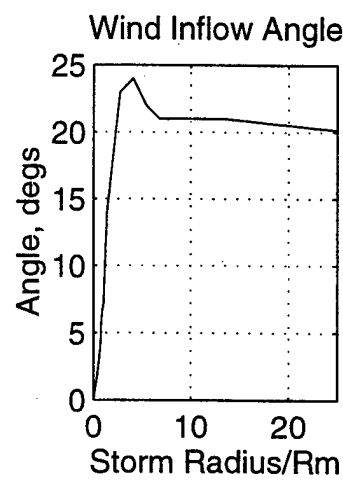


Figure 4.3. Tropical cyclone wind inflow angle. The horizontal axis is the ratio of r , the radial distance from the center of the storm., to R_m , the radius of maximum winds. The wind inflow angle is in degrees (From NOAA/NWS, 1979).

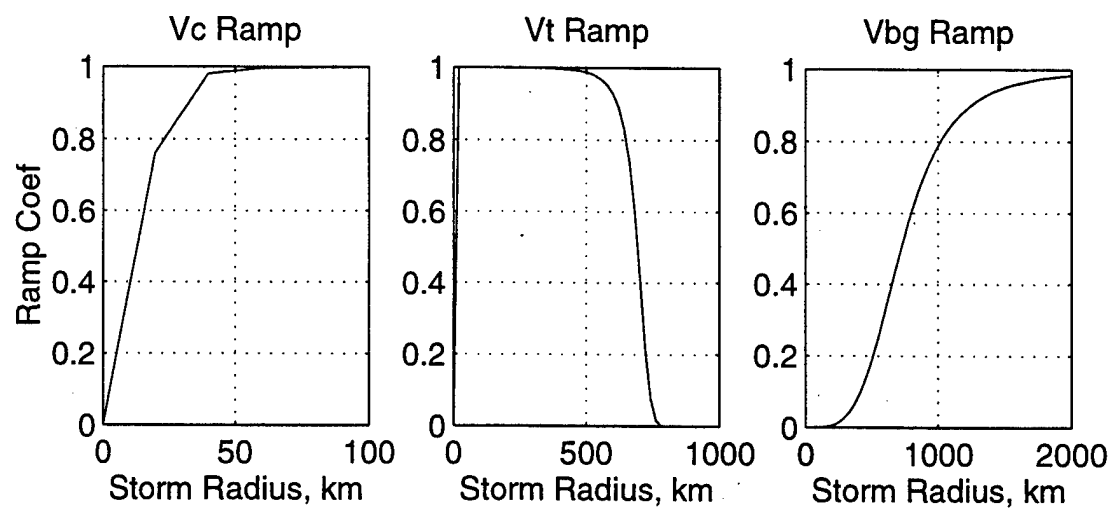


Figure 4.4. (a) Tropical cyclone wind profile adjustment equation, $\varepsilon 1$. (b) V_t adjustment, $\varepsilon 2$. (c) V_{bg} adjustment, $\varepsilon 3$.

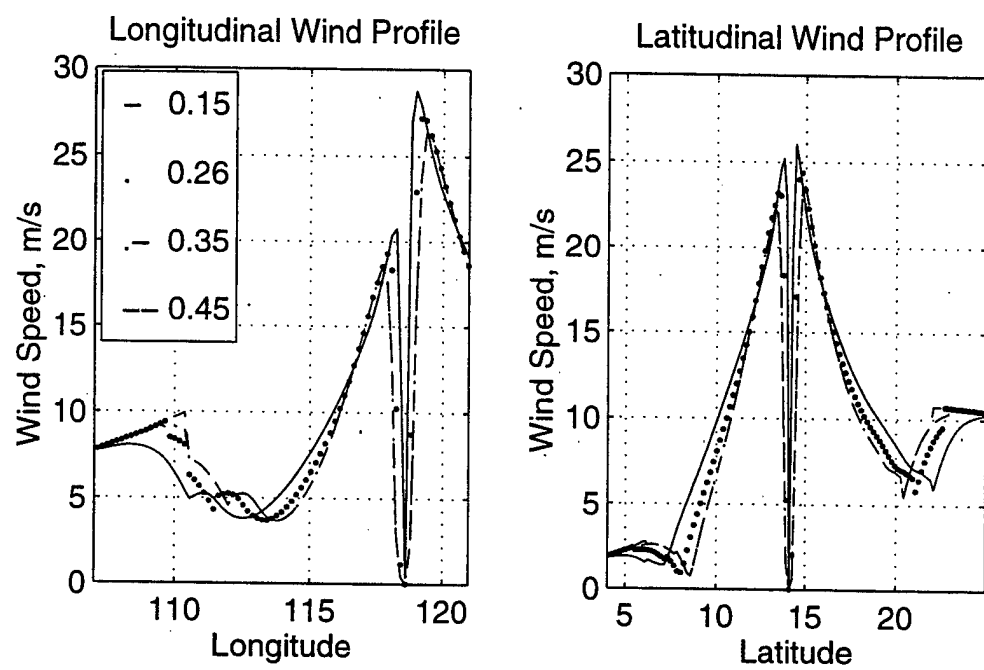


Figure 4.5. (a) Longitudinal radial tropical cyclone wind profile. (b) Latitudinal tropical cyclone wind profile.

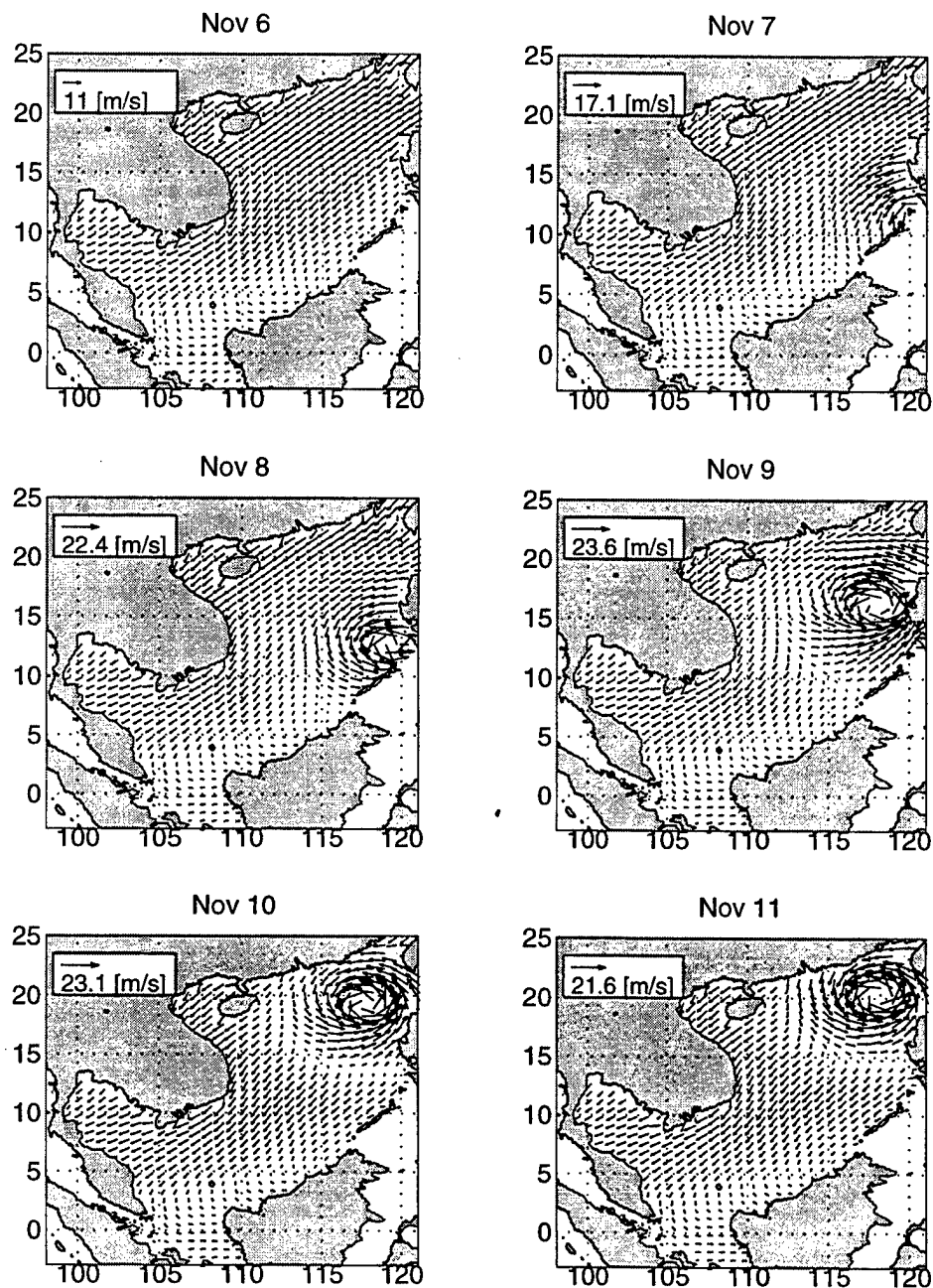


Figure 4.6. SCS model wind field for November 6 to 11, 1996. Wind speed in m/s.

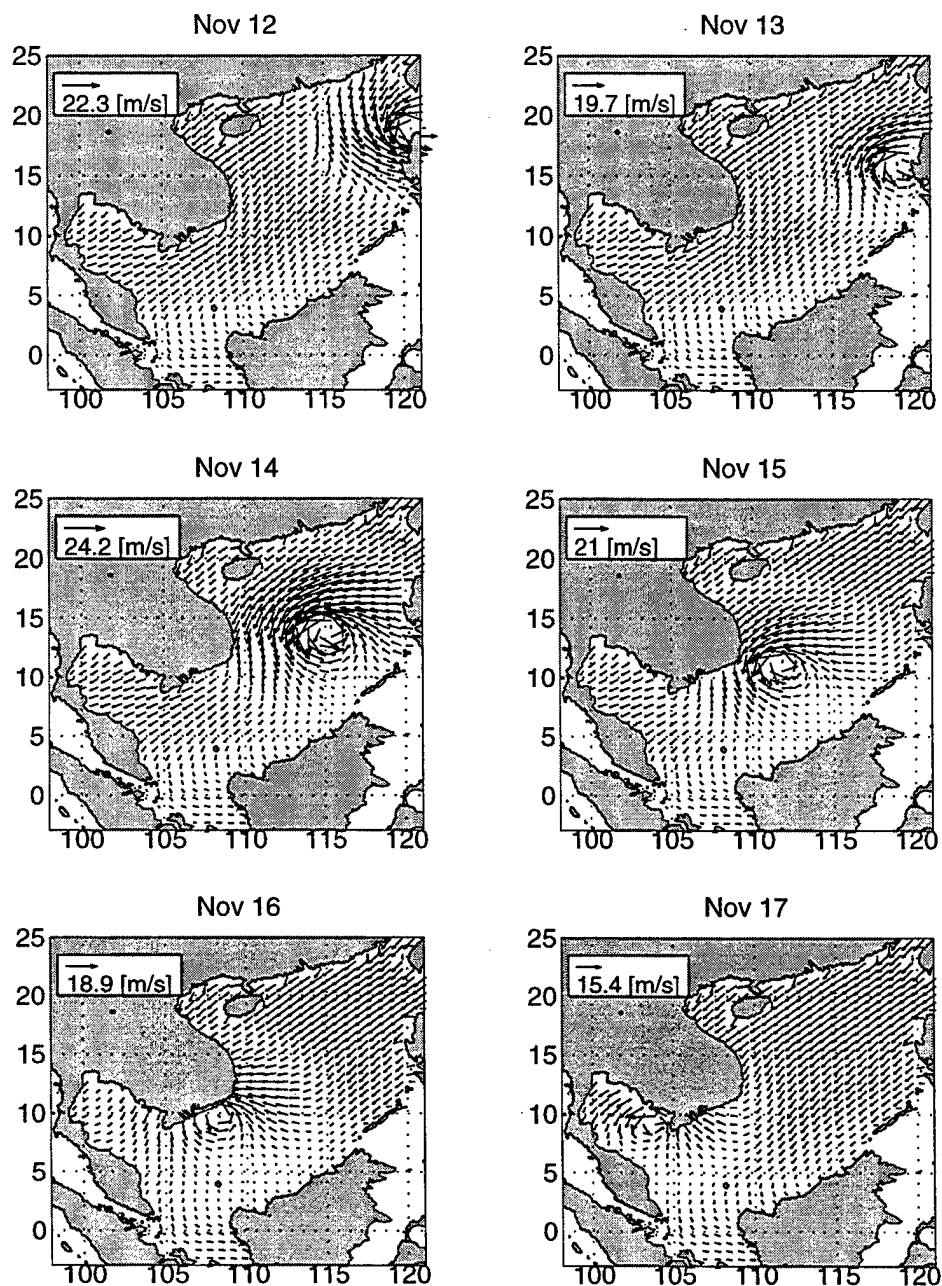


Figure 4.7. SCS model wind field for November 12 to 17, 1996. Wind speed in m/s.

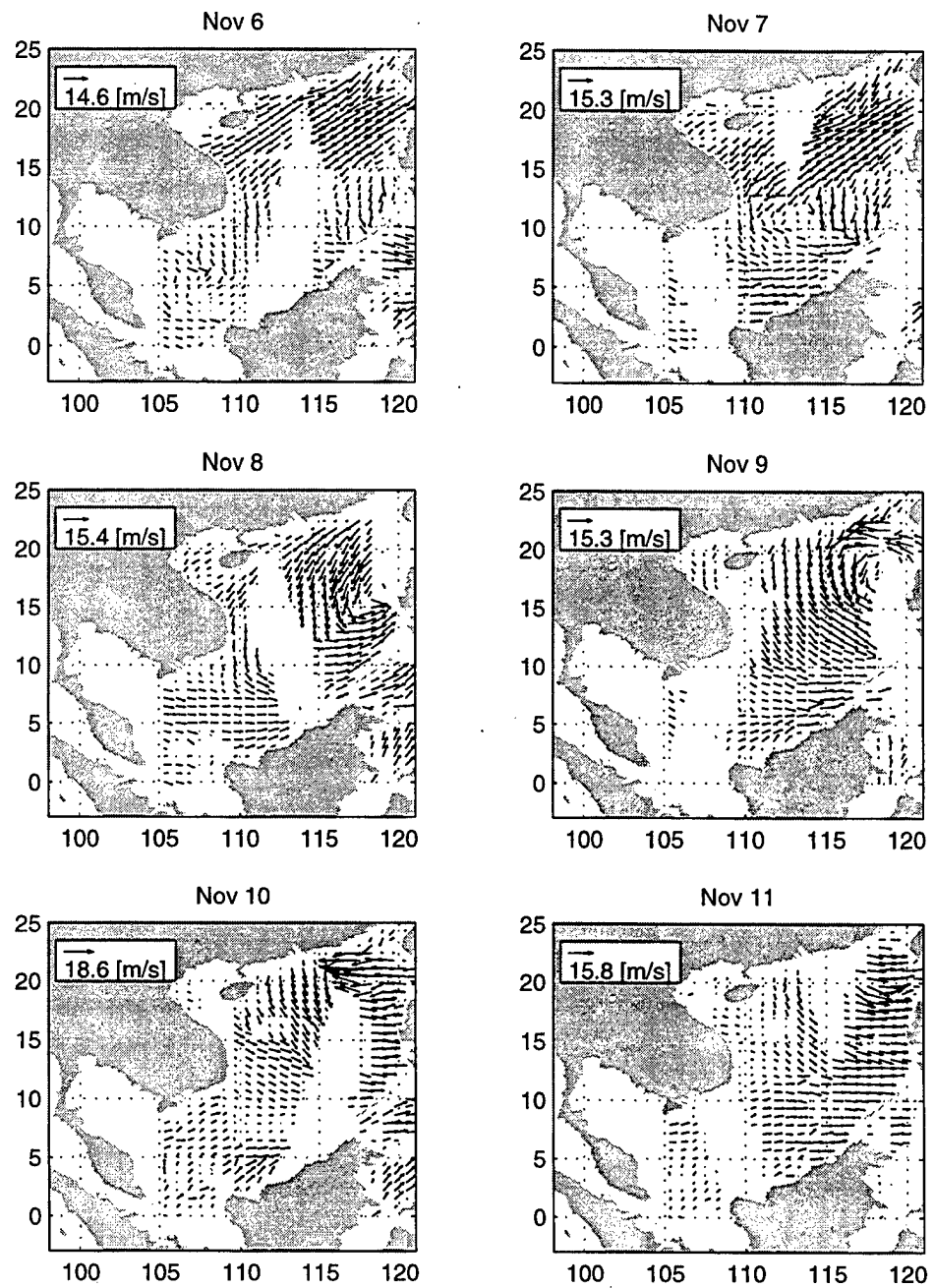


Figure 4.8. NSCAT wind field for November 6 to 11, 1996. Wind speed in m/s.

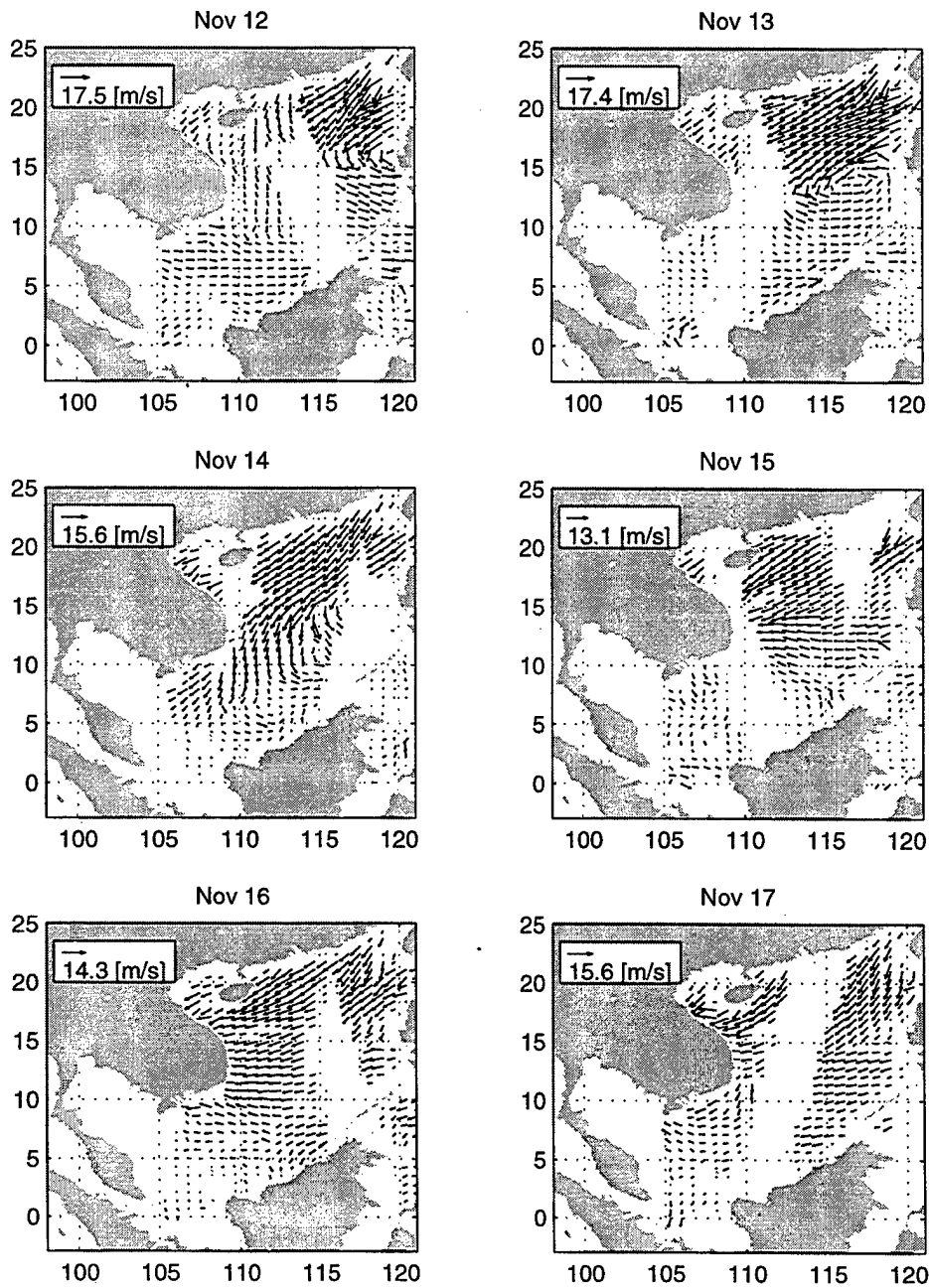


Figure 4.9. NSCAT wind field for November 12 to 17, 1996. Wind speed in m/s.

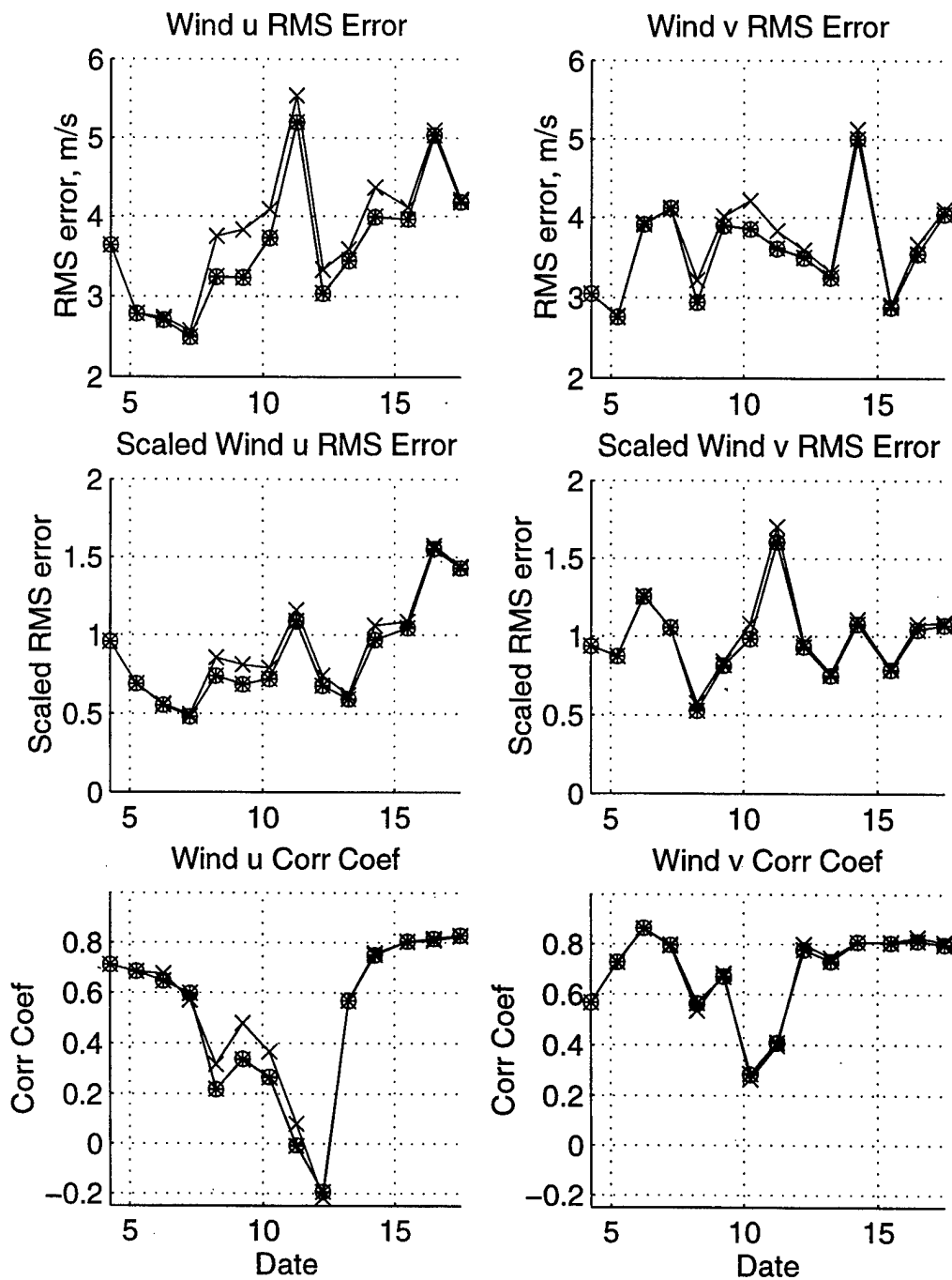


Figure 4.10. u and v wind component RMS errors, m/s, and correlation coefficients as compared to NSCAT data. Scaled RMS errors are RMS errors divided by NSCAT standard deviation.

V. PRINCETON OCEAN MODEL

A. MODEL FEATURES

Extreme high spatial and temporal variabilities that challenge prediction capabilities of numerical models mark ocean responses to tropical cyclone forcing. The ocean model used in this thesis to study these ocean responses is the Princeton Ocean Model (POM). The POM is a time dependent, primitive equation model in a three-dimensional grid that includes realistic topography and a free surface. Blumberg and Mellor (1987) developed this model at Princeton University. They specifically designed it to accommodate mesoscale phenomena, including nonlinear processes such as upwelling and eddy dynamics. These nonlinear processes are two of the most significant oceanic features produced by tropical cyclone forcing. Notable applications of the POM include simulation of circulation in the Gulf of Mexico (Blumberg and Mellor, 1985), the Gulf Stream (Mellor and Ezer, 1991 and Ezer and Mellor, 1992), the Kuroshio (Oey and Chen, 1991) and, most recently, a coupled atmospheric and oceanic model simulating oceanic sea surface temperature modifications caused by the passage of a tropical cyclone and the subsequent effect on the development of the storm (Ginis, 1997).

The SCS POM domain is from 3.06° S to 25.07° N and 98.84° E to 121.16° E, encompassing the SCS and the Gulf of Thailand. The SCS POM uses a rectilinear grid with horizontal spacing of 0.179° by 0.175° , resulting in a model resolution of

approximately 20 km. The 20 km grid resolution is of the same order of magnitude as the internal Rossby radius of deformation for the SCS, which is estimated to be 16-20 km. Therefore, the model adequately resolves most rotational effects. There are 23 sigma levels used in the vertical. Realistic bottom bathymetry from the Naval Oceanographic Office DBDB5 database, which has a resolution of 5 minutes by 5 minutes, is used.

The SCS Wind Model runs parallel to the POM and supplies the wind forcing, as described in Chapter IV of this thesis. Salinity and heat fluxes use the Haney-type restoring form (Haney, 1971). Seasonal variations in these quantities are used since precipitation and evaporation processes were not observed during Tropical Storm Ernie's passage through the region. Tidal forcing and river outflows are also not considered in this model. The model was sampled on a six-hour interval for the fourteen days that Ernie moved through the SCS region. This sampling rate should be high enough to capture most of the short term high frequency features produced by the tropical storm.

1. Sigma Coordinate System

Large bathymetric gradients create problems when incorporated in the standard, three dimensional orthogonal coordinate system. Model results near these large gradients tend to have many singularities that unrealistically affect adjacent grid values. To compensate for these problems the POM uses a contour following coordinate system based on a scaling of water depth at each horizontal grid location. The resulting sigma levels range from $\sigma = 0$ at the surface, $z = \eta$, to $\sigma = -1$ at the bottom, $z = -H$. Levels are

chosen between the surface and the bottom so that the model remains stable and achieves a sufficient vertical resolution to capture strong ocean processes in deep water. In this application 23 sigma levels are used.

The conversion between σ and z is:

$$\sigma = \frac{(z - \eta)}{(H + \eta)}, \quad (5.1)$$

where H is the mean water depth and η is the time varying free surface elevation at the horizontal grid point. Use of the sigma levels as the vertical coordinate system is not a perfect solution to the singularity problem. It does, however, allow for improved resolution of boundary layers and is a necessary procedure when dealing with topography with steep gradients, such as is found in the South China Sea (Mellor, 1992).

The sigma levels chosen in this study enable the POM to provide a mean vertical resolution of approximately 10 to 25 m in the upper 50 m of the water column and 50 to 100 m from $z = 50$ m to the bottom (Table 5.1). While this resolution is sufficient for general mesoscale processes occurring over the shelf regions, it does not allow for investigation of fine scale variations in the oceanic mixed layer in deep water.

2. Finite Differencing

The governing equations are finite differenced in a leapfrog manner, centered in space and time, to produce the model output. Model output includes the three

components of velocity (u, v, w), temperature and salinity at each grid point and depth averaged velocity, sea surface height η and two quantities that characterize the

σ Level	$H = 500 \text{ m}$	$H = 1000 \text{ m}$	$H = 2000 \text{ m}$	$H = 3000 \text{ m}$	$H = 4000 \text{ m}$
0.0000	0	0	0	0	0
-0.0125	-6	-13	-25	-38	-50
-0.0250	-13	-25	-50	-75	-100
-0.0500	-25	-50	-100	-150	-200
-0.1000	-50	-100	-200	-300	-400
-0.1500	-75	-150	-300	-450	-600
-0.2000	-100	-200	-400	-600	-800
-0.2500	-125	-250	-500	-750	-1000
-0.3000	-150	-300	-600	-900	-1200
-0.3500	-175	-350	-700	-1050	-1400
-0.4000	-200	-400	-800	-1200	-1600
-0.4500	-225	-450	-900	-1350	-1800
-0.5000	-250	-500	-1000	-1500	-2000
-0.5500	-275	-550	-1100	-1650	-2200
-0.6000	-300	-600	-1200	-1800	-2400
-0.6500	-325	-650	-1300	-1950	-2600
-0.7000	-350	-700	-1400	-2100	-2800
-0.7500	-375	-750	-1500	-2250	-3000
-0.8000	-400	-800	-1600	-2400	-3200
-0.8500	-425	-850	-1700	-2550	-3400
-0.9000	-450	-900	-1800	-2700	-3600
-0.9500	-475	-950	-1900	-2850	-3800
-1.0000	-500	-1000	-2000	-3000	-4000

Table 5.1. SCS POM σ levels and corresponding z levels (m) for $H = 500 \text{ m}$, 1000 m , 2000 m , 3000 m and 4000 m .

turbulence. The horizontal finite differencing is explicit on an Arakawa C-grid and includes advection, horizontal diffusion, pressure gradient and Coriolis effect subroutines. Vertically, the finite differencing is implicit to eliminate time constraints that would be imposed by the sigma level vertical coordinates due to their dependence on the time

varying free surface (Blumberg and Mellor, 1985).

3. Mode Splitting

Computational limitations require that the external mode (the two dimensional, barotropic, vertically integrated equations) be separated from the internal mode (the three dimensional, baroclinic, vertical structure equations) by a technique known as mode splitting (Blumberg and Mellor, 1987). Integrating the internal mode primitive equations over depth obtains the external mode equations. The barotropic solutions are then obtained before calculation of the internal mode equations. Mode splitting is applied with a barotropic time step of 25 seconds, based on the Courant-Friederichs-Levey (CFL) computational stability condition and the gravest external wave speed. Separating the governing equations into internal and external mode algorithms permits calculation of the free surface elevation and velocity transport, with no sacrifice in computational time from the calculation of the internal mode equations. Mode splitting and the explicit/implicit numerical scheme are the two essential features that allow the model to predict the highly variable dynamics of coastal regions and semi-enclosed seas.

4. Level Two Turbulence Closure

Equations used by the model are based on the Reynolds momentum and flux equations, where Reynolds stresses and flux terms (turbulence) require parameterization. Use is made of the Mellor-Yamada turbulence closure submodel (Mellor and Yamada,

1982) to provide the vertical eddy diffusivities for momentum, heat and salt ($K_{H,M}$) necessary to parameterize vertical mixing. These coefficients are calculated as a function of the turbulent kinetic energy and the turbulence length scale, a characteristic length of turbulent motion at any point in time or space. This process links the diffusivity coefficients with estimates of turbulence. Use of these coefficients allows the model to simulate realistic Ekman surface layers and mixed layer dynamics, both of which are important factors in the study of tropical cyclone wind forcing of the ocean.

B. MODEL GOVERNING EQUATIONS

The POM uses nonlinear equations solved over a Beta-plane to determine circulation and thermal structure. Two key assumptions are used: the fluid is in hydrostatic balance, where the weight of the water exactly balances the pressure force, and the Boussinesq Approximation, where the model neglects differences in density, unless multiplied by gravity (to include buoyancy effects).

1. Continuity Equation

$$\left(\frac{\partial U}{\partial x}\right) + \left(\frac{\partial V}{\partial y}\right) + \left(\frac{\partial W}{\partial z}\right) = 0 \quad (5.2)$$

This is the conservation of mass equation with U , V and W the mean velocities in the x ,

y, and z directions, respectively.

2. Momentum Equations

$$\left(\frac{\partial U}{\partial t}\right) + \nabla \cdot U - fV = -\left(\frac{1}{\rho_0}\right)\left(\frac{\partial P}{\partial x}\right) + \left(\frac{\partial}{\partial z}\right)\left(K_M \frac{\partial U}{\partial z}\right) + F_x \quad (5.3)$$

$$\left(\frac{\partial V}{\partial t}\right) + \nabla \cdot V + fU = -\left(\frac{1}{\rho_0}\right)\left(\frac{\partial P}{\partial y}\right) + \left(\frac{\partial}{\partial z}\right)\left(K_M \frac{\partial V}{\partial z}\right) + F_y \quad (5.4)$$

$$\rho g = -\frac{\partial P}{\partial z} \quad (5.5)$$

Equations (5.3), (5.4) and (5.5) are the momentum equations in x, y and z respectfully, with ρ_0 the reference density, ρ the *in situ* density, g the gravitational accelerations, P the pressure, K_M the vertical eddy diffusivity of turbulent mixing of momentum, and f the Coriolis parameter. $F_{x,y}$ represents the sum of processes occurring below the resolution of the model grid size.

3. Temperature and Salinity Conservations Equations

$$\left(\frac{\partial \theta}{\partial t}\right) + V \cdot \nabla \theta = \frac{\partial}{\partial z}\left(K_H \frac{\partial \theta}{\partial z}\right) + F_\theta \quad (5.6)$$

$$\left(\frac{\partial S}{\partial t}\right) + V \cdot \nabla S = \frac{\partial}{\partial z}\left(K_H \frac{\partial S}{\partial z}\right) + F_s \quad (5.7)$$

where Θ is the potential temperature (or *in situ* temperature for shallow water conditions) and S is the salinity. K_H denotes the vertical eddy diffusivity for turbulent mixing of heat and salt, and $\mathbf{F}_{\theta,S}$ represents the sum of processes occurring below the resolution of the model grid size.

4. Subgrid Scale Horizontal Mixing Processes

The model parameterizes processes that occur below the resolution of the model grid size in terms of horizontal mixing processes:

$$F_x = \frac{\partial}{\partial x} \left(2A_M \frac{\partial U}{\partial x} + \frac{\partial}{\partial y} \left(A_M \left(\frac{\partial U}{\partial y} + \frac{\partial V}{\partial x} \right) \right) \right) \quad (5.8)$$

$$F_y = \frac{\partial}{\partial y} \left(2A_M \frac{\partial V}{\partial y} + \frac{\partial}{\partial x} \left(A_M \left(\frac{\partial U}{\partial y} + \frac{\partial V}{\partial x} \right) \right) \right) \quad (5.9)$$

$$F_{\theta,S} = \frac{\partial}{\partial x} \left(A_H \frac{\partial(\Theta, S)}{\partial x} \right) + \frac{\partial}{\partial y} \left(A_H \frac{\partial(\Theta, S)}{\partial y} \right) + R_{\theta,S} \quad (5.10)$$

where A_M and A_H are the horizontal diffusivities required to damp small scale computational noise. Horizontal diffusivities are taken from the Smagorinsky formula (Smagorinsky, 1963):

$$A_M = C \Delta x \Delta y \left(\frac{1}{2} \right) \left| \nabla V + (\nabla V)^T \right| \quad (5.11)$$

with C the horizontal constant, chosen to be 0.2 for this application, V the velocity vector

at grid location (x,y) and the superscript T denoting the transpose applied to the gradient of \mathbf{V} .

C. INITIAL CONDITIONS AND BOUNDARY CONDITIONS

1. Initial Conditions and Initialization

The model was integrated from an initial at rest state and temperature and salinity specified by interpolating the climatology data (Levitus, 1984) to each model grid point. The model year consists of 360 days (30 days per month), with day 361 corresponding to January 1. It was found that after 90 days the model reached a quasi-steady state under these initial conditions (Edmons, 1996). The model was integrated for 34 months and 3 days before the introduction of the tropical cyclone wind forcing, after which it was run for another fourteen days with this forcing.

2. Bottom Boundaries

The bottom boundary conditions are calculated by:

$$\rho_0 \mathbf{K}_M \left(\frac{\partial U}{\partial z}, \frac{\partial V}{\partial z} \right) = (\tau_{bx}, \tau_{by}), \quad (5.12)$$

where (τ_{bx}, τ_{by}) is the bottom frictional stress vector, determined by matching the velocity

at the nearest gird point with the logarithmic law of the wall:

$$\tau_b = \rho_0 C_D |V_b| V_b, \quad (5.13)$$

where V_b is the velocity vector at the boundary and the drag coefficient, C_D is specified as 0.0025 (Blumberg and Mellor, 1985).

3. Forcing

a. Atmospheric forcing

Atmospheric forcing for the SCS POM includes both mechanical and thermal forcing. The model determines mechanical forcing by equation:

$$\rho_0 K_M \left(\frac{\partial U}{\partial z}, \frac{\partial V}{\partial z} \right) = (\tau_x, \tau_y), \quad (5.14)$$

where (τ_x, τ_y) are the two components of the wind stress vectors. During the model initialization the components of the wind stress vectors were taken from the Hellerman and Rosenstein (1983) database. After initialization the SCS Tropical Cyclone Wind Model was utilized to calculate the model wind field, as described in Chapter IV of this thesis.

Surface thermal forcing is determined by the equations:

$$K_H \frac{\partial \theta}{\partial z} = \alpha_1 \left(\frac{Q_H}{\rho C_p} \right) + \alpha_2 C (\theta_{OBS} - \theta), \quad (5.15)$$

$$K_S \frac{\partial S}{\partial z} = \alpha_1 Q_S + \alpha_2 C (S_{OBS} - S), \quad (5.16)$$

where θ_{OBS} and S_{OBS} are the observed potential temperature and salinity, C_p is the specific heat, and Q_H and Q_S are the surface heat and salinity fluxes, respectively. The relaxation constant, C , is the reciprocal of the restoring period for a unit volume of water. α_1 and α_2 are switch type parameters that may be with 1 or 0. If $\alpha_1 = 0$, $\alpha_2 = 1$ then the model applies only flux forcing; if $\alpha_1 = 1$, $\alpha_2 = 0$ then only restoring type forcing is applied. Since no thermal or salinity flux data was available for the time Ernie affected the SCS restoring type forcing was used in this study. While this procedure will have some affect on the thermodynamics of the model and produce errors between the model thermal fields and the actual state of the basin, the errors are expected to be small near the vicinity of the storm. SST decreases due to heat fluxes to the atmosphere typically account for less than 20% of the total decrease (Price, 1981; Black, 1983; Greatbatch, 1985; Bender, 1993), therefore, this procedure will be sufficient for this study. Further, the net effect of using a restoring type forcing is that the SCS will act as a heat source during the model run, which is consistent with air-sea thermal interactions. A C of 0.7 m/d was used in this study, which is equivalent to a relaxation time of 43 days for an upper layer 30 m thick (Chu et al., 1996).

b. Lateral boundary forcing

Closed lateral boundaries, horizontal land-sea boundaries, were incorporated using a free slip condition for velocity and a zero gradient condition for temperature and salinity. No advective or diffusive fluxes occur through these boundaries.

Open lateral boundaries are problematic in any oceanic model. The study assumes that the volume transports through the open boundaries at the Balabac Channel, Mindoro Strait, and Strait of Malacca are zero; only the Luzon Strait, Taiwan Strait and Gasper/Karimatra Straits are assumed to be open. The hydrographic data from the Naga Report (Wyrtki, 1961) was used to specify monthly boundary transport values. Barotropic velocities (V_n) at the open boundaries are calculated by the equation:

$$V_n = \frac{\text{Transport}}{\int_t H dl}, \quad (5.17)$$

where the seasonal transport is given in Table 5.2. l is the boundary width, n is the normal direction to the boundary and H is the water depth. The model calculates baroclinic velocities at the boundaries by (Chu, et al. 1996)

$$V_{nBC} = V_n \frac{e^\sigma}{(1 - e^{-1})} \quad (5.18)$$

Month	Feb.	Apr.	Jun.	Aug.	Oct.	Dec.
Gasper & Karimata Straits	4.4	0.0	-4.0	-3.0	1.0	4.3
Luzon	-3.5	0.0	3.0	2.5	-0.6	-3.4
Taiwan	-0.9	0.0	1.0	0.5	-0.4	-0.9

Table 5.2. Bi-monthly variation of volume transport (Sv) at the open boundaries (From Wyrtki, 1961).

The model similarly prescribes temperature and salinity advection through the open boundaries when transport at the boundary is into the model domain. When transport is flowing out of the model domain, the advection gradient equation

$$\frac{\partial(\theta, S)}{\partial t} + U_n \frac{\partial(\theta, S)}{\partial n} = 0 \quad (5.19)$$

is solved for both barotropic and baroclinic modes, where the subscript is the coordinate normal to the boundary.

VI. OCEAN RESPONSE TO TROPICAL CYCLONE FORCING

A moving tropical cyclone is an intense source of surface wind stress and stress curl that produces many significant responses in the ocean environment. Three of the most distinctive are changes to the ocean thermal structure, upper ocean currents and sea surface elevation.

A. OBSERVATIONS OF OCEAN RESPONSES

1. Ocean Thermal Structure

a. *Sea Surface Temperature (SST) Cooling*

Tropical cyclone forced cooling of the sea surface is a unique phonomania that is very important to the interaction between tropical cyclones and the ocean (Emmanuel, 1988). This ocean response is one of the most extensively studied, since researchers may observe it remotely through satellites (Stramma et al., 1986) and aircraft infrared sensors.

Many observations of SST clearly show that SST usually decreases by several degrees Celsius due to the storm forcing. Fisher (1958) documented a 3° C cooling by analyzing ship reports after the passage of tropical cyclones Connie and Diana in 1955. In 1964 Jordan was the first to document that maximum SST decreases occur on the right side of the storm track. Hazelworth (1968) analyzed the ship and buoy

measurements of SST cooling that resulted from ten hurricanes. He concluded that the SST reached its minimum values to the right side of the storm track, about one day after storm passage.

Black conducted further extensive studies of SST cooling (1983) for the period 1971-1980. He analyzed airborne infrared radiation thermometer (AIRT) and aircraft-expendable bathythermograph (AXBT) data. His summary shows a crescent shaped pattern for the SST decreases (Figure 6.1). The largest decrease is found in the right rear quadrant between R_m and $2R_m$.

b. Subsurface Thermal Structure Modification

While remote sensors can observe SST cooling patterns, subsurface observations of thermal responses are much more difficult to obtain. The usual techniques of subsurface temperature sampling using XBT and Conductivity-Temperature-Depth (CTD) sensors only provides a limited look at the larger pattern. Researchers require many such samples to gain an insight into the overall thermal structure.

Pudov et al. (1978) obtained detailed data on the subsurface structure of the upper ocean in the wake of a tropical cyclone during the special USSR project Typhoon '75. They conducted hydrographic surveys across the track of Typhoon Tess to depths of 500 to 1000 m. Information gathered during this survey showed that the swath of cooled surface water along the track was 400 km wide, with 3° C to 4° C decreases

(Figure 6.2a). As noted in previous studies, they observed the maximum decrease to the right of the storm track. A vertical cross section of the Tess data showed intense upwelling and cooling to significant depths (Figures 6.2b and 6.2c), accompanied by warming at the surface layers away from the center of the storm.

The warm layer began near the surface at the radius of maximum winds, then deepened with increasing distance away from the center of the storm. Pudov et al. summarized that downwelling apparently produced this warm layer. Black (1983) also observed this pattern in data from Typhoon Ella in 1978. He reports a negative annulus of wind stress curl may produce the warming at the outer regions of the storm.

2. Upper Ocean Current

The available data on ocean currents forced by tropical cyclones is very sparse. Most observations are obtained when tropical cyclones happen to pass near an already deployed oceanographic sensor or through limited airborne-expendable current profiler (AXCP) measurements.

a. Mixed Layer Currents

Shay et al. (1992) examined the three dimensional upper-ocean current responses produced by Hurricane Gilbert in the Gulf of Mexico using data from 78 AXCPs. The most prominent feature of the response was a significant right-hand bias in the upper ocean current amplitude (Figure 6.3). The magnitudes of the current velocities

in the mixed layer reached more than 1 m/s.

Price (1981) attributes this right-hand bias in the current amplitude to an inherent asymmetry in the coupling between the wind stress of the moving cyclone and the wind-driven, mixed layer currents. On the right side of the storm track the wind stress turns clockwise with time when viewed from the ocean. For a typical storm translational speed, this clockwise rotation is nearly in phase with the local inertial turning rate. Currents and wind stress remain nearly aligned during the passage of the storm, which enhances the currents on the right side of the storm track. On the left side of the track the wind stress turns counterclockwise with time, opposite to the current inertial rotation. This causes the currents on the left side to be weaker than the right side.

This mixed layer current structure produces a unique convergence and divergence pattern in the wake of the storm, which in turn create significant vertical velocities and strong upwelling and downwelling.

b. Thermocline Currents

Thermocline currents are opposite to those in the mixed layer. Surface divergence and upwelling produces a subsurface pressure anomaly (Price, 1994). Subsurface current flow converges inward toward this pressure anomaly, producing very strong current shear between the mixed layer and thermocline. The effect of this strong shear is to reduce the Richardson number, R_i , which decreases the vertical stability and enhances upwelling.

$$R_i(z) = \frac{N^2(z)}{u_z^2 + v_z^2}, \quad (6.1)$$

where $u_z^2 + v_z^2$ is the vertical shear of the current and $N^2(z)$ is the usual Brunt-Vaisala frequency. Shay et al. (1992) noted this significant current shear between the mixed layer and thermocline in the Hurricane Gilbert data (Figure 6.3).

c. Upwelling and Downwelling

The inertially rotating wind-driven currents are highly divergent, which forces an oscillating vertical velocity at the base of the mixed layer with a near inertial period. This oscillating vertical velocity produces a cycle of strong upwelling and downwelling. The first upwelling cycle occurs behind the storm center due to the storm's forward motion. Ginis (1995) calculated an estimate of this distance from the equation

$$\lambda = \frac{\pi - \alpha}{f} U_h, \quad (6.2)$$

where α is the storm inflow angle and U_h is the storm's translational speed and λ is one half of the wavelength of the generated inertial wave.

Ocean sensors recorded the first velocity structure measurements in the Gulf of Mexico during the passage of Hurricane Eloise (Withee and Johnson, 1976). This data set clearly showed the generation and rapid decay of these near-inertial motions at 53 m, roughly the mixed layer depth, before and after the passage of the storm.

Shay and Elsberry (1987) examined a more extensive set of observations collected during the passage of Hurricane Frederic (1979). Frederic passed within 80 to 130 km of an array of current meters, CMA1, CMA2, and CMA3, deployed at depths of 100 to 470 m. Shay and Elsberry observed near inertial waves throughout the water column (Figure 6.4). They noted that mixed layer currents oscillated with an 80 to 90 cm/s amplitude for about four inertial periods, then rapidly decreased.

3. Sea Surface Elevation

Actual real time observations of the sea surface elevation are difficult to obtain. The usual means of direct observation of the sea surface elevation is through satellite altimetry. The sea surface coverage by satellite altimetry sensors is limited however, since the typical altimeter only covers a very narrow swath and has a long repeatability cycle. The storm modified sea surface elevation field is therefore usually obtained by modeling the physical processes that produce the elevation changes. Five different physical processes affect the sea surface elevation, (1) the 'inverted barometer effect', (2) wind stress divergence, (3) wind stress curl, (4) the geostrophic balance of the barotropic currents, and (5) the baroclinic effect caused by the ocean thermodynamic changes (Ginis and Sutyrin, 1995; Ginis, 1995; Geisler, 1970).

a. Inverse Barometer Effect

The 'inverse barometer effect' is produced by the storm's atmospheric

pressure gradient. Lower pressure at the center of the storm produces a set-up of the sea surface in this region. The amount of this atmospheric set-up may be calculated using the equations

$$\frac{\partial \eta}{\partial x} = \frac{1}{\rho_0 g} \frac{\partial p_a}{\partial x}, \quad (6.3)$$

$$\frac{\partial \eta}{\partial y} = \frac{1}{\rho_0 g} \frac{\partial p_a}{\partial y}, \quad (6.4)$$

(Ginis and Sutyrin, 1995), where η is the sea surface elevation, ρ_0 is the ocean density and p_a is the atmospheric pressure. The solution of these equations suggests that this set-up is approximately 1 cm per millibar of pressure change. This set-up however is localized to the central portion of the storm and travels with it.

b. Wind Stress Curl Effect

The tangential component of the storm wind produces a cyclonic wind stress curl, strong surface divergence at the center of the storm and sea surface set-down. In deep water this set-down will lower the sea surface according to the equations

$$\frac{\partial \eta}{\partial x} = \frac{\tau_x}{\rho_0 g h}, \quad (6.5)$$

$$\frac{\partial \eta}{\partial y} = \frac{\tau_y}{\rho_o g h}, \quad (6.6)$$

(Ginis and Sutyrin, 1995) where τ_x, τ_y are the wind stress components and h is the water depth. For a storm with a wind stress of 1 N/m^2 , approximately 25 m/s wind, a storm size R_0 of 800 km , and a water depth of $2,000 \text{ m}$ the wind stress curl will produce a set-down of 4 cm .

c. Wind Stress Divergence Effect

In a cyclone-centered coordinate system the change in the sea surface elevation due to wind stress divergence is given by the equation

$$\zeta_d(r) = - \int_r^\infty \tau_r dr, \quad (6.7)$$

where τ_r is the radial wind stress (Ginis and Sutyrin, 1995). Since the radial component of the tropical cyclone wind is negative, directed inward toward the center of the storm, this produces convergence at the storm center and a rise in the sea surface elevation. This set-up also moves with the storm center.

d. Barotropic Current Effect

After passage of the storm, geostrophic adjustment toward a balance of the mass sea surface elevation and depth-averaged barotropic current field takes place. A

cyclonic barotropic current field, elongated in the along-track direction, is produced by the moving cyclone (Ginis and Sutyin, 1995). The effect of this cyclonic wind stress curl is to cause mass divergence, generating a trough in the wake of the storm.

Because of the inertial cycle of the divergent surface currents, the local maxima of the depression will oscillate at a near-inertial period. Studies by Ginis and Sutyrin (1995) indicate that the cross track horizontal scale of this barotropic response is comparable to the storm size.

e. Baroclinic Current Effect

Upwelling and cooling in the storm's wake will produce a semi-permanent subsurface baroclinic ridge in the along-track direction of the storm (Ginis, 1995) and a compensating sea surface set-down. Geisler (1970) showed that the amplitude of this ridge, and therefore the set-down, will increase for slower moving storms since temperature decreases will be greater for these storms. Because maximum temperature decreases occur to the right of the storm track, the maximum set-down of the sea surface produced by this ridge will be offset to the right of the storm track.

B. NUMERICAL MODELING OF OCEAN RESPONSES

Tropical cyclones generate highly complicated ocean responses. In addition to near-inertial currents, they also produce strong non-oscillating currents. Further,

entrainment mixing due to turbulence, convective overturning and velocity shear across the mixed layer causes significant mixed layer deepening. Therefore, the ocean response to a tropical cyclone is a combination of highly nonlinear, three-dimensional processes. Extensive numerical calculations are required to simulate these responses fully.

Researchers have used two types of models to simulate these responses, layer and level models. Level models have a distinct advantage over layer models however. Level models may be set up with a fine enough vertical grid spacing to achieve the necessary resolution to simulate the complicated vertical dynamic and thermodynamic structures produced by a tropical cyclone.

1. Simulations of Ocean Responses Using Level Models

Level models have been used by Chang (1985), Shay et al. (1990) and Price et al. (1994) to simulate the ocean response to tropical cyclone forcing. These models are based on the standard set of primitive equations on a Beta plane. Price et al. simplified the system of equations by using the reduced gravity approximation and ignoring the horizontal diffusion.

Each of these three models parameterize vertical mixing differently. The Price et al. model assumes that the storm will mix the upper ocean density and velocity vertically to satisfy three stability parameters. In the Chang model, which was also used by Shay et al., the eddy diffusivity (K_z) depends on the Richardson number and a specified mixing length. None of these models includes realistic bottom bathymetry or horizontal

topographic boundaries.

a. Chang (1985) Ocean Model

Chang tested an asymmetrical level model that included a free surface and flat bottom. The vertical model resolution included 51 grid points between the surface and 1500 m, with the highest resolution of 5 m near the surface. Chang applied a stationary hurricane forcing for 48 hours, then removed it and ran the model for another 96 hours to study the post-storm adjustment.

The results of this study showed that the ocean current response extended to a great depth. The maximum barotropic velocity reached 19 cm/s at 48 hours and was a large part of the deep ocean response. During the post-storm period near-inertial oscillations with large amplitudes extended over much of the ocean depth.

b. Shay et al. (1990) Ocean Model

Shay et al. used Chang's model to simulate the ocean response to a moving hurricane. The total model depth was 610 m, with a flat bottom. They moved an idealized forcing, simulating Hurricane Frederic, through the model domain with a steady 5.5 m/s westward translational velocity.

The model generated maximum mixed layer velocities of about 140 cm/s to the right of the storm track. The simulated thermocline currents in the cross track direction were 180° out of phase with the mixed layer currents, similar to observations of

Hurricane Gilbert reported by Shay et al. (1992). The depth of the current reversal increased to 200 m after one inertial period. The mixed layer temperature decreased by 1.0° C to 1.2° C at $x = R_m$ following storm passage. The model also generated a significant barotropic response, with a 20 cm deep sea surface trough formed along the storm track.

c. Price et al. (1994) Ocean Model

Price et al. simulated the ocean response to three hurricanes, Norbert and Josephine (1984) and Gloria (1985), using the Chang (1985) model. The vertical grid spacing of the model was 10 m within the upper 150 m and increased to 50 to 100 m at depths down to 1000 m. Vertical mixing was the only subgrid scale upper-ocean process simulated by the model.

In all three of the simulations near-inertial currents dominated the ocean response. A review of temperature data from AXCP and model profiles showed that much of the vertical mixing occurred within the upper thermocline, rather than solely in the deepening mixed layer. Price et al. also tested the wind stress calculated from a bulk formula using the drag coefficients of Large and Pond (1981) with flight level winds. They compared the simulated upper ocean transport in the top 80 m layer with the transport calculated using AXCP data. They concluded that modeling of the ocean

current response to a hurricane could be accomplished using the wind stress estimated from aircraft measured winds and the bulk formula, to an accuracy of ~20%.

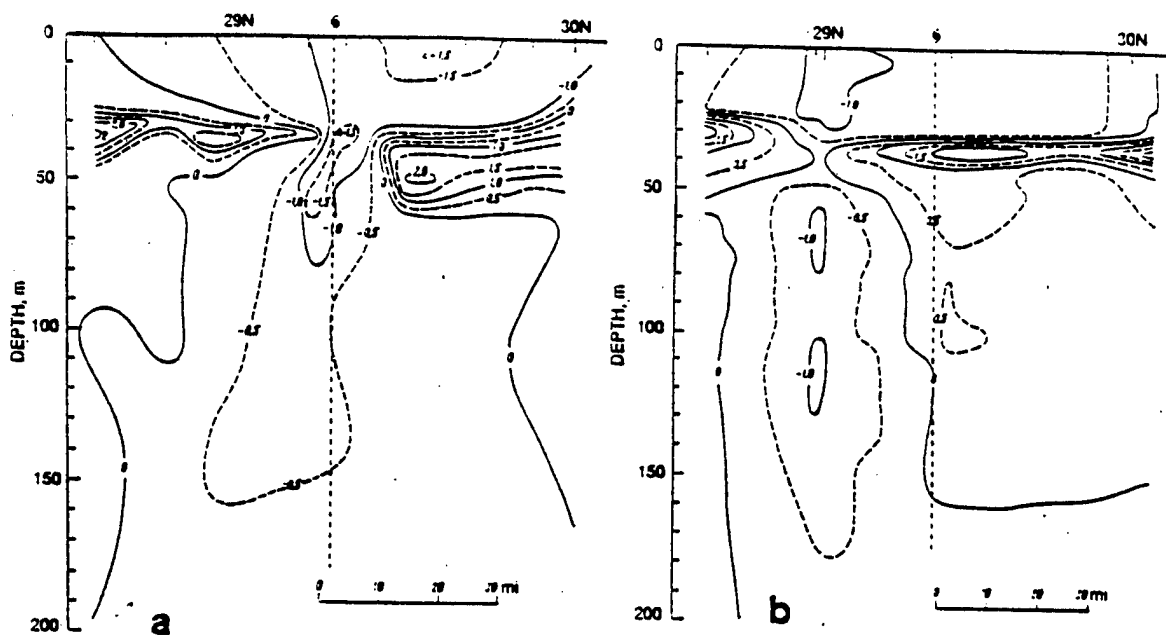


Figure 6.1. SST departure ($^{\circ}\text{C}$) from pre-storm analysis for Hurricane Ella on 2 September 1978. Storm positions at 6-h intervals are indicated by open circles with UTC labeled. Open triangles indicate AXBT observations. Dashed line indicates location of R/V Akademik Kurchatov measurements (From Black, 1983).

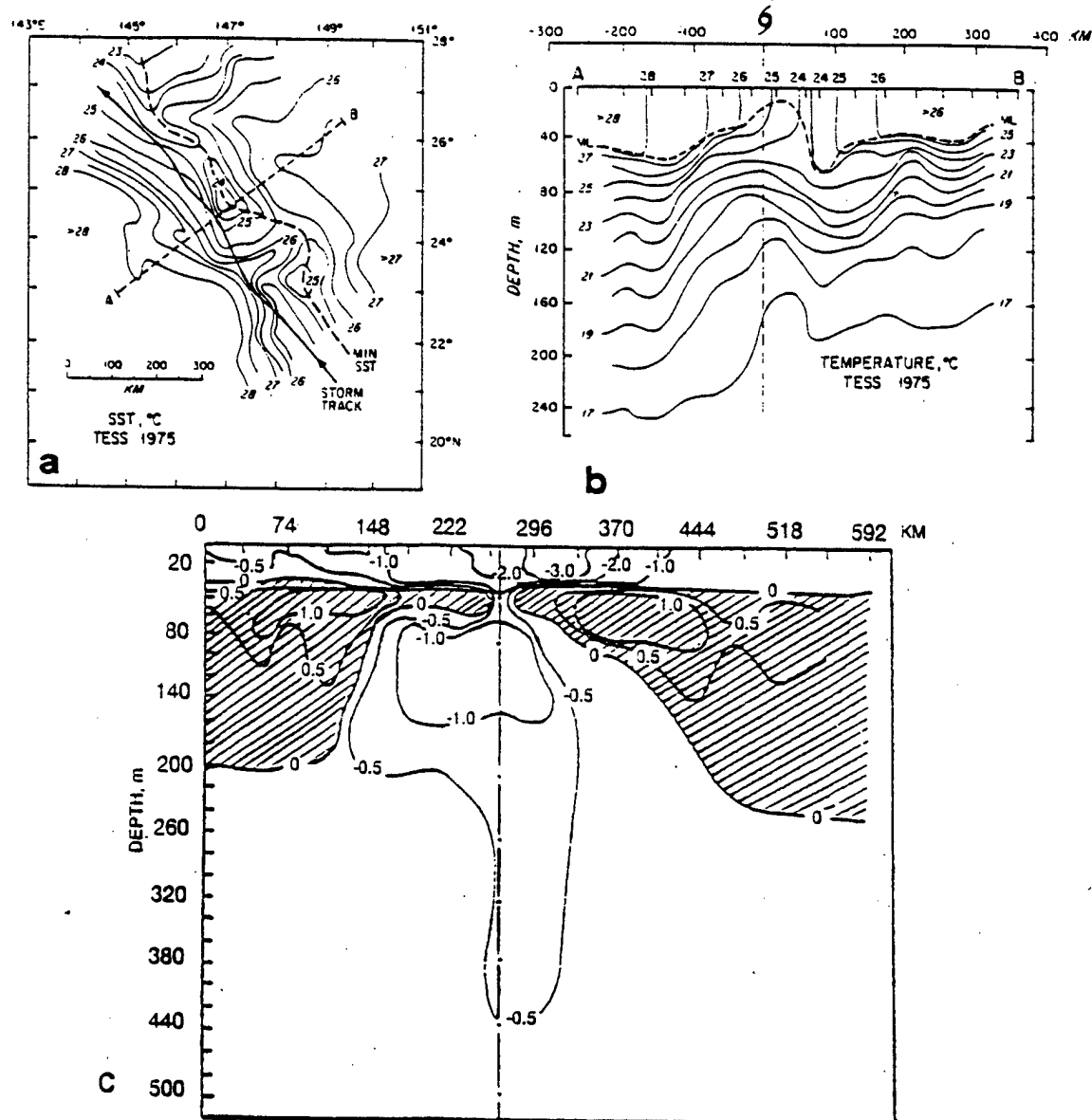


Figure 6.2. (a) SST around Typhoon Tess observations were made at 20 km intervals along 5 sections 3-5 days after storm passage. (b) Temperature ($^{\circ}\text{C}$) along section AB in (a). (c) Temperature changes ($^{\circ}\text{C}$) along section AB relative to climatological values (From Pudov et al., 1978).

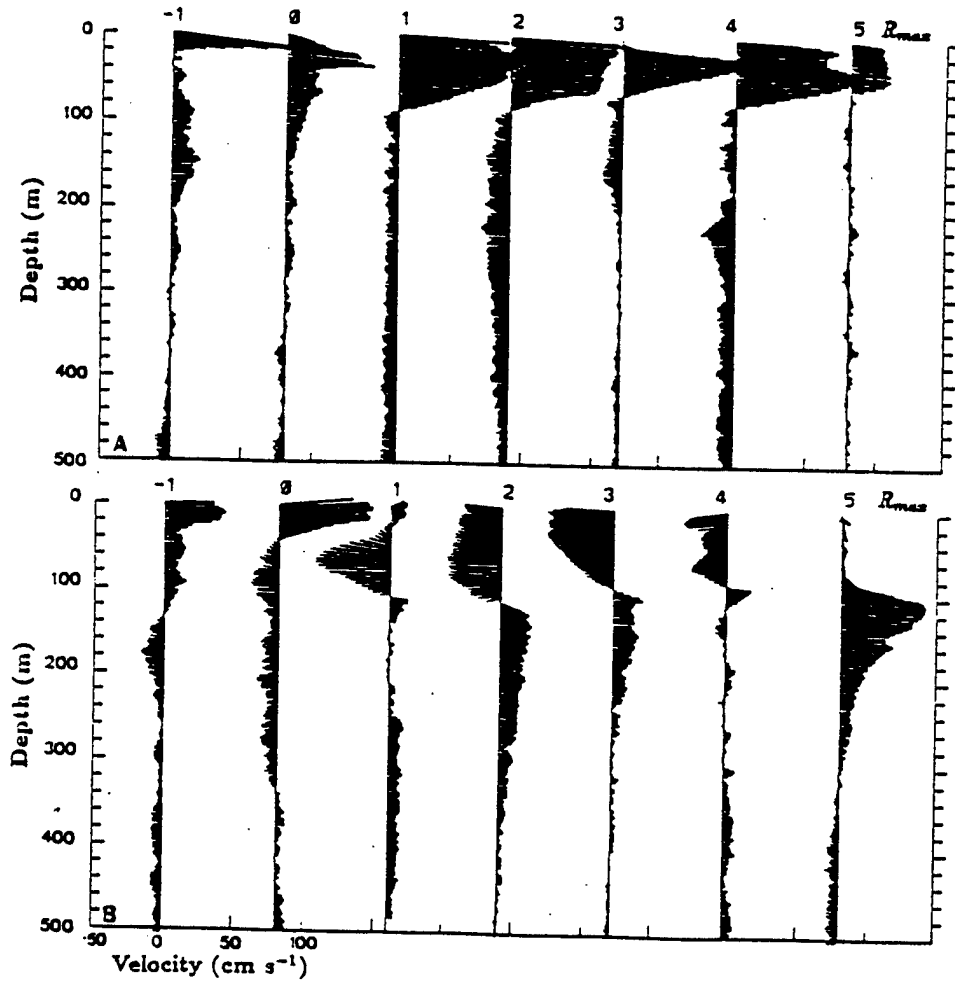


Figure 6.3. Vector stick plot of the observed velocity profiles, cm/s from (a) Wake I and (b) Wake II observations of Hurricane Gilbert. Each current profile is displaced by 85 cm/s from $-R_m$ to about $5 R_m$, with velocity scale in the lower left corner (From Shay et al., 1992).

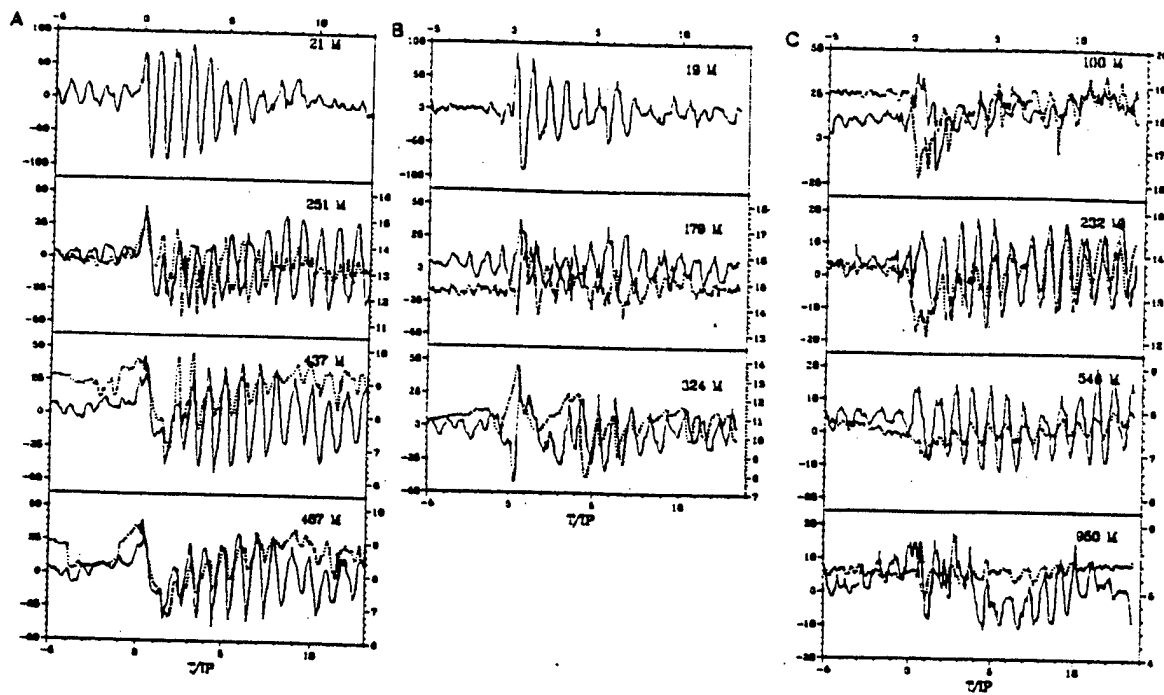


Figure 6.4. Along-track velocity (cm/s) temperature (°C, dashed) time series from moored arrays (depth in meters) at (a) CMA3, (b) CMA2 and (c) OTEC sites from 7 to 25 September 1979. Time 0 corresponds to time of closest approach to sensor. (From Shay and Elsberry, 1987)

VII. NUMERICAL SIMULATION OF SCS RESPONSE TO TROPICAL CYCLONE ERNIE (1996)

The POM was used to investigate the ocean response to forcing by Tropical Cyclone Ernie (1996). This is a three-dimensional model developed by Blumberg and Mellor (1987) with hydrostatic and Boussinesq approximations and the following features: (a) a staggered scheme, (b) sigma coordinates in the vertical, (c) a free surface, (d) a second-order turbulence closure model for the vertical viscosity (Mellor and Yamada, 1982), (e) horizontal diffusivity coefficients calculated by the Smagorinsky (1963) parameterization, and (f) split time steps for the barotropic (25 seconds) and baroclinic modes (900 seconds). This application of the model did not include tidal forcing and river outflow. No observed atmospheric thermal and salinity flux data was available, therefore restoring forcing was applied using a restoring rate of 0.7 m/day, which is equivalent to a 43 day restoration of a 30 m deep layer.

Solid lateral boundaries were defined using a free slip condition for velocity and a zero gradient condition for temperature and salinity. The model did not allow advection or diffusions of these properties across these boundaries. Open boundaries were treated as radiative boundaries. Volume transport through the Luzon Strait, Taiwan Strait and Gasper/Karimata Strait was defined according to observations by Wrytki (1961) (Table 5.2).

A. NUMERICAL SIMULATION

1. Pre-experimental Stage

The model was integrated for 34 months and three days from an initial at rest state with three-dimensional climatological January temperature and salinity fields (Levitus, 1984), using climatological monthly mean wind stress forcing (Hellerman and Rosenstein, 1983). The study took the final state of the integration as the initial condition for November 4, 1996.

a. *Model Initial State Verification*

The model initial state for November 4, 1996 was verified using prior study of mean monthly surface current (Wyrtki, 1961) and temperature patterns (Su and Weng, 1995) and satellite multichannel sea surface temperature (MCSST) data from the polar orbiting Defense Meteorological Satellite Program (DMSP) satellites .

Due to extensive cloud cover associated with Ernie, MCSST data used to verify the model initial SST fields during the November 3 to 6 period was primarily concentrated in the northern SCS along the Vietnam and Chinese coast (Figure 7.1). RMS temperature errors between the model SST and the MCSST fields for this period range from 0.59°C to 0.81°C (Figure 7.2). A comparison of the scaled RMS temperature errors, the ratio of the RMS error to the standard deviation of the observed MCSST, ranges from 0.61°C to 0.78°C . This suggests that the model's initial SST field

was consistent with the actual state of the SCS surface temperatures for this region.

The SST of those regions obscured by clouds was compared with past water mass studies by Su and Weng (1994) (Figure 2.3). A subjective analysis of the model SST field in the northern SCS (Figure 7.3) shows that it is consistent with these studies. The model generated winter SST and temperature patterns similar to Su and Weng's observations, with isotherms aligned parallel to the Asian coastline. A narrow band of minimum temperatures was found along the coast, produced by offshore wind flow and coastal upwelling.

Since no surface current observations were available, a subjective comparison between the model November 6 surface current pattern (Figure 7.5) with winter current patterns from studies by Wyrtki (1961) (Figure 2.5) was performed. This comparison was used to verify that the surface velocities were consistent with normal winter patterns. The comparison shows very good agreement. The model depicted a closed cyclonic gyre in the central SCS, with a westward intensification along the coast of Hainan Island and Vietnam. Current speeds off the coast of Vietnam exceed 140 cm/s. A cyclonic gyre was also generated in the Gulf of Thailand. These patterns and current intensities are consistent with Wyrtki's prior analysis.

The model developed three cyclonic eddies. One eddy was found in the central southern SCS near 5° N, 108° E, another was found off the west coast of Luzon near 16° N, 116° E and a third off the east coast of Vietnam near 13° N, 109° E. The South China Sea Institute of Oceanology (SCSIO) has reported this eddy off Vietnam as

a usual winter feature.

2. Numerical Simulation

After the pre-experimental stage, the SCS Tropical Cyclone Wind Model forced the ocean model, simulating Tropical Cyclone Ernie, for eighteen days. This wind model attempted to simulate realistically not only the movement of the storm, but its size and intensity variability. On the eighteenth day the storm passed out of the model domain into the Bay of Bengal and the model run was stopped. Three-dimensional u , v and w and temperature and salinity fields and two-dimensional depth averaged u and v velocity fields along with sea surface elevation fields were outputted from the model every six hours for later analysis.

B. ANALYSIS SCHEME

An analysis of the ocean responses to the storm forcing, including the tendencies of the sea surface temperature, elevation and currents, and the subsurface temperature and current structure, was done. This analysis compared previous observational and numerical modeling studies of ocean responses to tropical cyclones to determine the SCS POM's ability to simulate ocean responses to forcing by Tropical Cyclone Ernie (1996). Fields for November 4, the model initial state, were used to compute temperature and sea surface elevation anomalies.

Due to the large size of the SCS model domain, approximately sixteen degrees longitude by twenty eight degrees latitude, a detailed analysis of the fields covering the entire basin was not done. Instead, a general analysis of the basin wide sea surface temperature, elevation and currents was conducted. In addition, three limited area regions were selected for detailed analysis of the ocean response. The criteria for selecting these areas included the behavior of the storm and the proximity of the storm to geographic features, since coastal and bottom interactions may significantly alter the ocean responses.

1. Analysis Areas

a. Area One

Area One is an eight degree longitude by eight degree latitude region to the southwest of Luzon (Figure 7.7). This region includes the coastline of the northern Philippine islands and has water depths reaching 4000 m. The storm moved northerly through this region along the coast of Luzon for about one day. Ernie reentered this region three days later from the northeast after looping over the northern SCS and Luzon. Average storm translational speeds were 5 to 6 m/s. Storm strength was moderate, with JTWC analyzed wind speeds of 20 to 24 m/s.

b. Area Two

Area Two is an eight degree longitude by eight degree latitude open ocean region to the northwest of Luzon (Figure 7.7). This region includes the coastline of

southern Taiwan and has depths reaching 3800 m. The storm was quasi-stationary in this region for about twenty four hours. Storm strength while Erine moved through the area was moderate, with JTWC analyzed wind speeds of 24 m/s.

c. Area Three

Area Three is an eight degree longitude by nine degree latitude region to the east of Vietnam (Figure 7.7). The region includes the coast of central Vietnam and has water depths extending to 4000 m. The storm moved southwesterly through this region at 5 to 6 m/s. The storm strength was weak to moderate, with JTWC analyzed wind speeds of 15 to 20 m/s.

C. SIMULATION RESULTS

1. Overview

An overview of the model results suggests that the simulated ocean response to forcing by Tropical Cyclone Ernie is consistent with both observations and previous numerical studies.

Surface currents (Figures 7.5 and 7.6) exhibited the strong asymmetrical pattern seen by Shay et al. (1992) in Hurricane Gilbert data, with enhanced flow to the right of the storm track. Maximum current velocities were 139 to 199 cm/s. The most significant example of this pattern occurred from November 14 to 17 as the storm moved steadily to

the southwest over the central SCS. The model generated a ‘fan shaped’ pattern of anticyclonic-rotating near-inertial currents to the right of the storm track, which has been previously seen in AXCP data and reproduced in other numerical models (Ginis et al., 1992). Currents to the left of the storm track rotated cyclonically and were significantly weaker.

SST decreases were also very consistent with observations and modeling results (Figures 7.3 and 7.4). Maximum surface cooling 2° C to 3° C was found to the right of the storm track as the storm moved northerly along the coast of Luzon. The model formed an almost circular cold SST anomaly, -2° C, with a radius of 250 to 300 km near 18° N and 118° E, in the region where Ernie became quasi-stationary on November 10 and 11. A second similar feature was formed off the coast of Vietnam near 13° N and 111° E. This region is associated with significant divergence in the near-surface ‘fan shaped’ current field to the right of the storm track.

Eleven XBT observations were taken to depths of 100 m in the central SCS from November 9 to 12 (Figure 7.8), before Ernie entered the basin. Overall these observations indicate that the model was initialized and performed well in this region during these days. The total RMS SST error was very low, only 0.6° C (Figure 7.9). This error gradually increased to about 2° C near 50 m, the average base of the mixed layer in the region, then remained constant. This increase in RMS error is due to the poor vertical resolution of in the upper oceanic layer.

MCSST data also shows good agreement between the model results and the actual

state of the SCS. MCSST observations are limited to those regions that were cloud free. Therefore, most of the observations from November 4 to 12 are concentrated in the northern or western portions of the basin (Figure 7.1), away from Ernie's location. RMS errors between the model SST field and the MCSST observations average 0.6° C (Figure 7.2), similar to the XBT comparisons. RMS errors from November 13 to 17, when cloud cover was diminished, ranged between 0.6° C and 0.9° C. Scaled RMS errors are all less than 0.75° C and averaged about 0.5° C.

The model created sea surface depressions to the right of the storm track as the storm entered the SCS to the southwest of Luzon on November 8. Another large depression of 20 cm was formed around the region where Ernie became quasi-stationary on November 10 and 11. The model also produced sea surface set-ups along the northwest coast of Luzon on November 10 and 11 and the southeast tip of Vietnam on November 16. Divergent surface currents caused by strong cyclonic wind stress curl produced significant on shore flow and set-up in these regions.

Satellite altimetry observations were compared with the model sea surface elevation. Both sets of data were averaged for the fourteen day period of the model run when Ernie moved through its domain, resulting in two-dimensional mean sea surface elevation fields. This technique was used to remove the tidal signal from the altimetry data. Over the fourteen day period satellite altimeters observed 38% of the model domain (Figure 7.10d). The results indicate that the mean model sea surface elevation field was consistent with the observed mean field. The mean elevation error was -0.74 cm, the

maximum error was 156.6 cm and the minimum error was -176.9 cm (Figure 7.10a). However, a review of scatter plots of the model elevation and the elevation error (Figures 7.10b and 7.10c) indicates that larger errors are associated with the extreme sea surface elevations, suggesting that the model produced extreme elevations that were too large. A line fitted linearly through the satellite observed and model elevation scatter plot (Figure 7.10c) suggests that the model extreme elevations, which occurred along the basin's coastlines, was 300% too large. These large errors are most likely due to the treatment of the shoreline as a solid boundary. No inshore movement of onshore flowing water is allowed, therefore water accumulates along the coast, producing high sea surface elevations.

2. Area One

Ernie first entered Area One late on November 7 from the southeast after passing through the central Philippine Islands. The storm size, R_θ , was approximately 850 km. The radius of maximum winds, R_m , was 20 km and the maximum wind speed was 25 m/s. Initial ocean responses occurred almost immediately as the storm crossed the coast.

Outflow from the storm produced very strong divergent upper layer currents (Figures 7.11 and 7.12) and significant upwelling along the coast. A strong barotropic cyclonic circulation was noted near 13° N on November 8 in a cross section of the u velocity field taken along 119.5° E (Figure 7.13). Velocities were 60 to 100 cm/s at the surface, decreasing to 20 cm/s at 100 m. The model produced very intense vertical

current shear across the base of the mixed layer, with 180 cm/s northerly flow in the mixed layer and 100 cm/s southerly flow in the thermocline (Figure 7.13). Shay et al. (1992) saw a similar pattern in current meter data from Hurricane Gilbert (Figure 6.3). This 180° phase reversal between the mixed layer and thermocline indicates that wind stress generated the near-surface currents, whereas pressure gradient effects generated the thermocline currents (Price, 1983).

Along the 119.5° E cross section the v velocity field shows very strong divergence at 40 to 50 m. This divergence generated an intense, narrow upwelling plume, with velocities reaching 300 cm/hr at 100 m near 13° N, 119.5° E. This intense upwelling produced large SST and subsurface temperature changes. SST decreases of 1.5° C were noted to the right of the storm track (Figures 7.14 and 7.15), which is consistent with past observation of tropical cyclone SST cooling (Jordan, 1964; Hazelworth, 1968; Black, 1983). Subsurface temperature changes were more pronounced however. The largest subsurface temperature changes occurred to the right of the storm track near 50 m, the approximate depth of the thermocline, with a decrease of 3.5° C (Figure 7.16). Pudov et al. (1978) reported a similar subsurface cooling pattern in the wake of Typhoon Tess (Figure 6.2). The storm produced subsurface cooling of up to 1.5° C to a depth of 200 m.

Along the coast, the model generated an oblong sea surface depression of 15 to 20 cm by November 8 (Figure 7.17). Strong surface divergence and coastal effects caused by storm wind flow may produce this depression. Offshore upper layer flow is prominent in the 119.5° E v velocity field cross section (Figure 7.13). Intense upwelling was found

along the coast, with 100 cm/hr vertical velocities at 75 m (Figure 7.13). Baroclinic effects, caused by the 3.5° C cooling near the coast at 50 m, also likely contributed to the set-down.

By 00 local time on November 9 Ernie was located near 16° N, 118° E. The model produced a crescent shaped pattern of SST decrease to the right the storm track. This pattern is very similar to SST patterns observed in observational studies by Pudov et al. (1978) and Black (1983). Maximum cooling was 2.5° C at 80 km from the track, approximately $1.5R_m$.

The model formed a sea surface trough, with maximum depressions of 15-20 cm, to the right of the track, in the wake of the storm (Figures 7.17 and 7.18). The trough extends 100 to 150 km on either side of the storm track, 2 to $3R_m$, which is similar to modeling results obtained by Shay et al. (1990). Along the western coast of Luzon sea surface set-up of up to 15 cm occurred due to onshore current flow produced by the upper ocean divergent storm current.

Ocean responses are more pronounced on November 9. Strong surface divergence, vertical current shear and upwelling was still evident in the velocity cross sections (Figures 7.19 and 7.20). Mixed layer and thermocline currents reversed however. Flow was to the southeast and onshore in the upper layer and northwest and offshore in the thermocline. This reversal pattern, which Shay et al. (1990) and Price (1994) documented in previous observational studies of other tropical cyclones, is a signature of the inertial currents excited by the storm. A power density spectrum of the

near-surface u and v velocities at 13° N, 119.5° E (Figure 7.21d) indicates that they have a period of 2.1 days, which is very close to the local inertial period at 13° N of 2.2 days.

Coastal interactions with this current pattern appear to have produced a 84 cm/s subsurface jet flowing parallel to the coast at 75 m on November 9 (Figure 7.20). A time series of the u and v velocities at 13° N, 119.5° E (Figure 7.21a,b,c) suggests that this feature is related to the oscillating surface currents. When the surface currents are onshore to the east and southeast, coastal downwelling occurred and a strong northwesterly subsurface jet was produced. When the currents reversed and became offshore to the west and northwest, coastal upwelling occurred. The subsurface jet reversed to the southeast and weakened slightly.

A divergent surface outflow caused sea surface rises along the coast of up to 25 cm extending along the entire west coast of Luzon. Subsurface, the upwelling plume expanded and moved farther to the north with the storm. Upwelling velocities in excess of 200 cm/hr were centered near 14° N in the 119.5° E cross section and 119.5° E in the 13° N cross section (Figures 7.19 and 7.20). The latitudinal extent of the upwelling plume expanded northward, along the storm's track, to cover a 200 km long region. Although upwelling velocities had decreased, subsurface cooling had deepened and increased. Cooling at 60 m exceeded 4° C (Figure 7.22). Black (1983) also noted this one day delay in maximum subsurface cooling in observational studies of ten years of storm data. Along the coast, 400 km to the southeast of the storm, intense downwelling occurred. The 26° C isotherm, which had been at 40 m on November 8, had been

depressed to near 75 m. Warming of 1.5° C was produced at 100 m.

The storm continued moving to the north, passing out of Area One on November 10. A wake of lower SST and sea surface elevation stretched southward along its entire track to the coast.

Ernie reentered the area on November 13, after looping over the northern SCS and Luzon, crossing over its previous track near 16° N. SST cooling and sea surface set-down was not as intense during the second pass through the region, even though the storm intensity had only decreased by 4 m/s. SST cooling was only 1° C and set-down 8 cm along its track.

These modest responses may be attributed to interaction with the near-inertial oscillations produced by Ernie during its first pass through the region. As the storm initially moved through the region, it set up near-inertial oscillations in the velocity and temperature fields. This oscillation can best be seen in the 30 m vertical velocity fields for November 10 to 12 (Figures 7.23 and 7.24) as the completed reversal of the velocity fields every twenty four hours. The alternating convergence and divergence patterns in the surface current fields to the right of the storm track on November 14 to 17 are also an indication of this near-inertial current. The approximately 450 km half-wavelength of this current pattern agrees quite well with a calculated theoretical value of the inertial half-wavelength of 470 km, using the formula (Ginis, 1995)

$$\lambda = \frac{\pi - \alpha}{f} U_h, \quad (7.1)$$

where α is the storm inflow angle and U_h is the storm's translational speed and λ is one half of the wavelength of the generated inertial wave. When the storm reentered the region the second time, the forcing imparted to the water mass was out of phase with the initial forcing. This is evident in November 13 time series of the temperature field at 16° N, 118.6° E (Figure 7.25). The warming trend from the surface down to 40 m on that date was less than during the previous inertial period due to upwelling produced by the storm moving through the region again. This is an indication of an out of phase component being added to the preexisting near-inertial oscillation.

3. Area Two

Ernie entered the area on November 9, moving northerly at 7 m/s. Ernie rapidly reduced its forward translational speed and became quasi-stationary near 20° N, 118° E on November 10. Storm size, R_θ , was 718 km and the radius of maximum winds, R_m , was 72 km.

Initial influences of Ernie on the area occurred on November 8 with a slight SST rise in a pre-existing warm surface anomaly off the northwest tip of Luzon. This region appears to be a zone of convergence between a northward flowing coastal current along the western coast of Luzon and the inflow of a branch of the warm Kurishio Current through the Bashi Channel (Figures 7.26 and 7.27). As the storm entered the SCS, divergent flow in the surface layer enhanced this northward coastal current, increasing the convergence off the tip of Luzon and raising SST nearly 1.5° C (Figures 7.28 and 29).

Northerly divergent storm flow into the northern SCS shelf region off the coast of China also raised the sea surface elevation over this region by 5 to 7 cm.

SST and sea surface elevation anomaly patterns, which had been concentrated in the storm's wake, quickly became nearly concentric with the storm's position as it went quasi-stationary (Figures 7.28 through 7.31). Maximum SST cooling, 1° C, and sea surface depression, 15 cm, occurred near the center of the storm.

Cross sections taken along 19.6° N and 117.7° E indicate that upper ocean current patterns were still highly divergent (Figures 7.32 and 7.33). Intense upwelling, with vertical velocities of 170 cm/hr to a depth of 200 m beneath the center of the storm, caused subsurface cooling of 2° C at 75 m (Figures 7.34 and 7.35). A time series of the velocity fields near the position where the storm became quasi-stationary (Figure 7.36a,b,c) shows persistent southwesterly upper ocean flow and upward vertical velocities for the period the storm was quasi-stationary. The power density spectrum of these fields (Figure 7.36d) indicates that near-inertial oscillations in these fields did occur. A strong peak in the spectrum at the 1.4 day period closely corresponds to an inertial period at this position. The second peak in the spectrum at 1.6 days was produced by wave energy propagating into the region from the south. After leaving this area the storm moved to the southeast, then westerly and crossed its track to the south of this region near 16° N. The 1.6 day period corresponds to an inertial wave generated near 17° N, approximately the latitude that Ernie where this crossing occurred.

At a distance of 150 to 250 km from the center of the storm significant

downwelling occurred while Ernie was quasi-stationary, with 60 to 100 cm/hr vertical velocities (Figures 7.37 and 7.38). Pudov et al. (1978) saw this pattern of downwelling on the periphery of the storm in data from Typhoon Tess. The Tess data also showed that subsurface warming occurred in association with this downwelling, however none was noted in this model simulation of Typhoon Ernie. Warming did occur at 121° E in the 19.6° N temperature cross section (Figure 7.40) however. This was due to downwelling in the region, but there is uncertainty about whether this downwelling and warming was storm induced. This region is at the edge of the model domain and is an open boundary in the Bashi Channel. A mean seasonal mass transport through this boundary was used in the model run since no studies have been conducted concerning transport through this boundary under tropical storm forcing, therefore ocean responses in this region are highly suspect.

Ernie began moving to the southeast on November 12 toward northern Luzon. Divergence intensified as upper ocean currents increased due to increased wind stress caused by the forward motion of the storm. Upper-layer horizontal flow to the south at 80 cm/s and north at 20 cm/s along the 117.7° E velocity cross section (Figure 7.37) produced 140 cm/hr upward vertical motions to the southwest of the storm center. This caused the intensity of the maximum SST cooling and sea surface depression to increase quickly and their locations to shift to the right rear quadrant of the storm. SST cooling reached a maximum of 2° C and the sea surface depression increased to 20 cm (Figures 7.28 and 7.29). Subsurface cooling also increased to 3° C near 60 m (Figures 7.39 and

7.40).

The model fields depict a subsurface northerly jet at 50 m near 121° E in the 19.6° N velocity cross section (Figure 7.38), however this is most likely another artifact of the open boundary problem in this region.

During the next five days the SST anomaly gradually decreased, reducing to less than 1° C. The nearly circular sea surface depressions generated by the storm however remain steady at 15 to 20 cm. A review of the temperature time series near the storm's quasi-stationary position, 19.6° N, 117.7° E, (Figure 7.41) indicates that temperatures had initially rapidly decreased at all levels, from the surface down to 500 m. SST then gradually increased to a nearly pre-storm temperature as the storm moved away from the area to the southeast. This SST warming may be too large, however, due to the model's use of a 0.7 m/day thermal restoring rate lacking atmospheric thermal flux data.

4. Area Three

Ernie entered this region from the northeast early on November 15. Ernie moved through the area for the next twenty four hours, gradually losing intensity as its wind speed decreased from 18 to 13 m/s.

The most striking surface feature produced by the storm during its movement through the area was the strong 'fan shaped' pattern of convergent and divergent currents to the right of the storm track (Figure 7.42). This pattern was produced by the anticyclonically rotating near-inertial currents. Because of the storm's weak intensity,

surface responses in the wake of the storm were minimal. Maximum SST cooling was only 1° C (Figure 7.43) and covered a broad area to the right of the storm track. Sea surface set-down was only 10 to 15 cm (Figure 7.44).

The most significant response was a sea surface set-up along the southern coast of Vietnam produced by divergent upper-ocean storm flow (Figure 7.44). This set up began near 13° N on November 15. It then moved southerly down the coast and increased to 20 cm on November 16 as the storm moved to the southwest and decreased its distance to the coast. By November 17 the set-up along this section of the coast had dissipated as the storm continued tracking into the Gulf of Thailand to the west-southwest and its influence diminished.

Subsurface responses were also weaker due to the low intensity of the storm. Surface layer currents were still highly divergent to the right of the storm track however. A cross section of the currents along 109.6° E (Figure 7.45) on November 16 indicates that the u velocity field was easterly at 60 cm/s north of 11.5° N and westerly at 80 cm/s south of this point. This divergent current produced strong upwelling with vertical velocities in excess of 300 cm/hr near 10° N. Subsurface cooling did not occur in this region on November 16 however.

Along the coast of Vietnam a complete reversal of the normal current pattern occurred. The northeast monsoon flow over the region in November creates a westward intensified current along the coast (Wyrtki, 1961). This pattern is evident in November 4 velocity cross section along 12.3° N (Figure 7.46). Divergent surface currents from the

storm reversed the upper level of this current, generating 140 cm/s northerly currents offshore of the coast to a depth of 25 m. This current reversal is evident down to 160 m offshore, but shoals to just below the surface immediately offshore. Below this northerly layer the flow remains southerly, with a current maximum of 100 cm/s at 75 m (Figure 7.47).

The model fields indicated subsurface cooling over a broad area, from 110° E to 114° E, in a cross section at 12.3° N on November 16 (Figure 7.48). Strong surface divergence caused maximum cooling of 1.5° C to 2° C in this region at 75 m. Along the coast warming of 1° C to 1.5° C occurred down to depths in excess of 200 m (Figure 7.48) due to intense downwelling produced by offshore current flow near 13° N (Figure 7.45). Twenty four hours later these patterns were reversed. Temperatures within a narrow one degree wide wedge of the broad cool anomaly warmed significantly. Temperature increases of up to 2.5° C occurred (Figure 7.49) down to 175 m. Along the coast upwelling caused temperatures to cool by 1° C to 2.5° C. An analysis of the surface current pattern indicates that the forward propagation of the near-inertial surface current generated by the storm caused this reversal of the subsurface temperature anomalies. Near the coast convergence and onshore flow replaced upper-ocean divergence and offshore flow.

D. SENSITIVITY STUDY

The SCS Tropical Cyclone Wind Model provided the major forcing for the POM for this study. This wind model was developed to simulate the wind field produced by Tropical Cyclone Ernie as it moved through the basin. Adjusting the storm profile coefficient, X , tuned the wind model to minimize errors between the simulated wind field and the NSCAT observed and JTWC analyzed wind fields. By adjusting this coefficient the storm size, R_0 , and the slope of the wind profile are varied. This adjustment will then affect both the wind stress curl and divergence fields of the simulated storm. An analysis of the wind field RMS errors, as detailed in Chapter IV of this thesis, indicated that a value of $X = 0.15$ would produce a wind field which was most similar to the actual wind field generated by Ernie.

A model sensitivity test was performed however to determine how sensitive the POM was to minor variations in the Tropical Cyclone Wind Model. Three additional POM experimental runs were done using wind fields produced with $X = 0.26, 0.35$ and 0.45 . To examine the POM sensitivity an analysis of the temperature anomaly at $z = -50$ m, roughly the base of the mixed layer, was done. This parameter was chosen since it is the one parameter that is dependent not only on the magnitude of the wind, but also the divergence and curl of the wind field. An RMS difference time series, between the main and sensitivity experimental runs, was constructed in each of the three analysis areas (Figure 7.50). An examination of these time series indicates that the POM is insensitive

to minor variations in the wind fields. Maximum differences were only 0.15° C, or approximately 4% of the observed maximum model temperature anomaly at $z = -50$ m. These maximum differences occurred in analysis areas One and Three, as the storm moved along the coasts of Luzon and Vietnam, respectively. Differences in analysis area Two, where the storm was quasi-stationary, were only 20% of the differences in the areas One and Three.

This sensitivity study suggests that to simulate the ocean responses to forcing caused by a moving tropical cyclone realistically it is critical to simulate accurately both the size and intensity of the tropical cyclone's wind field. Any errors in these storm parameters will affect both the wind stress curl and divergence, which will in turn affect the ocean responses.

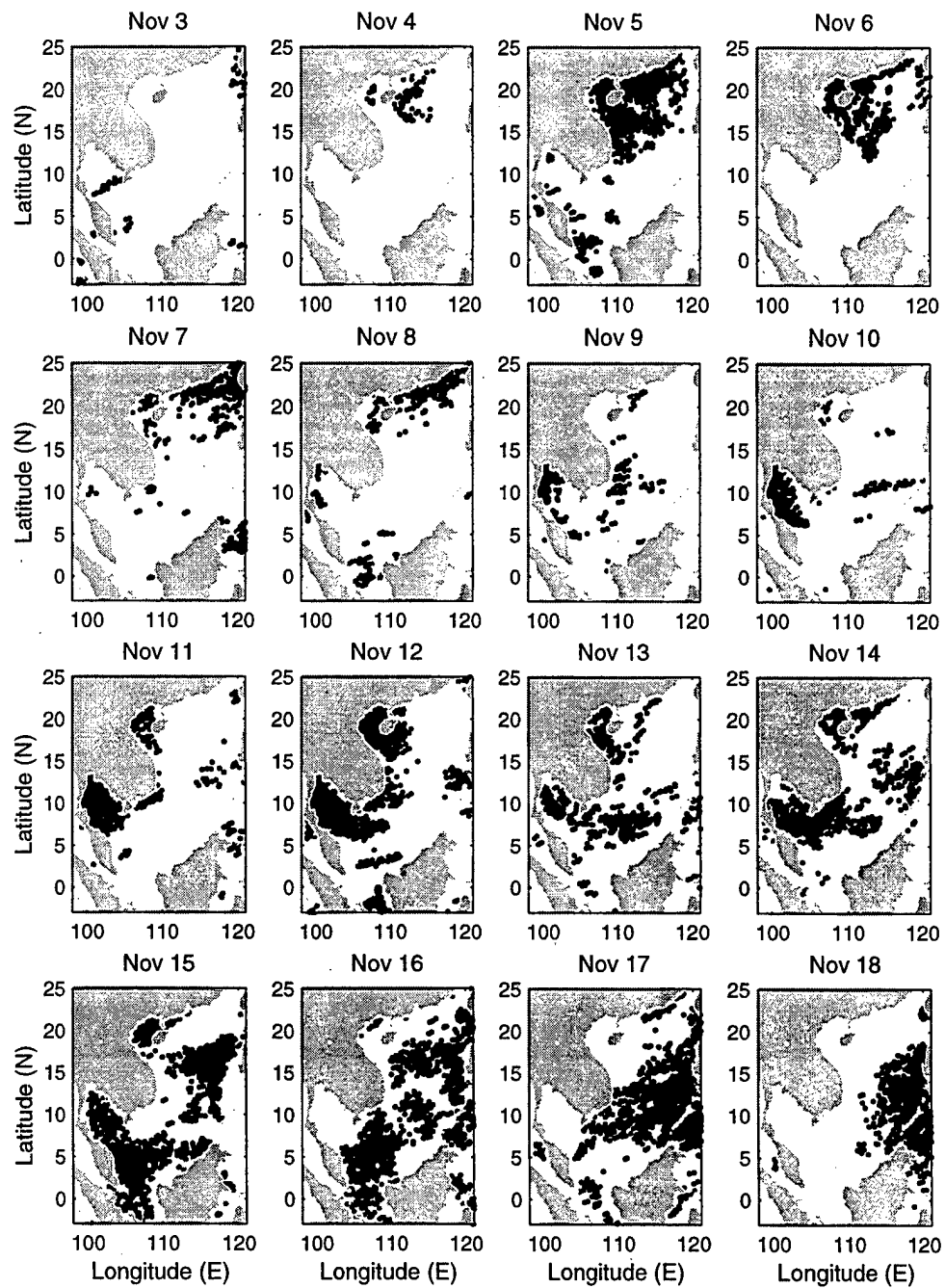


Figure 7.1. Satellite MCSST coverage for November 3 to 18, 1996. Dark areas indicate those locations where MCSST observations were retrieved.

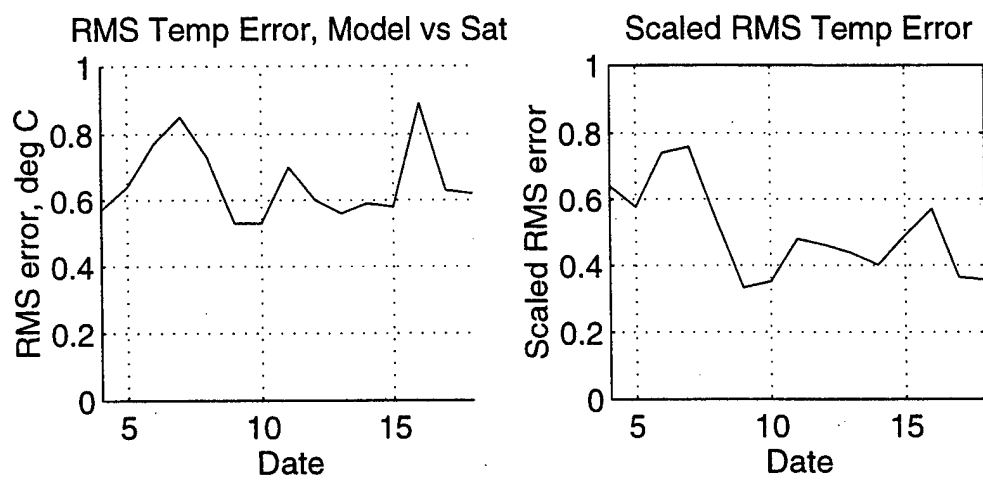


Figure 7.2. (a) Time series of the SST RMS errors ($^{\circ}\text{C}$). Errors calculated between the POM simulated SST and the observed satellite MCSST. (b) Time series of the scaled SST RMS errors ($^{\circ}\text{C}$). Scaling was performed by dividing the standard deviation of the observed satellite MCSST by the SST RMS error.

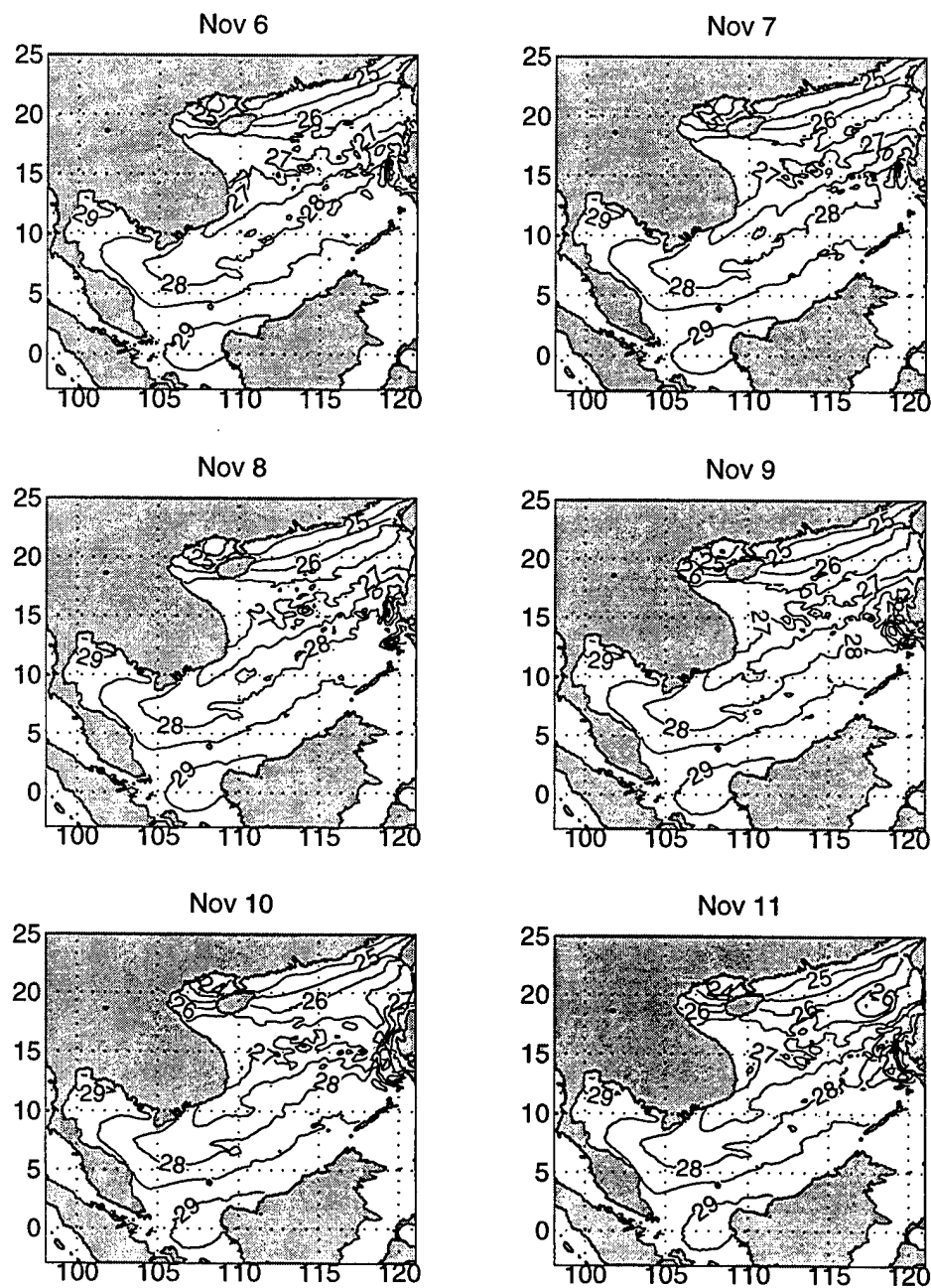


Figure 7.3. POM simulated sea surface temperature ($^{\circ}\text{C}$) for November 6 to 11, 1996.

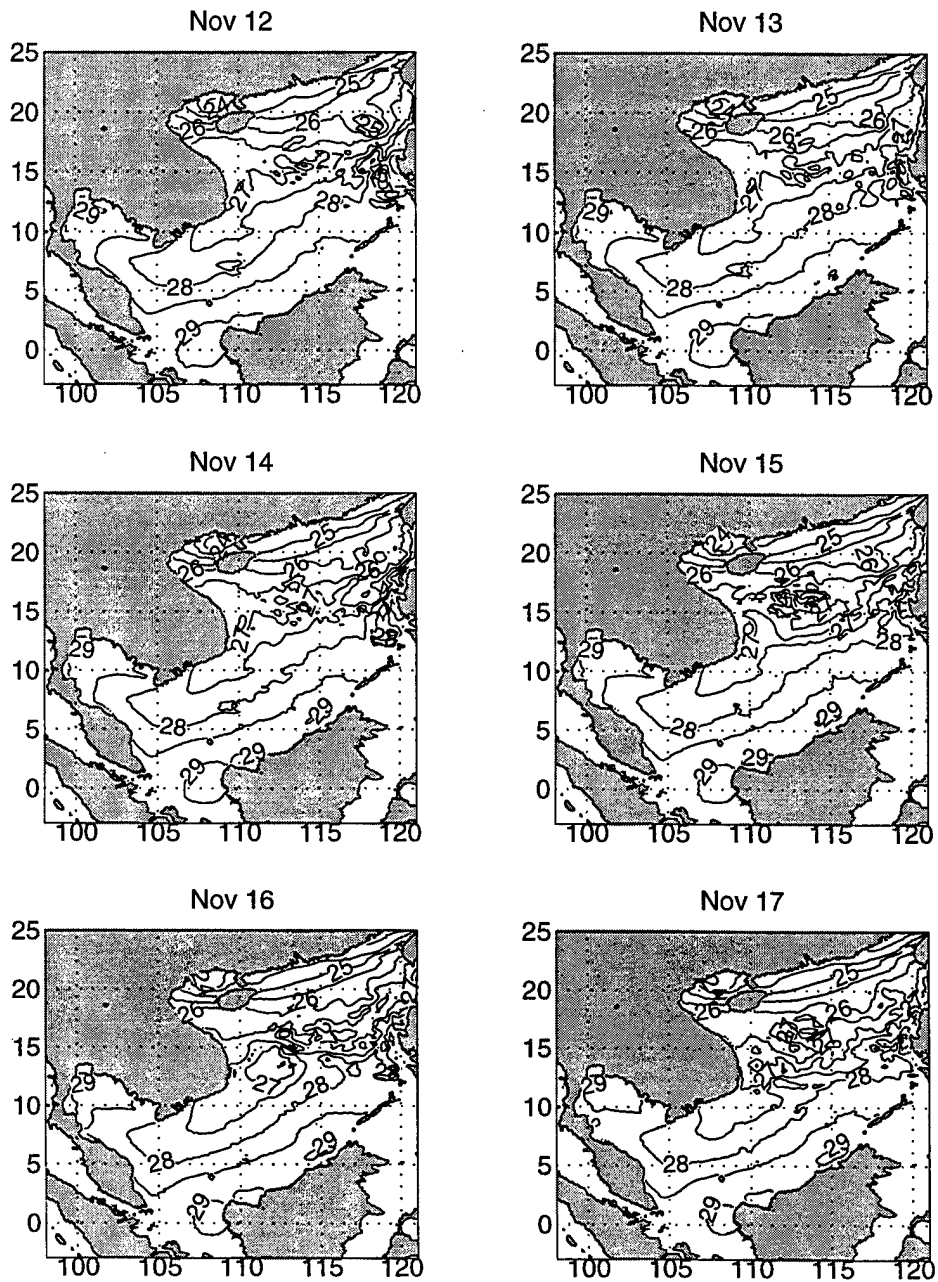


Figure 7.4. POM simulated sea surface temperature ($^{\circ}\text{C}$) for November 12 to 17, 1996.

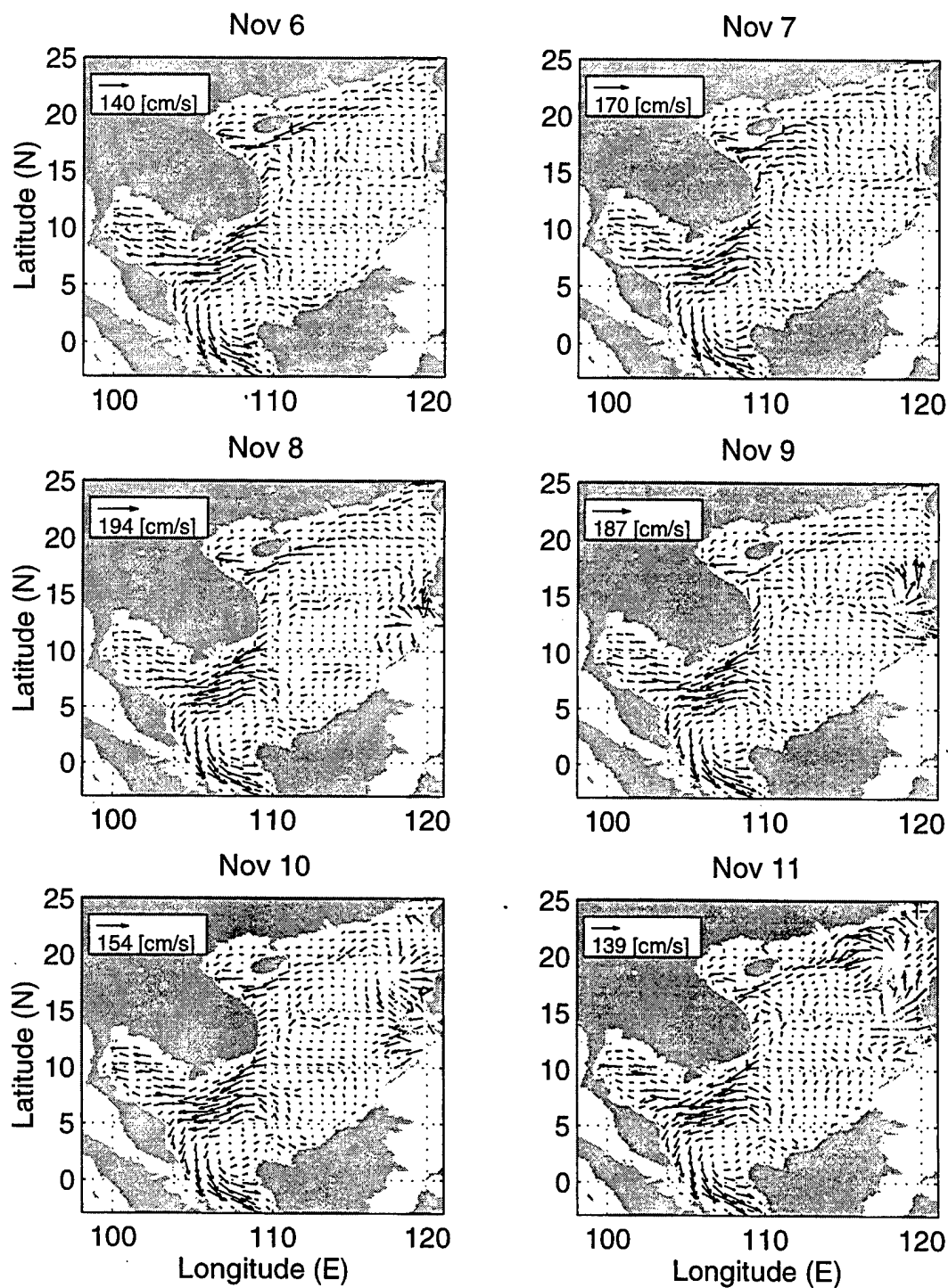


Figure 7.5. POM simulated surface currents (m/s) for November 6 to 11, 1996.

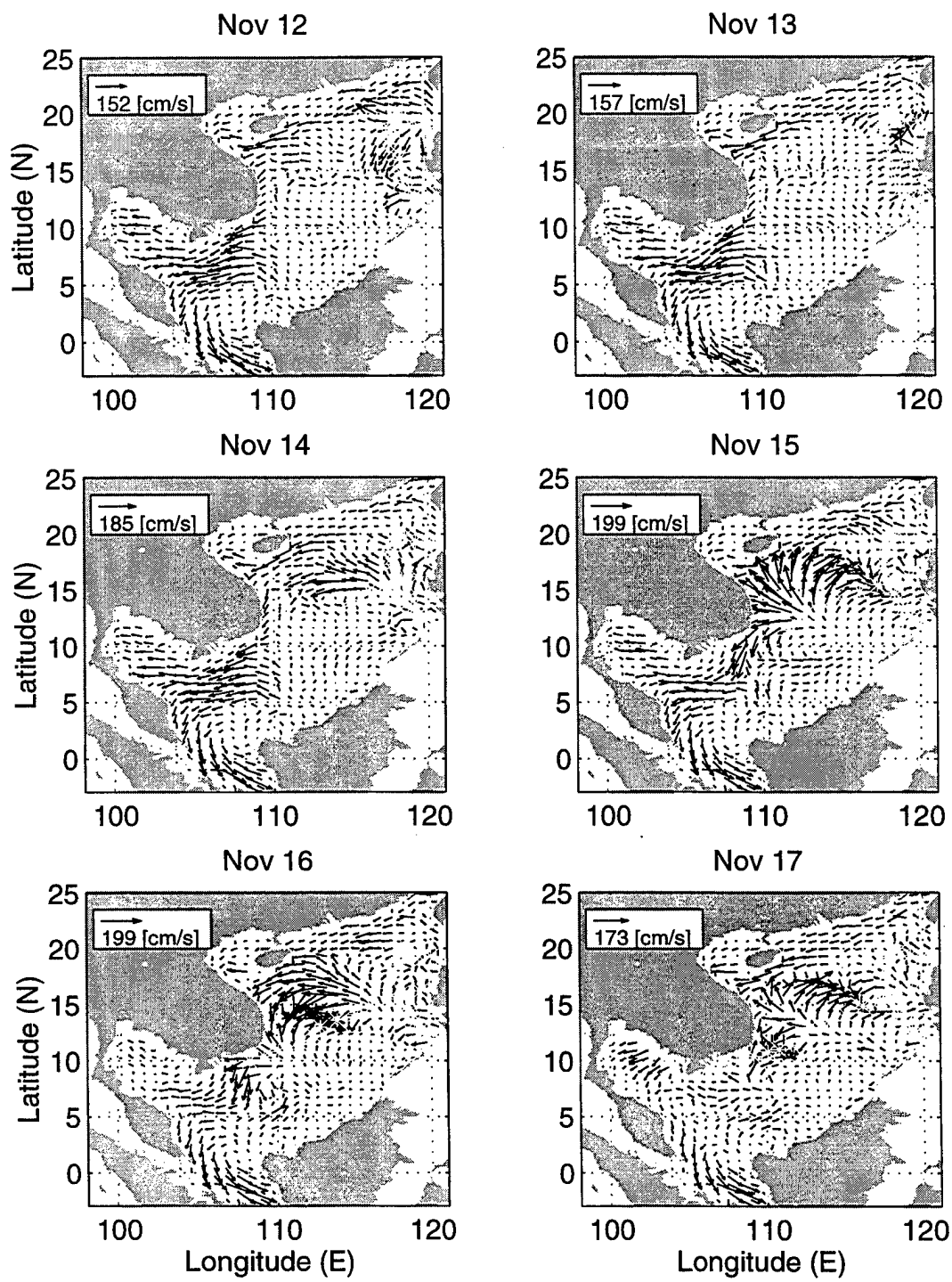


Figure 7.6. POM simulated surface currents (m/s) for November 12 to 17, 1996.

Analysis Areas

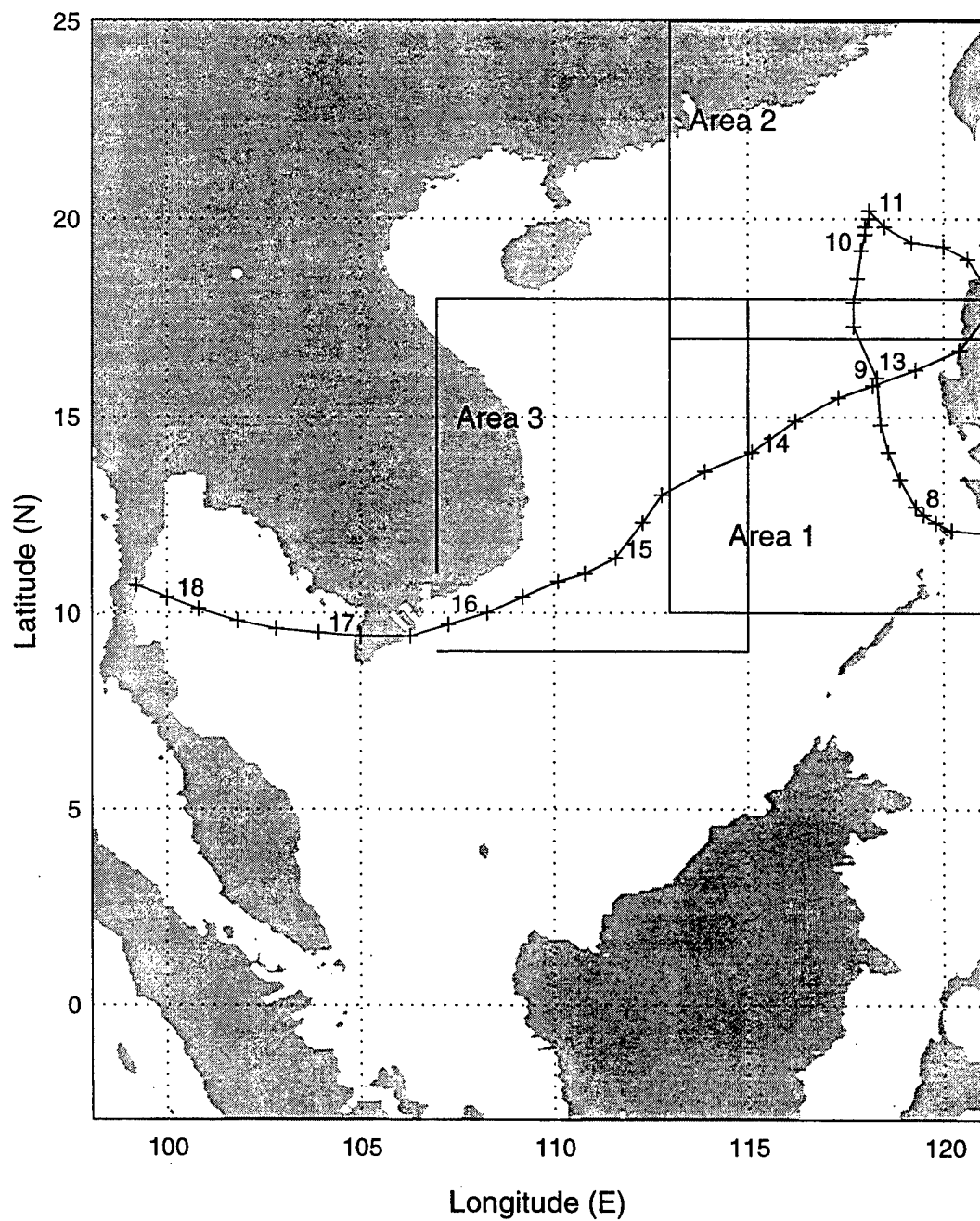


Figure 7.7. POM simulation analysis areas.

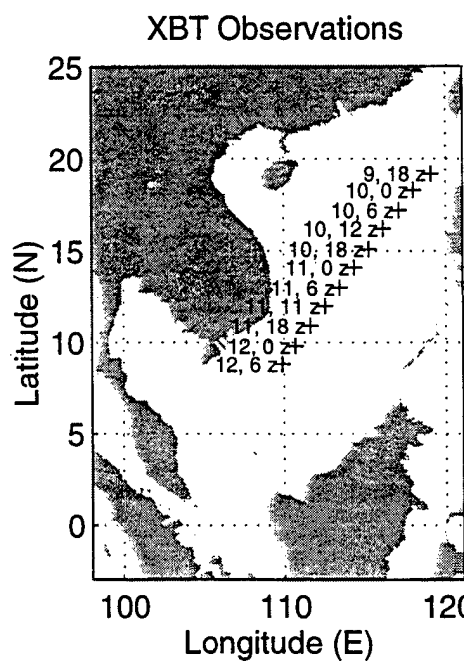


Figure 7.8. XBT observation locations.

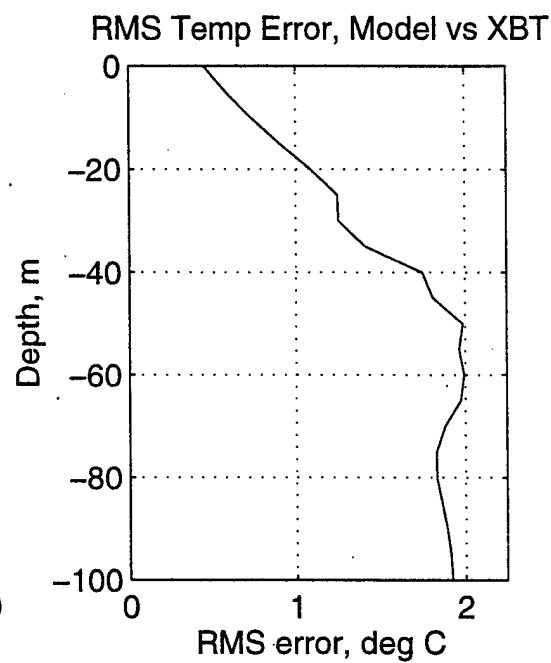


Figure 7.9. Average RMS temperature error ($^{\circ}\text{C}$). Average RMS error calculated between the POM simulated temperature fields and eleven XBT observations.

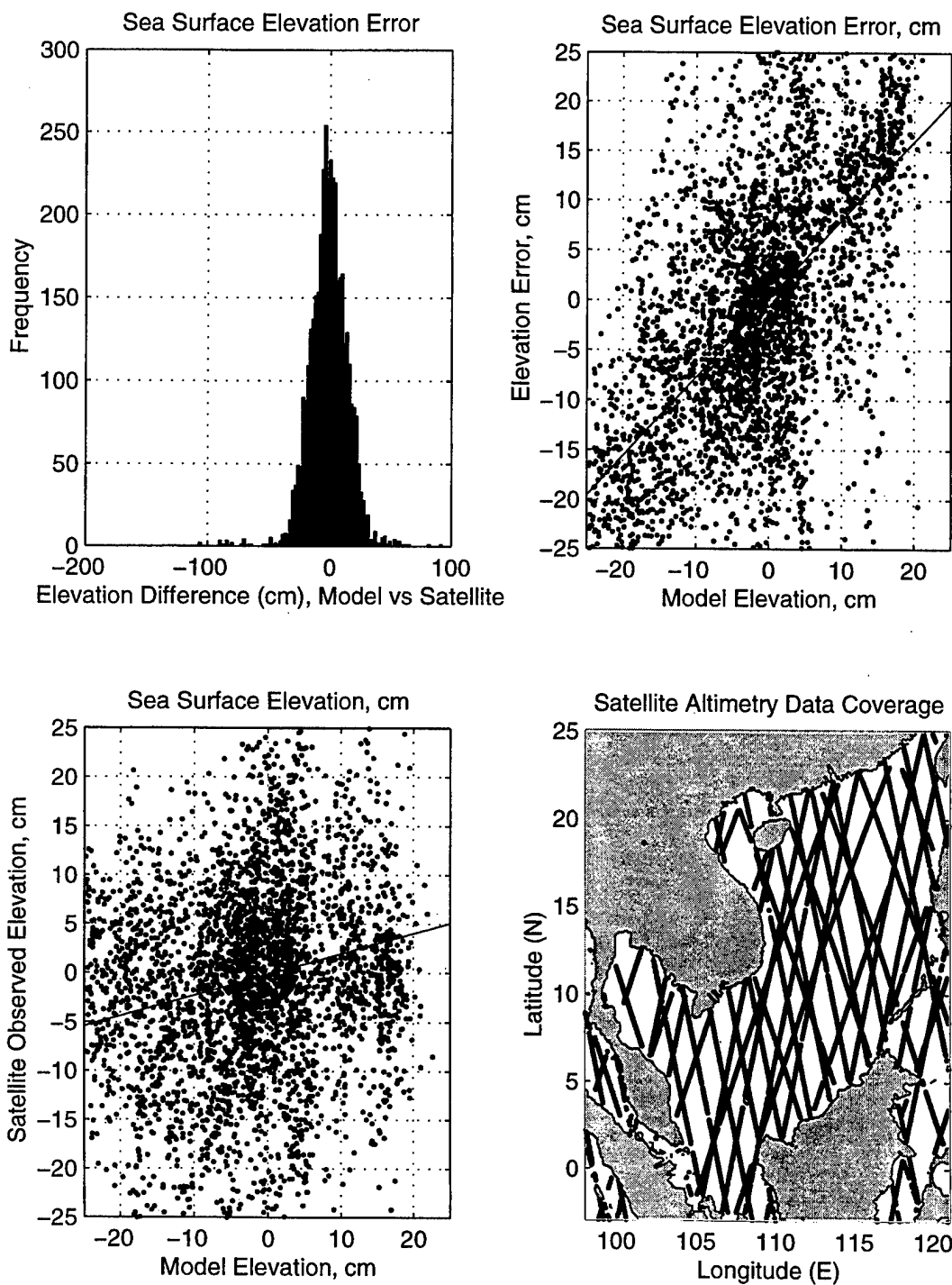


Figure 7.10. (a) 14 day average POM sea surface elevation error (cm). (b) Scatter plot of POM sea surface elevation and the elevation error (cm). (c) Scatter plot of satellite and POM sea surface elevations (cm). (d) 14 day TOPEX/Poseidon and ERS1 observation coverage.

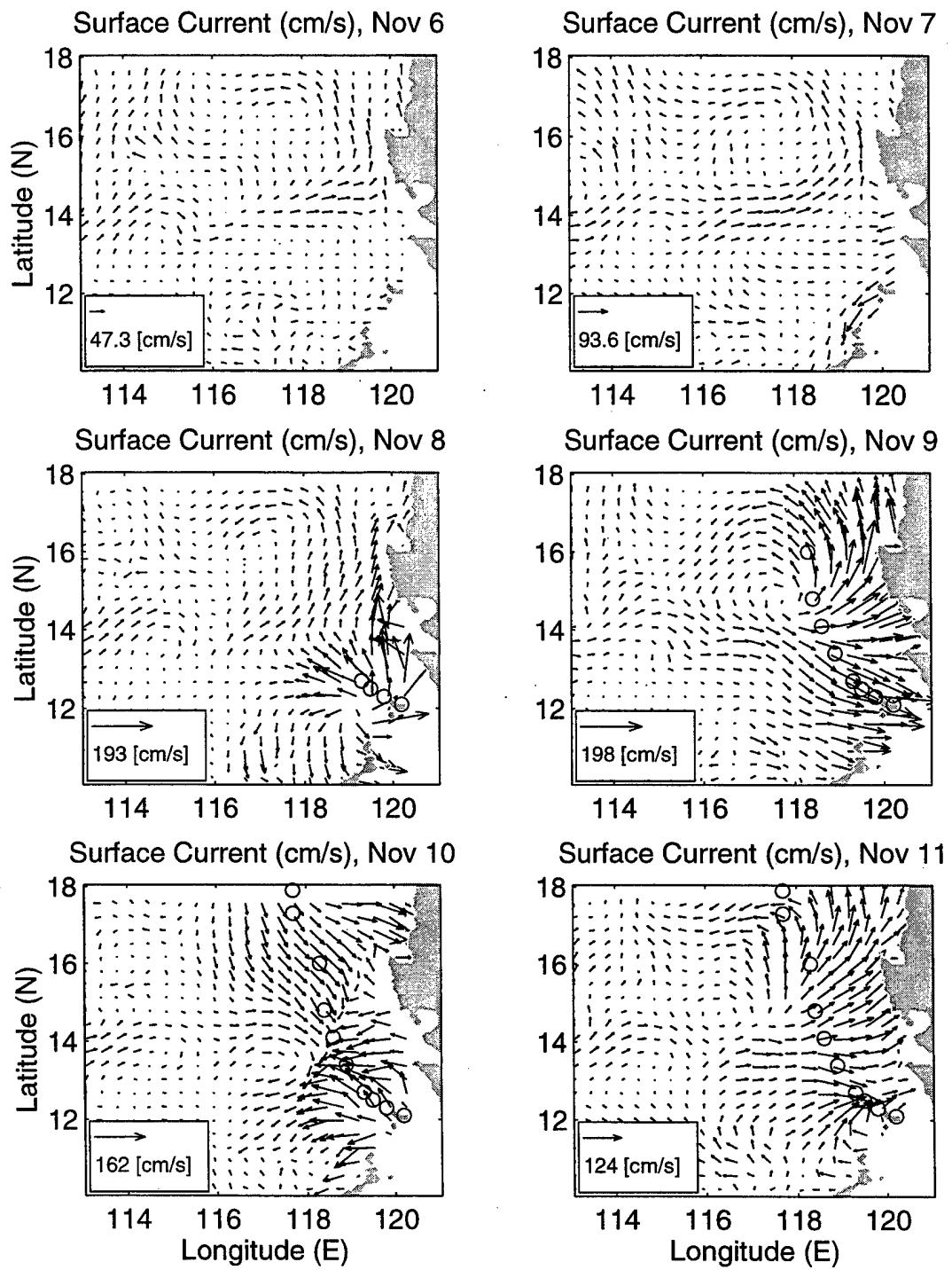


Figure 7.11. Surface current (cm/s) for Analysis Area One, November 6 to 11, 1996.

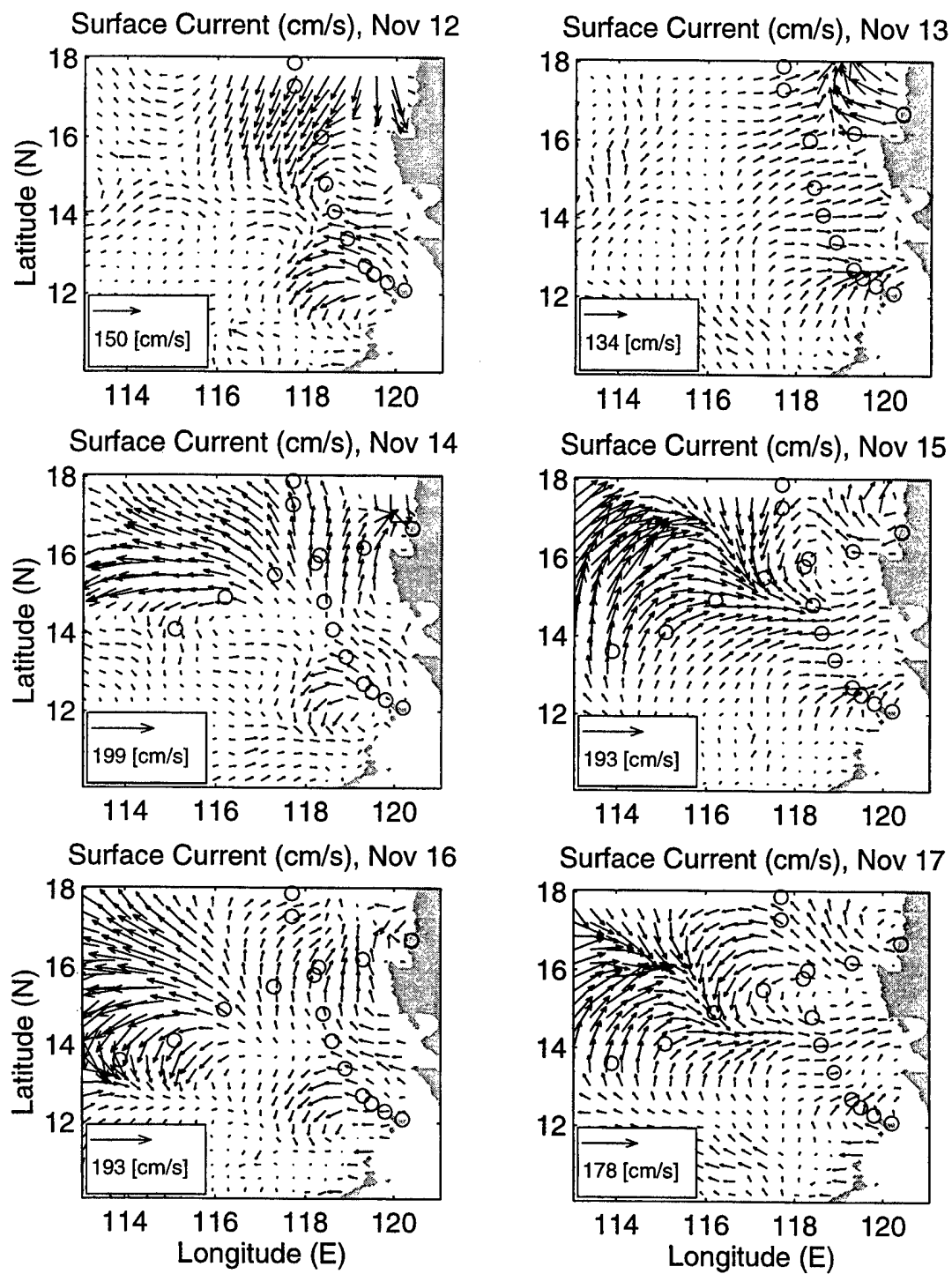


Figure 7.12. Surface current (cm/s) for Analysis Area One, November 12 to 17, 1996.

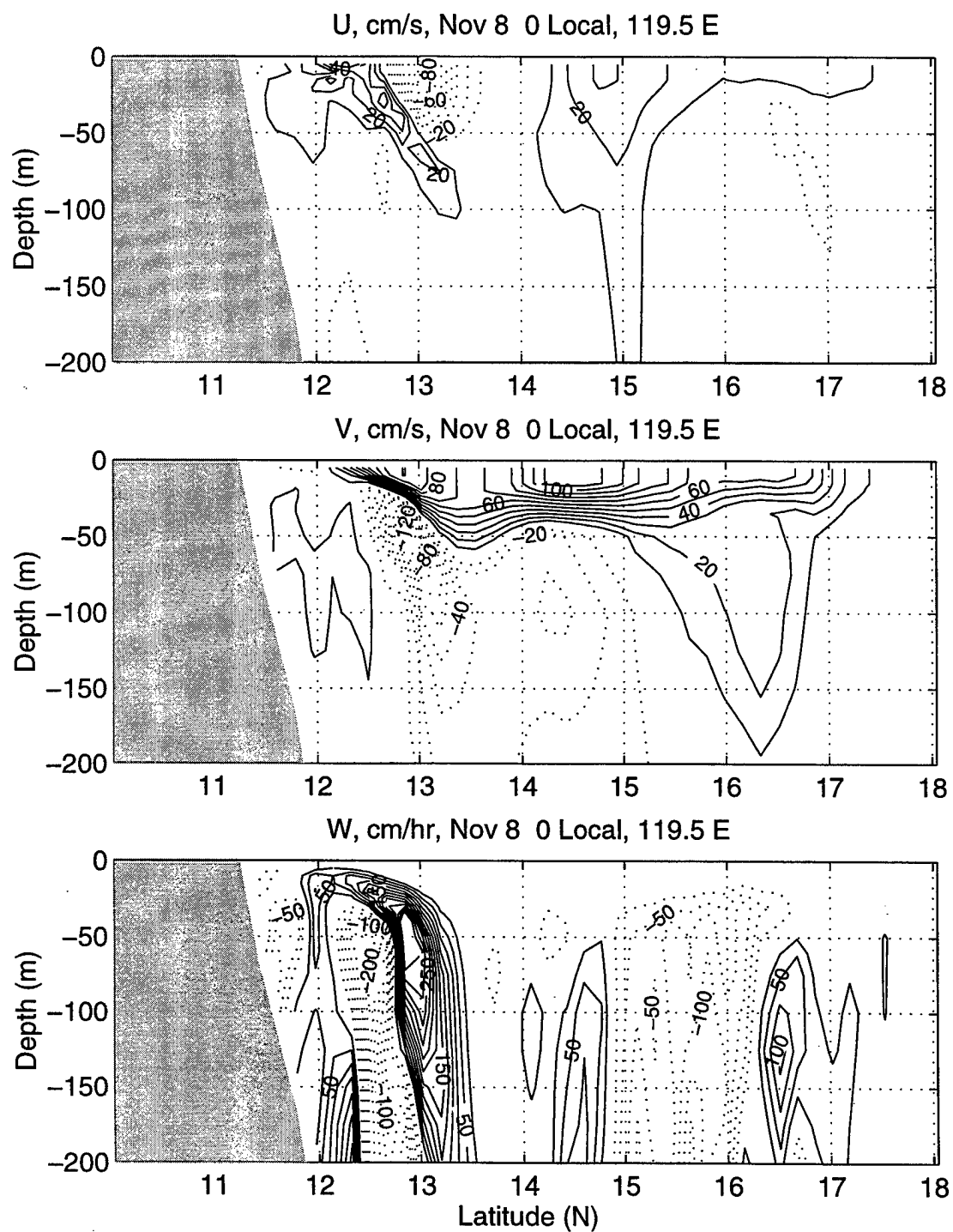


Figure 7.13. Analysis Area One longitudinal cross section of model u , v (cm/s) and w (cm/hr) velocities along 119.5° E for November 8, 1996.

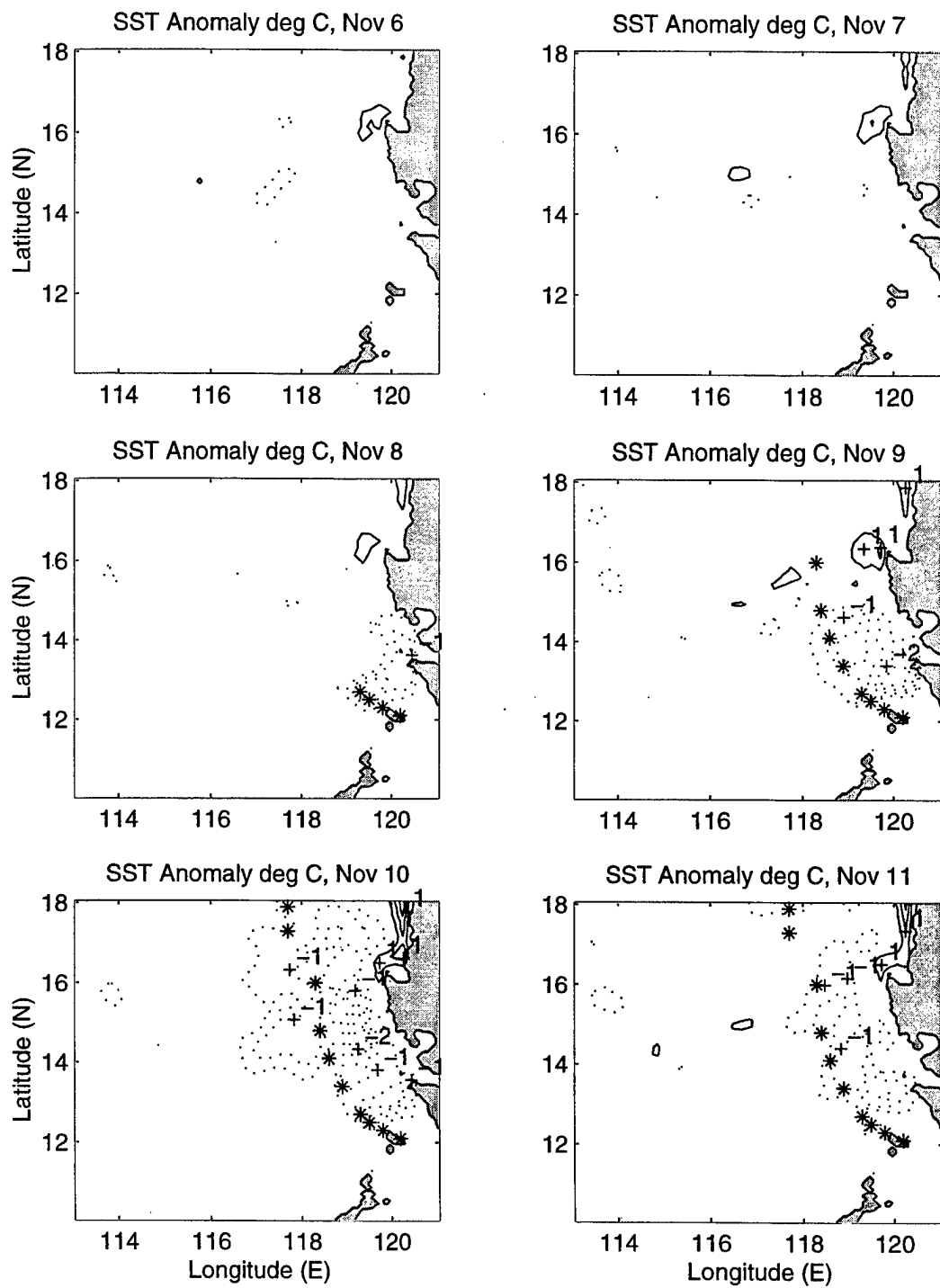


Figure 7.14. Sea surface temperature anomaly ($^{\circ}\text{C}$) for Analysis Area One, November 6 to 11, 1996. Temperature changes relative to November 4 SST model field.

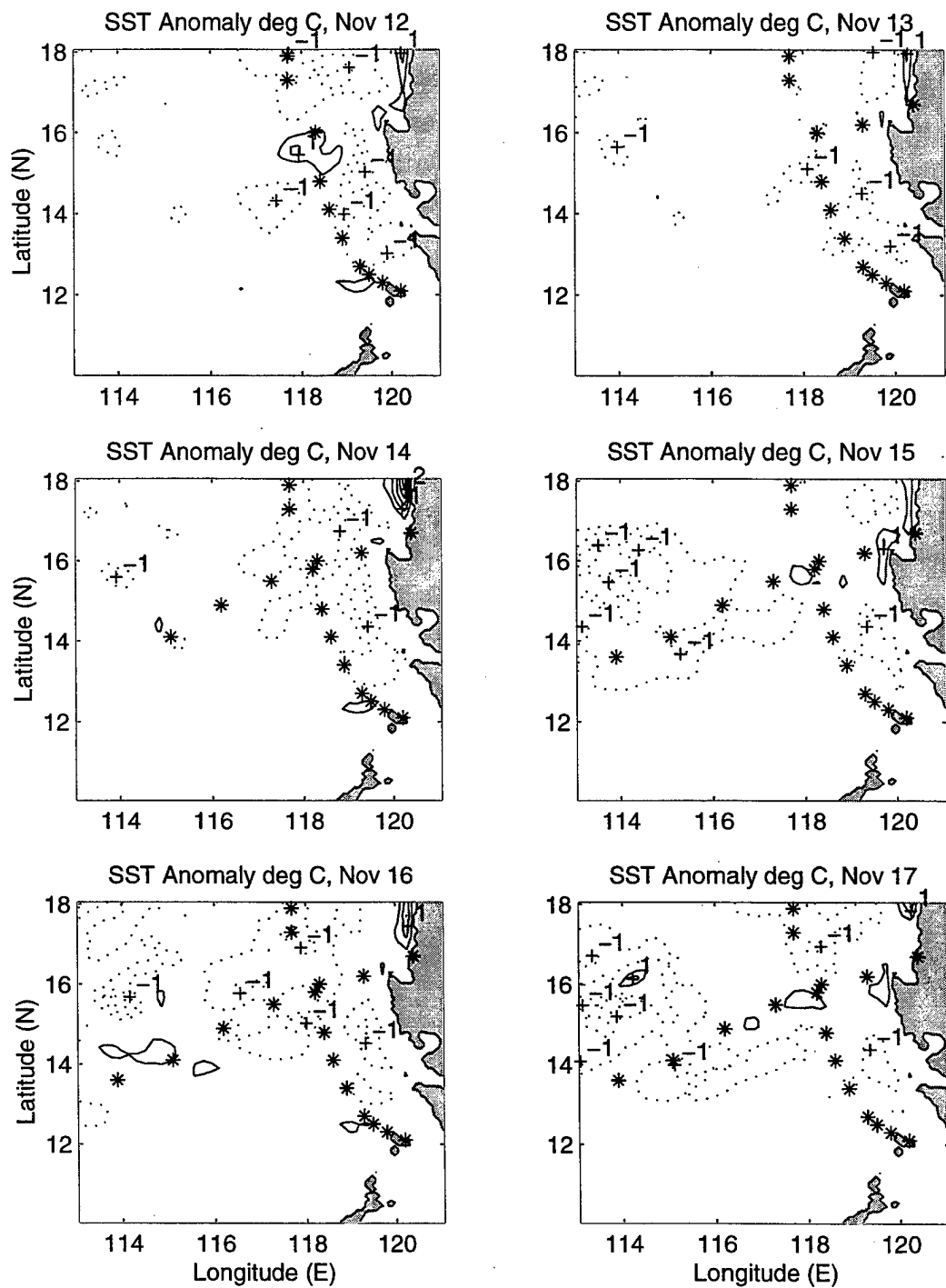


Figure 7.15. Sea surface temperature anomaly ($^{\circ}\text{C}$) for Analysis Area One, November 12 to 17, 1996. Temperature changes relative to November 4 SST model field.

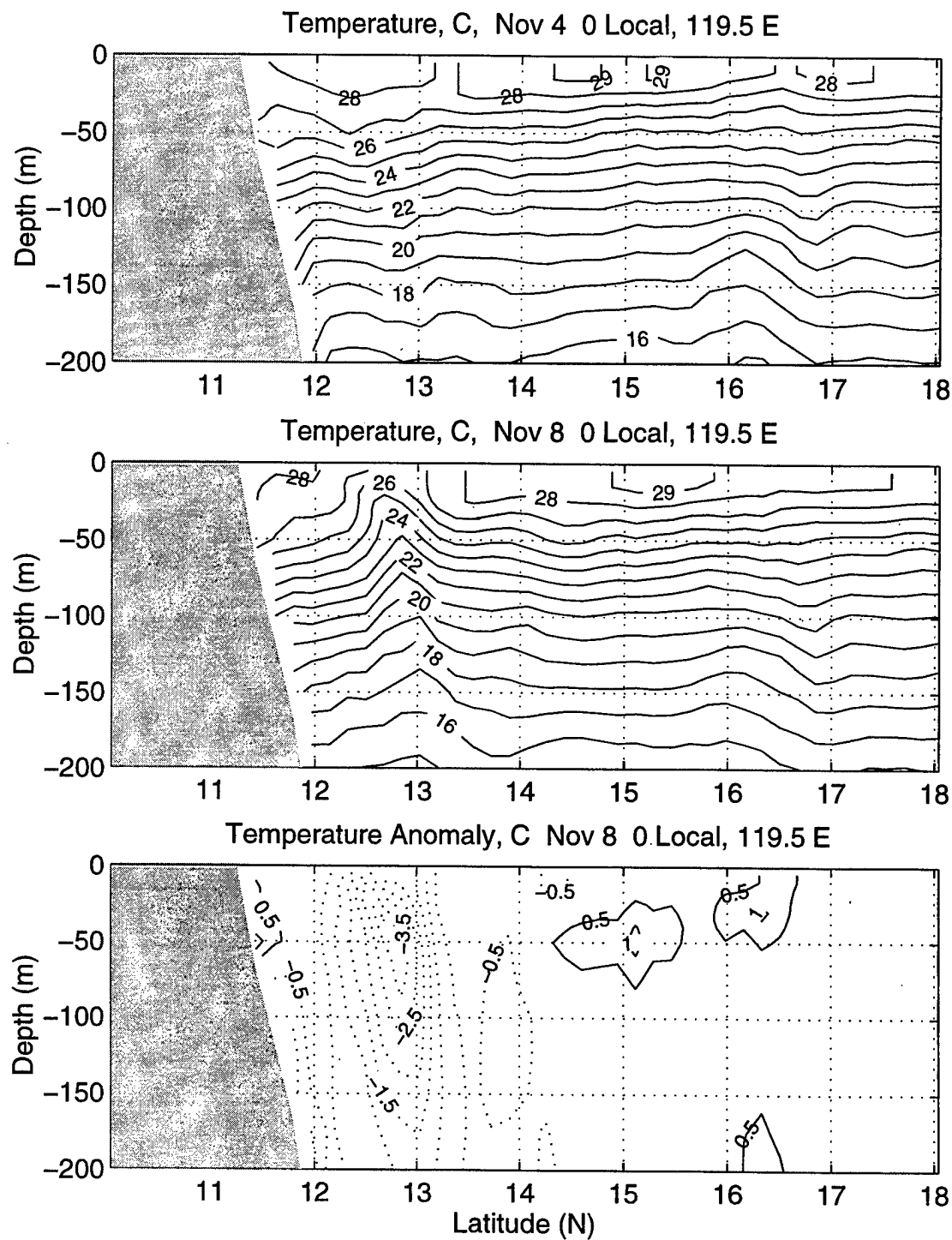


Figure 7.16. Analysis Area One longitudinal cross section of the temperature anomaly ($^{\circ}\text{C}$) along 119.5°E for November 8, 1996. Anomaly relative to November 4 temperature model fields.

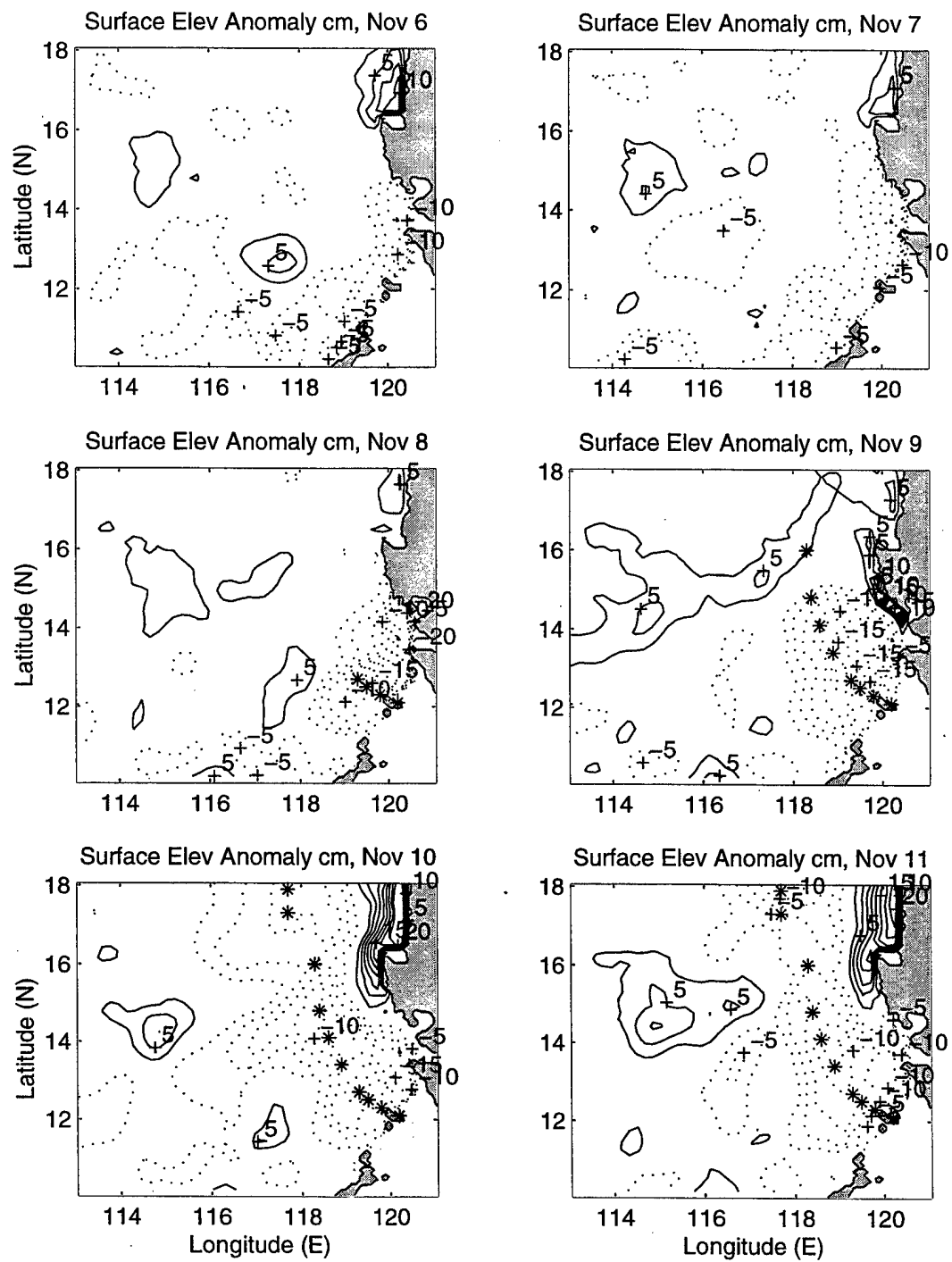


Figure 7.17. Sea surface elevation anomaly (cm) for Analysis Area One, November 6 to 11. Elevation changes relative to November 4 sea surface elevation model field.

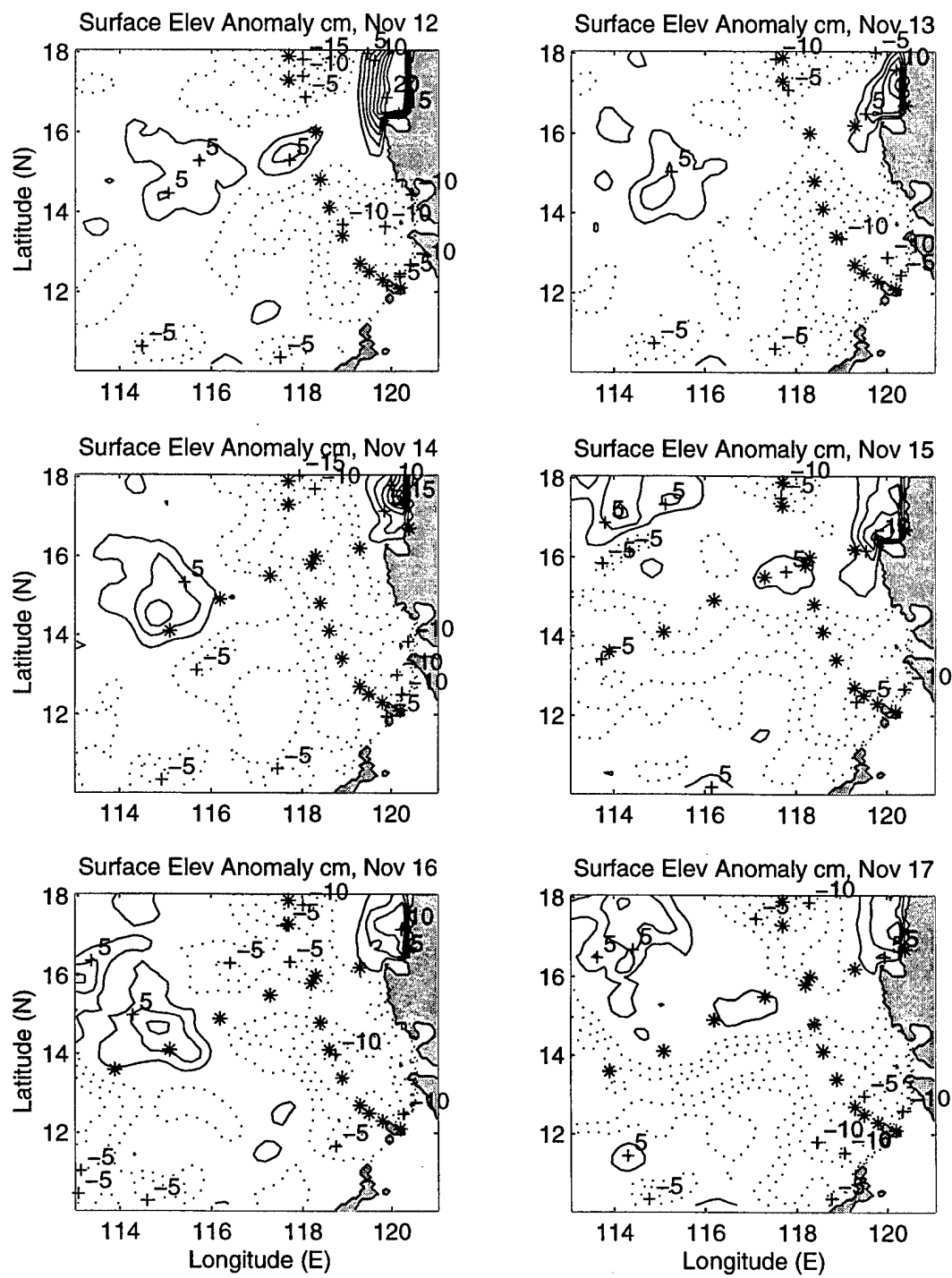


Figure 7.18. Sea surface elevation anomaly (cm) for Analysis Area One, November 12 to 17. Elevation changes relative to November 4 sea surface elevation model field.

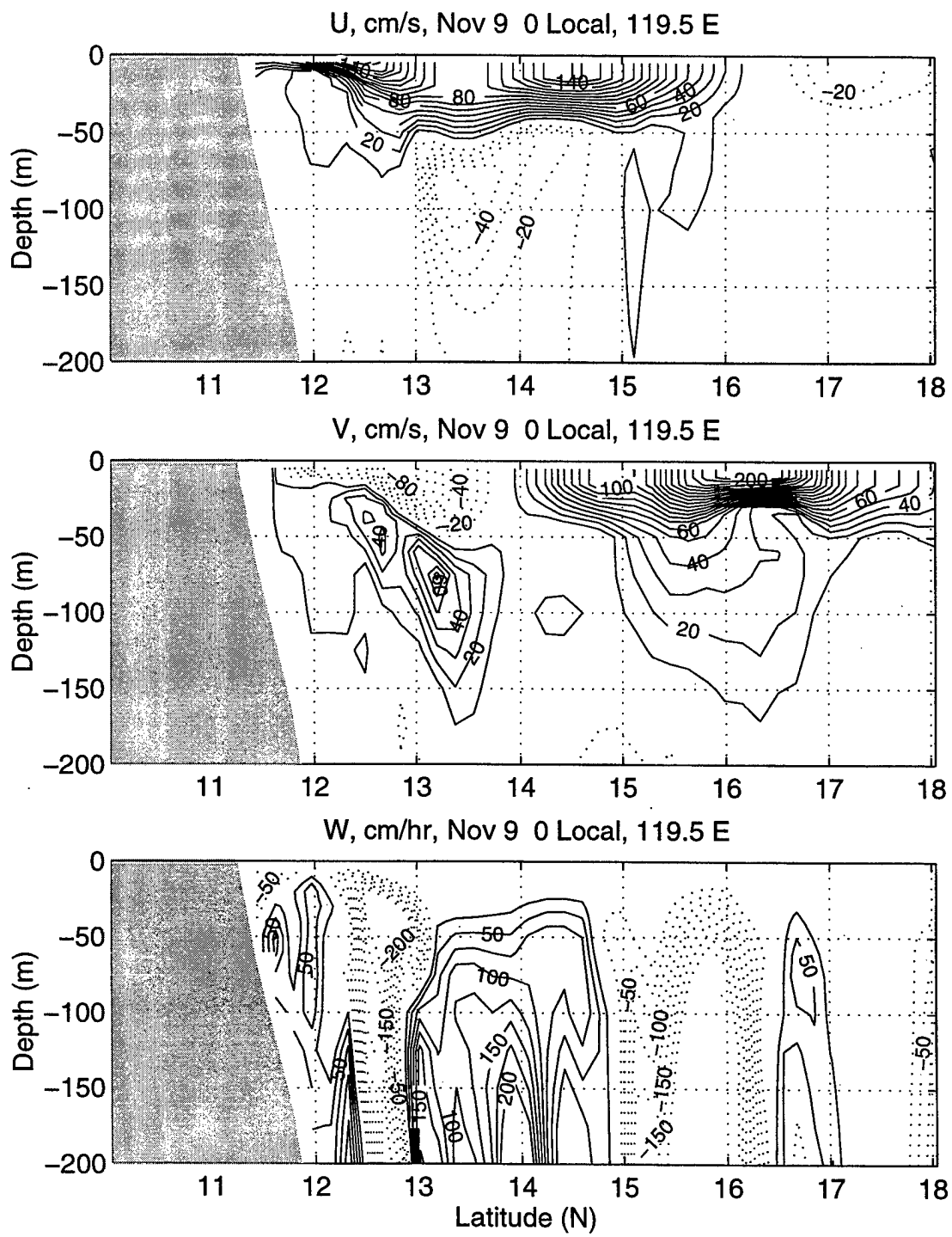


Figure 7.19. Analysis Area One longitudinal cross section of model u, v (cm/s) and w (cm/hr) velocities along 119.5° E for November 9, 1996.

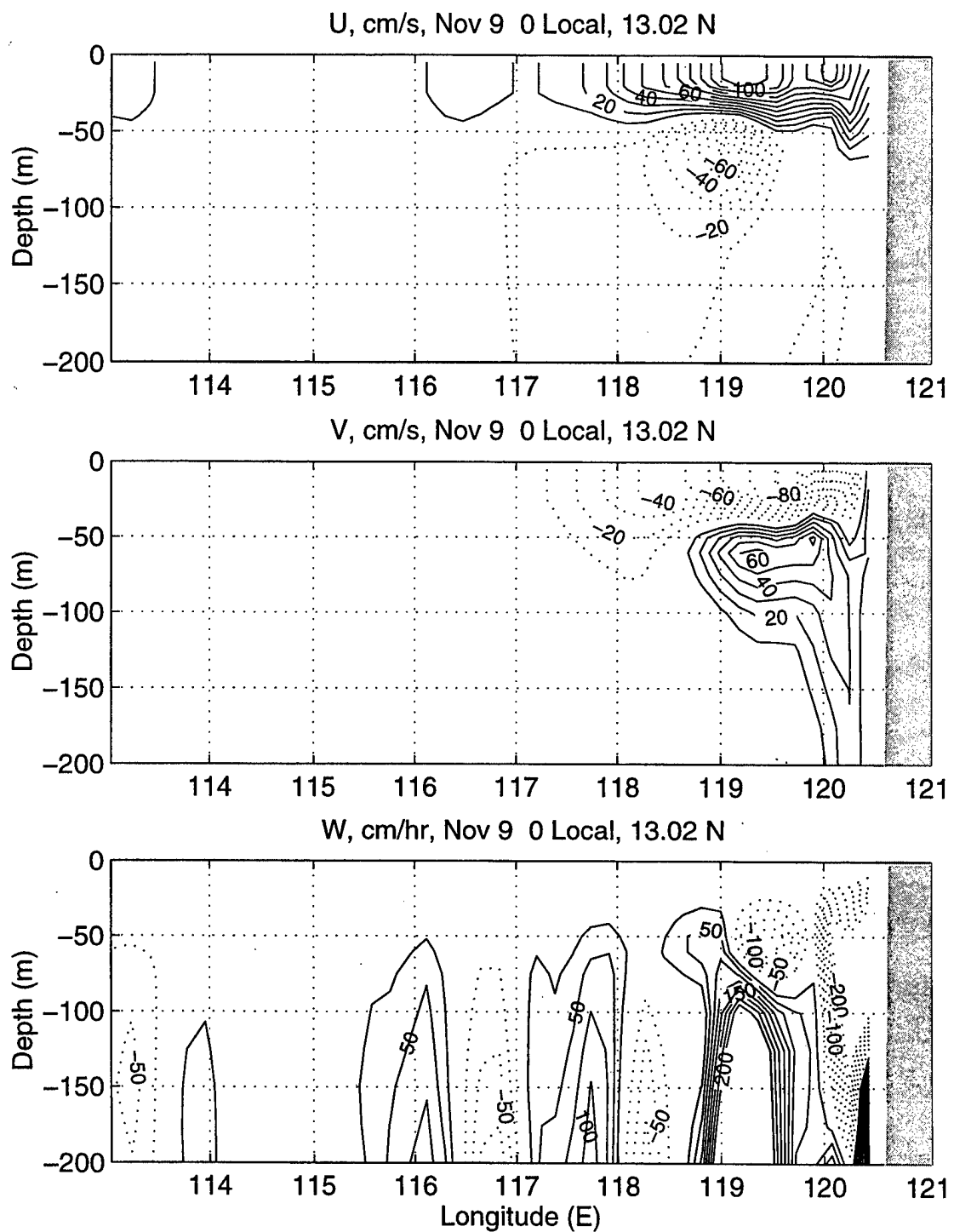


Figure 7.20. Analysis Area One latitudinal cross section of model u , v (cm/s) and w (cm/hr) velocities along 13° N for November 9, 1996.

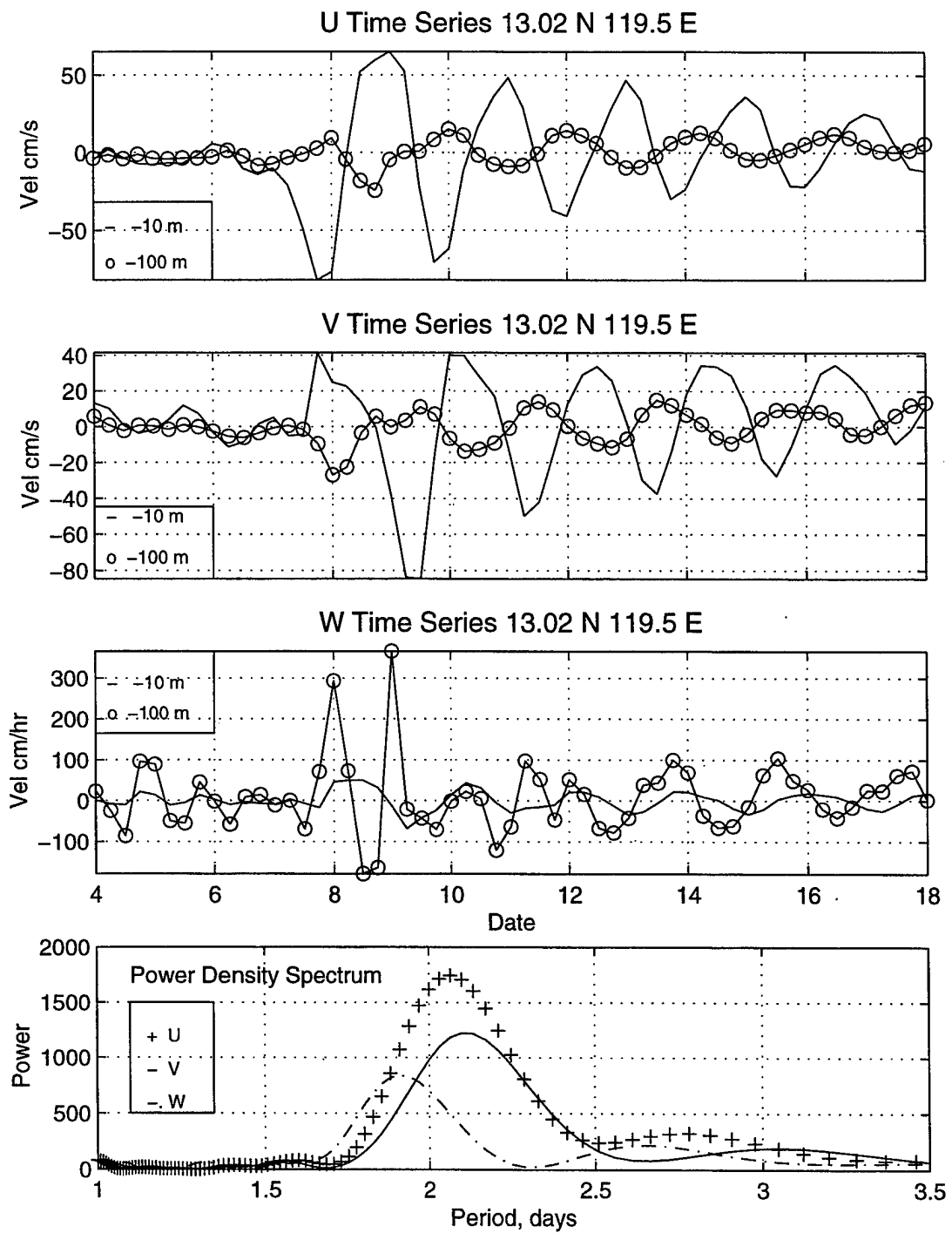


Figure 7.21. Time series and power density spectrum of model u , v and w velocities at 13° N, 119.5° E, from November 4 to 18.

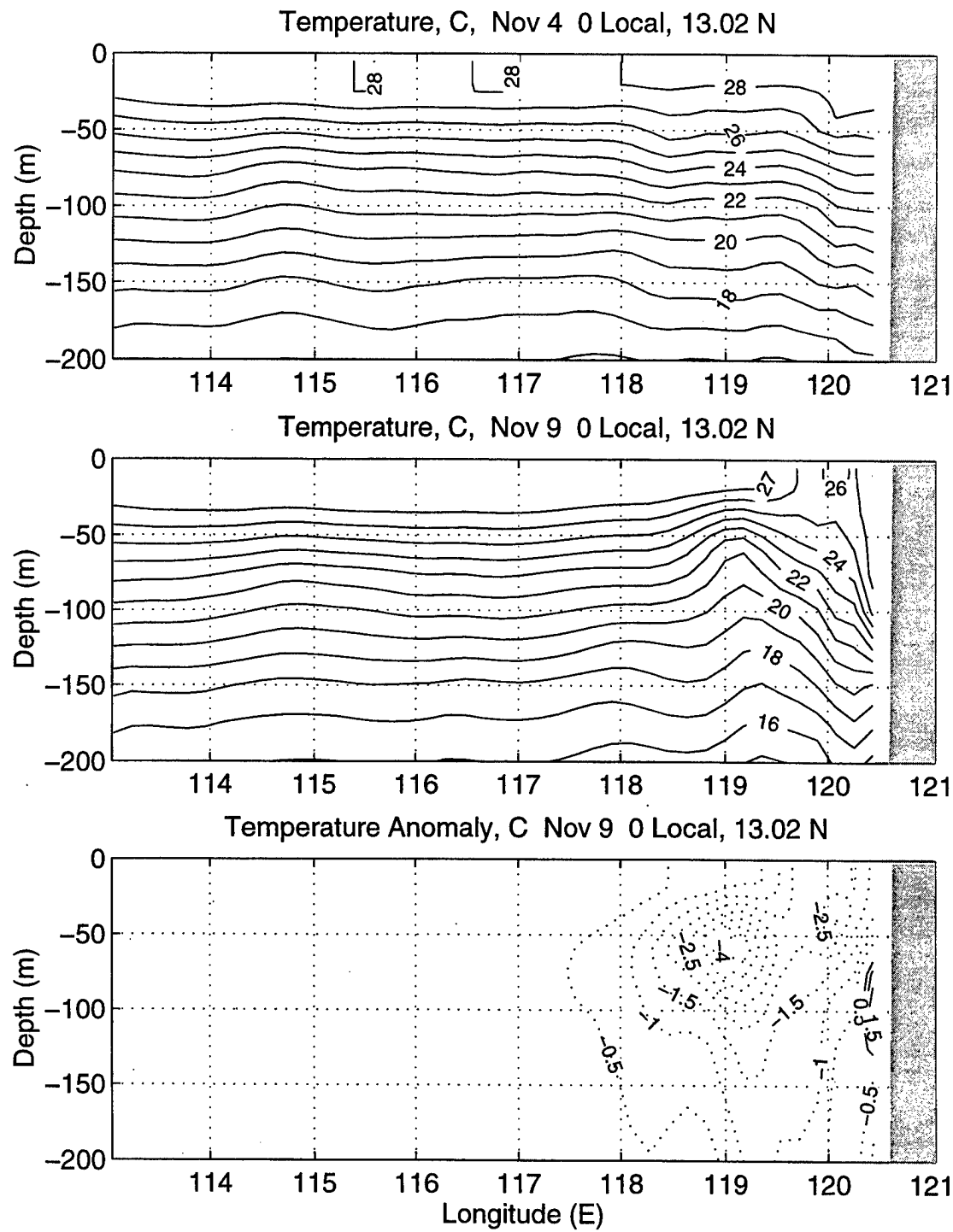


Figure 7.22. Analysis Area One latitudinal cross section of the temperature anomaly ($^{\circ}\text{C}$) along 13° N for November 9, 1996. Anomaly relative to November 4 temperature model fields.

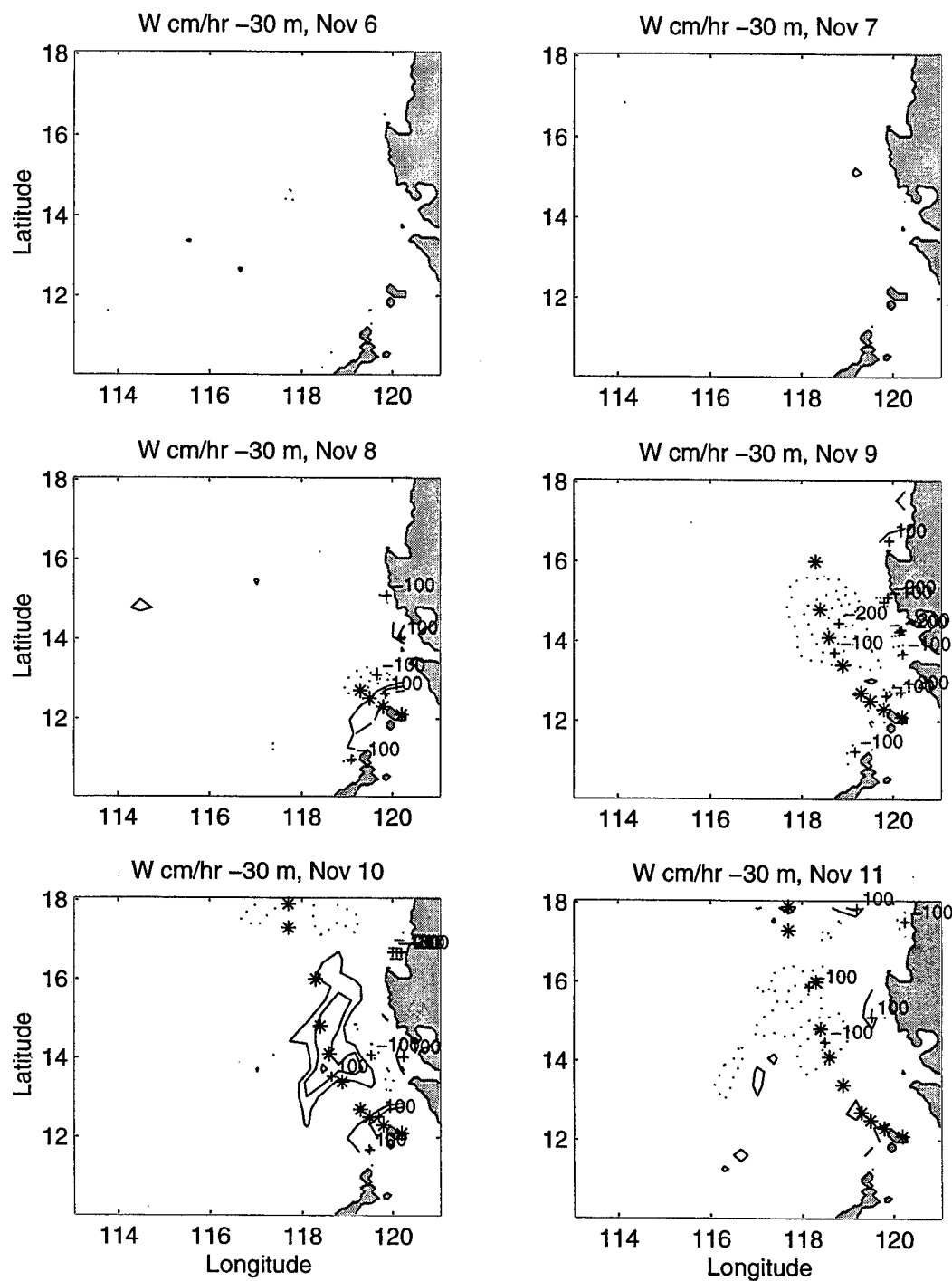


Figure 7.23. POM simulated vertical velocity (cm/hr) at $z = -30$ m for November 6 to 11, 1996. Positive values indicate upward vertical motion.

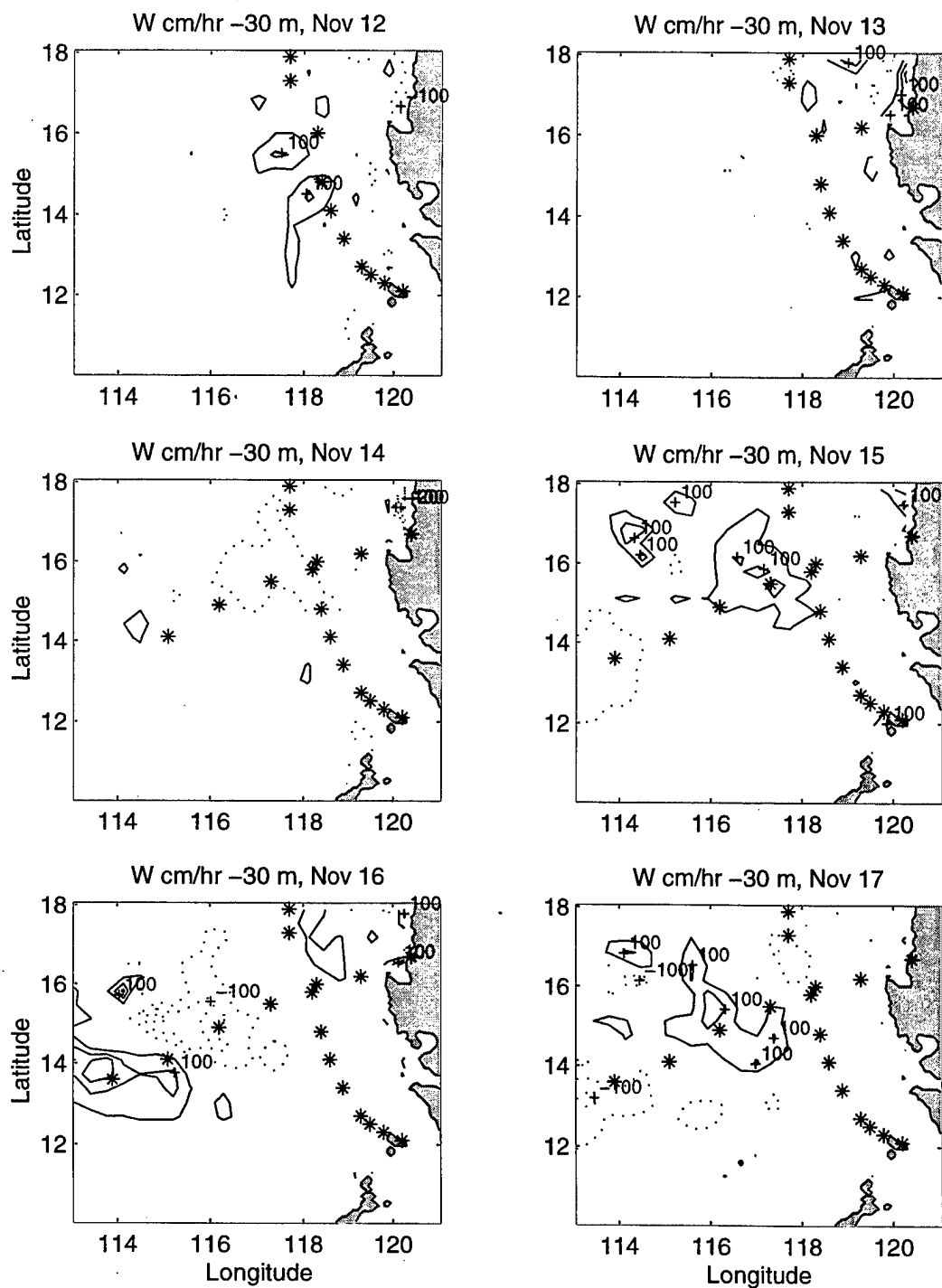


Figure 7.24. POM simulated vertical velocity (cm/hr) at $z = -30$ m for November 12 to 17, 1996. Positive values indicate upward vertical motion.

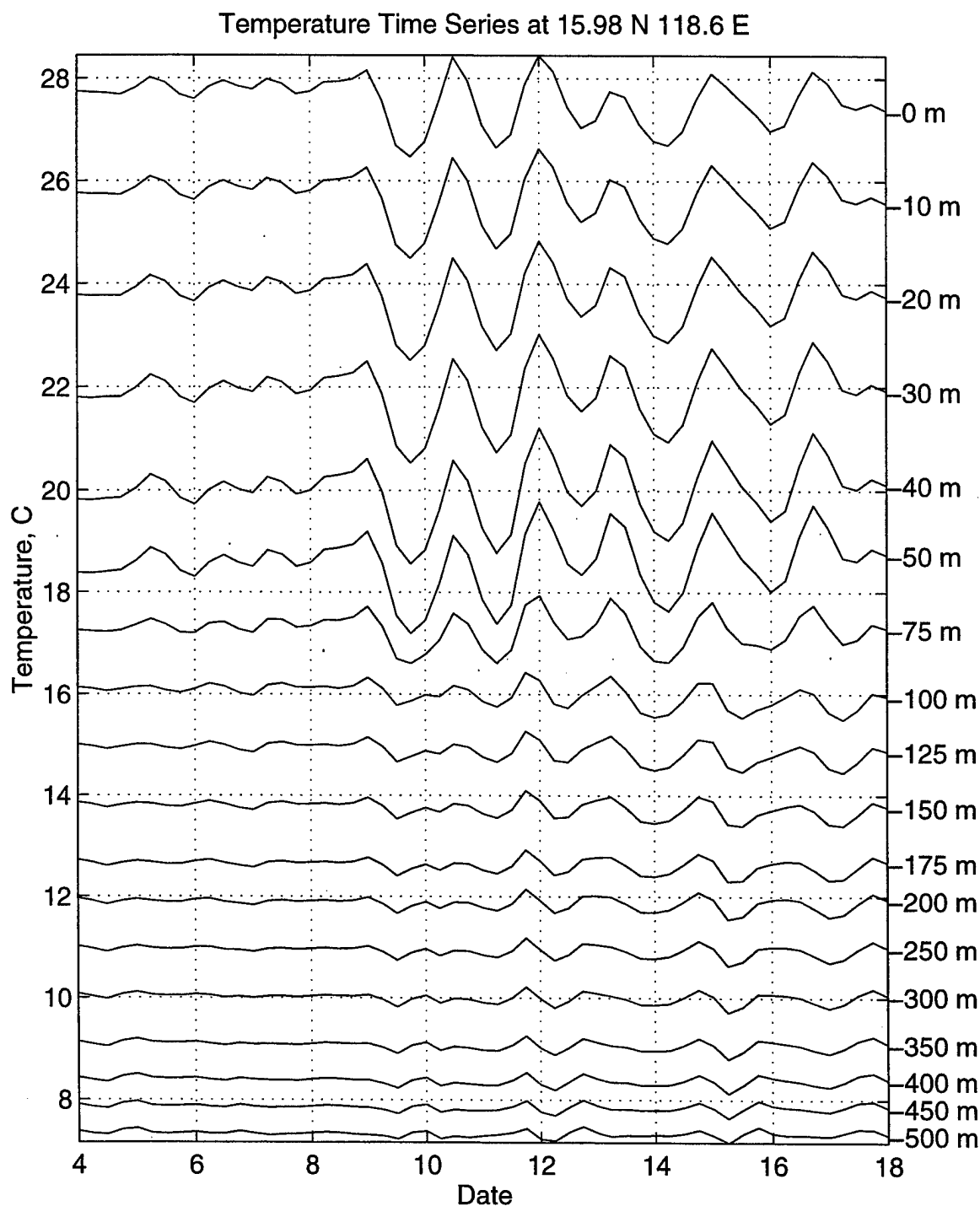


Figure 7.25. Time series of model sub-surface temperature ($^{\circ}\text{C}$) at 16°N , 118.6°E , from November 4 to 18.

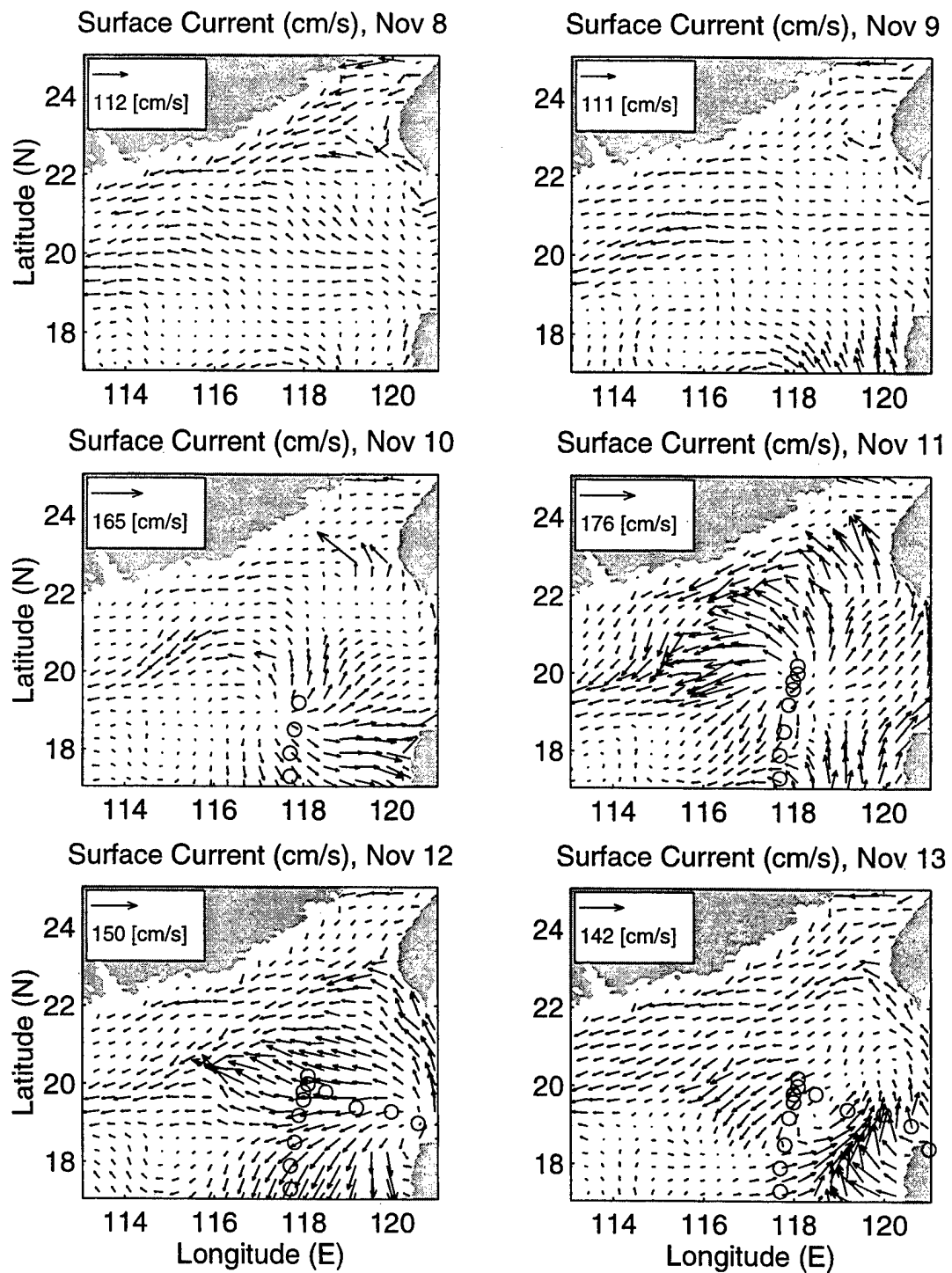


Figure 7.26. Surface current (cm/s) for Analysis Area Two, November 8 to 13, 1996.

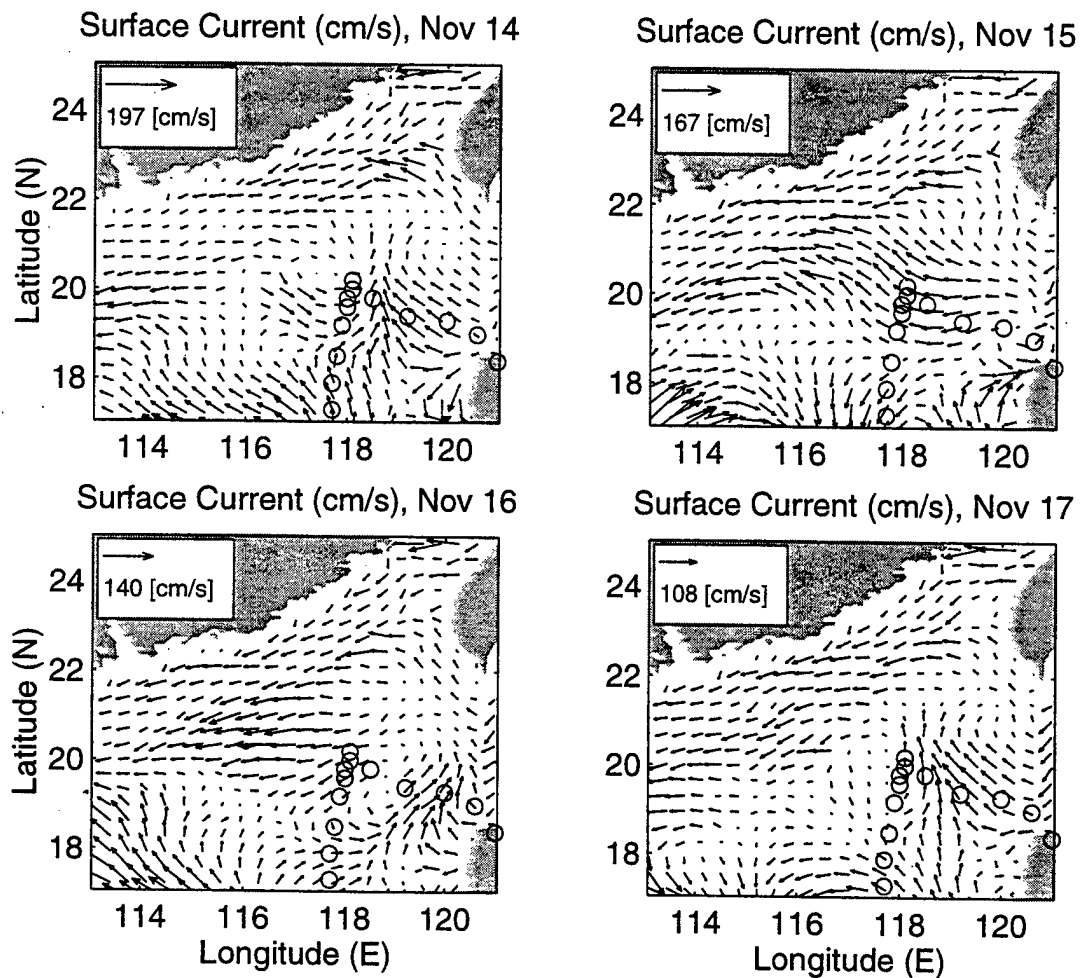


Figure 7.27. Surface current (cm/s) for Analysis Area Two, November 14 to 17, 1996.

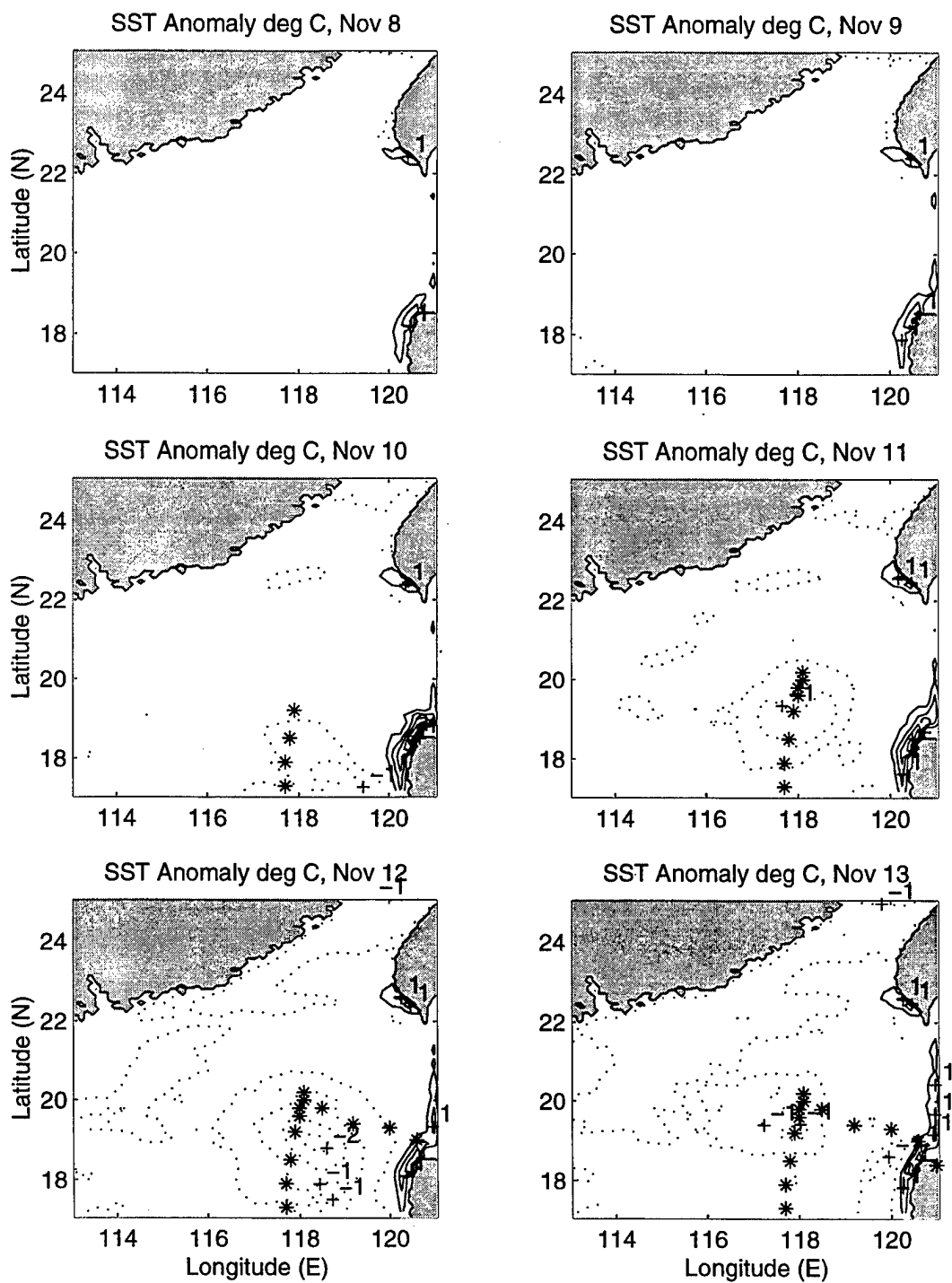


Figure 7.28. Sea surface temperature anomaly ($^{\circ}\text{C}$) for Analysis Area Two, November 8 to 13, 1996. Temperature changes relative to November 4 SST model field.

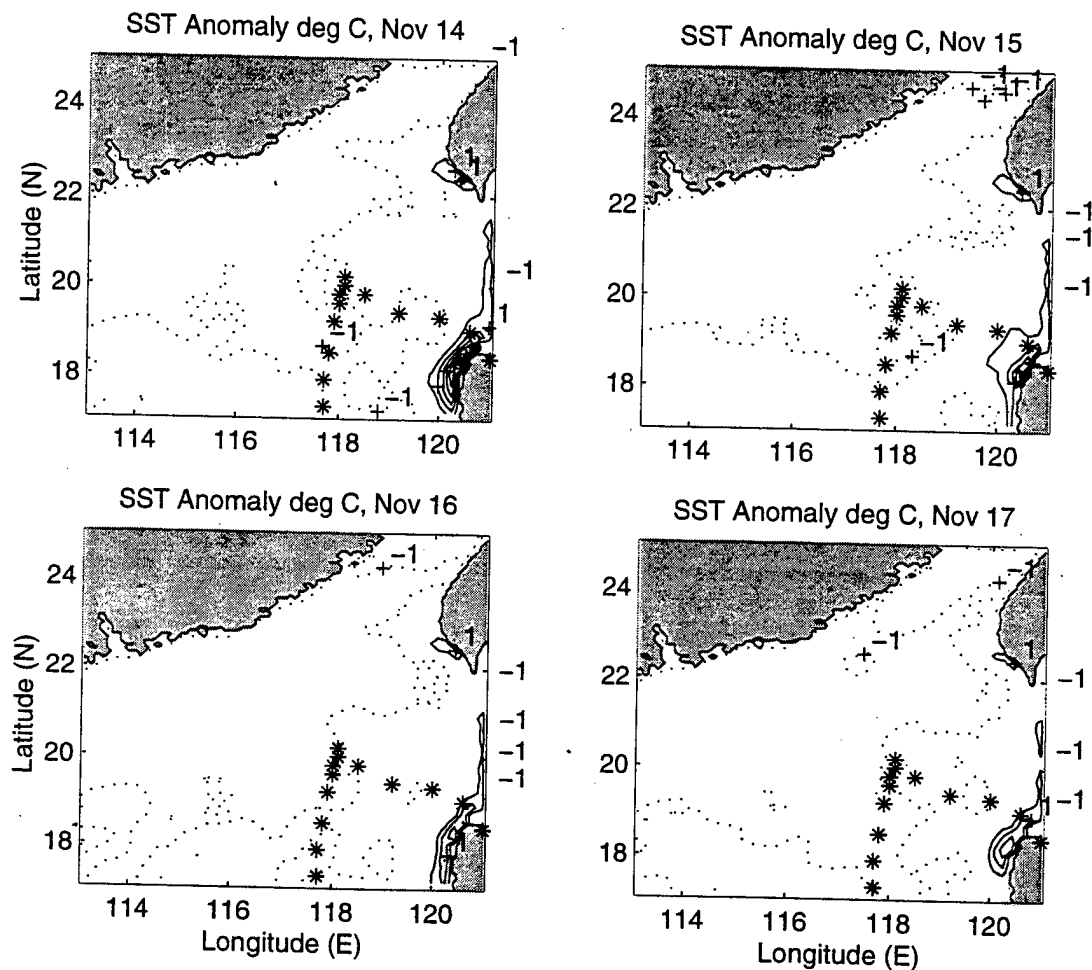


Figure 7.29. Sea surface temperature anomaly ($^{\circ}\text{C}$) for Analysis Area Two, November 14 to 17, 1996. Temperature changes relative to November 4 SST model field.

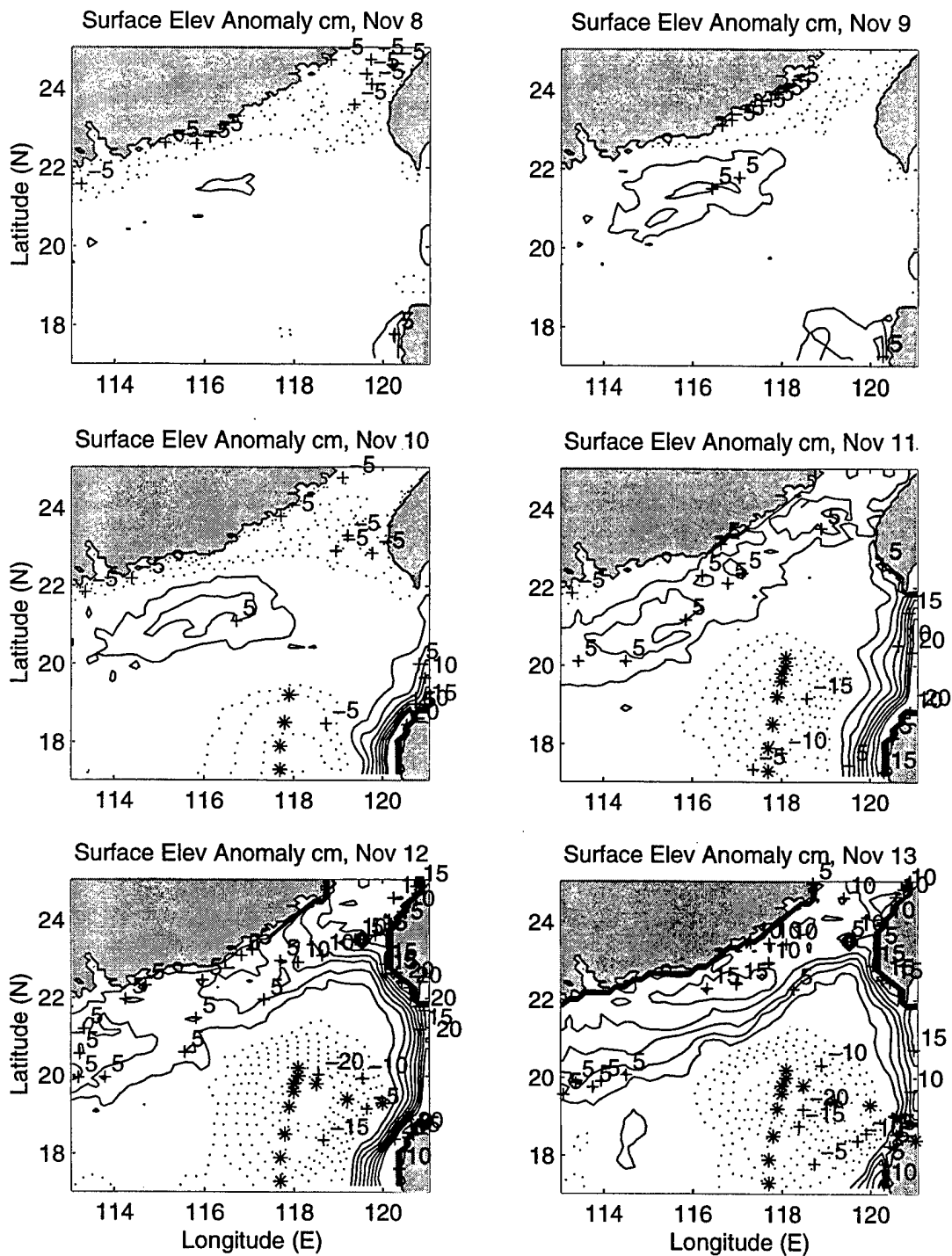


Figure 7.30. Sea surface elevation anomaly (cm) for Analysis Area Two, November 8 to 13. Elevation changes relative to November 4 sea surface elevation model field.

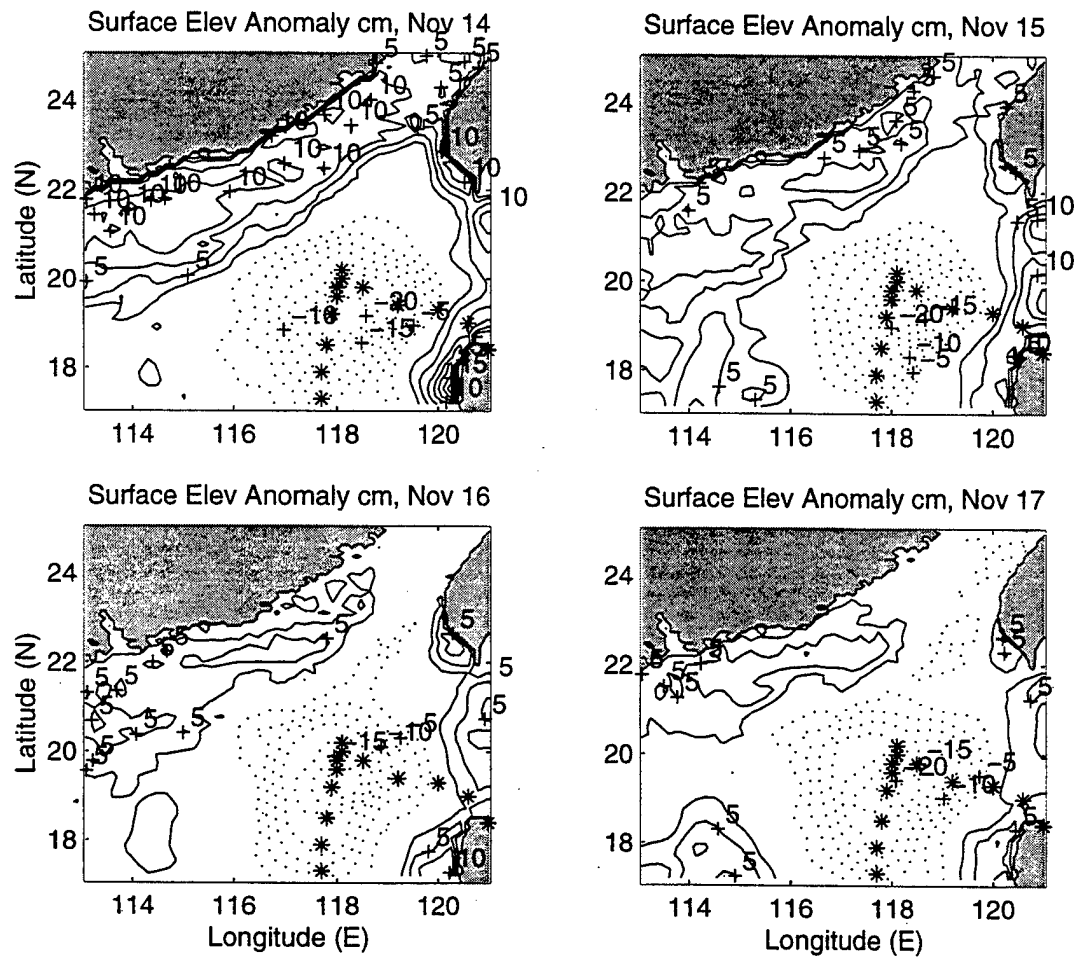


Figure 7.31. Sea surface elevation anomaly (cm) for Analysis Area Two, November 14 to 17. Elevation changes relative to November 4 sea surface elevation model field.

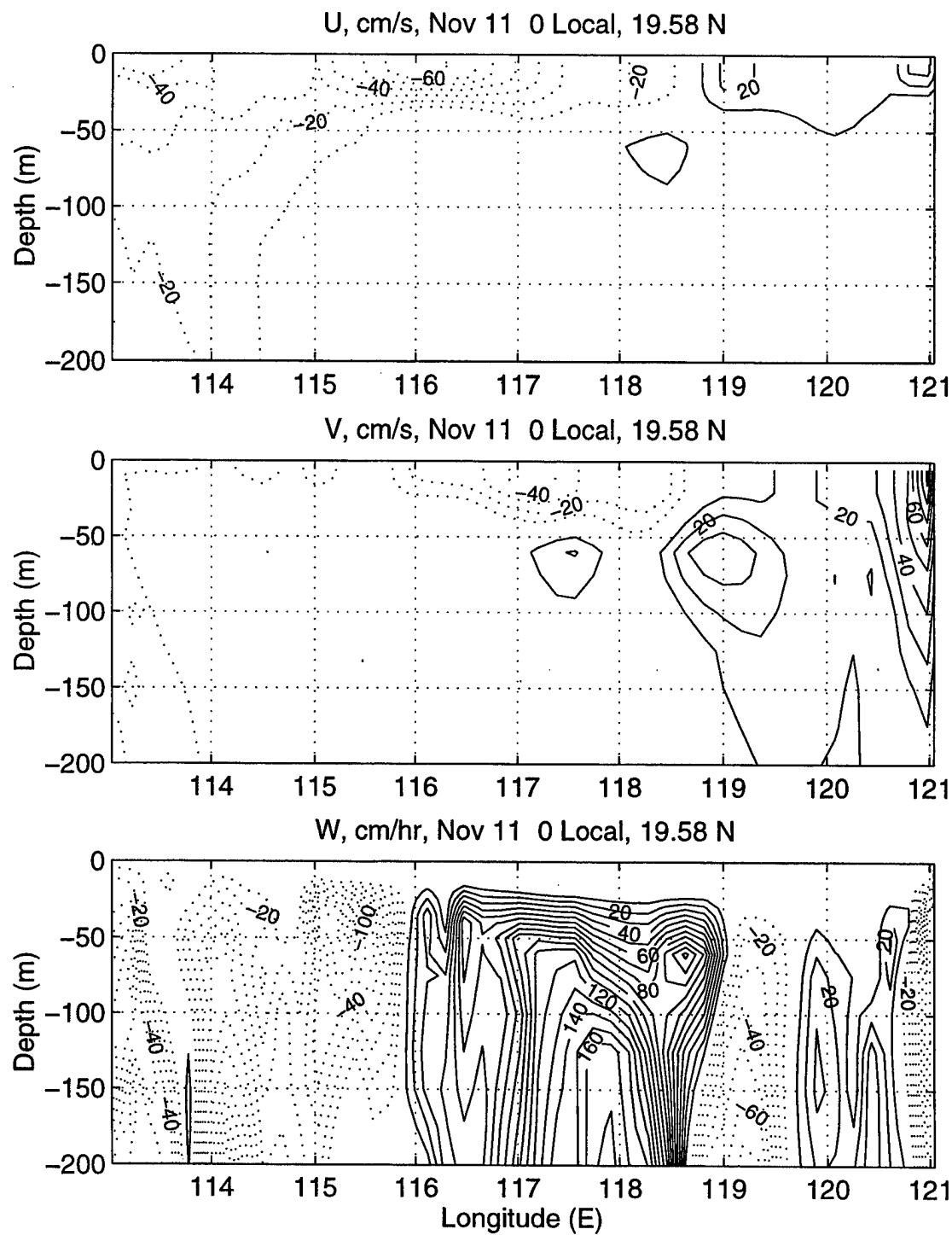


Figure 7.32. Analysis Area Two latitudinal cross section of model u, v (cm/s) and w (cm/hr) velocities along 19.6° N for November 11, 1996.

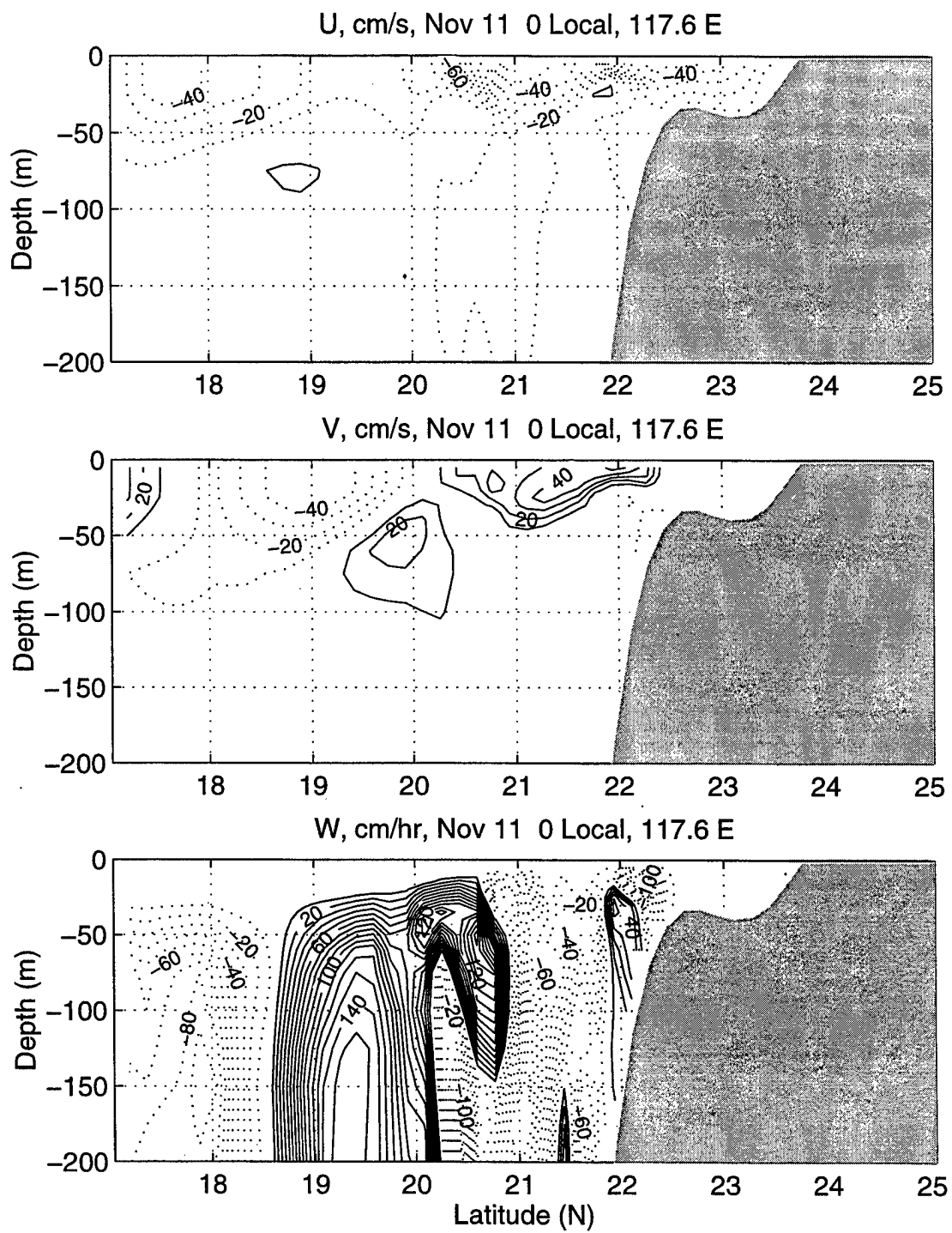


Figure 7.33. Analysis Area Two longitudinal cross section of model u, v (cm/s) and w (cm/hr) velocities along 117.6°E for November 11, 1996.

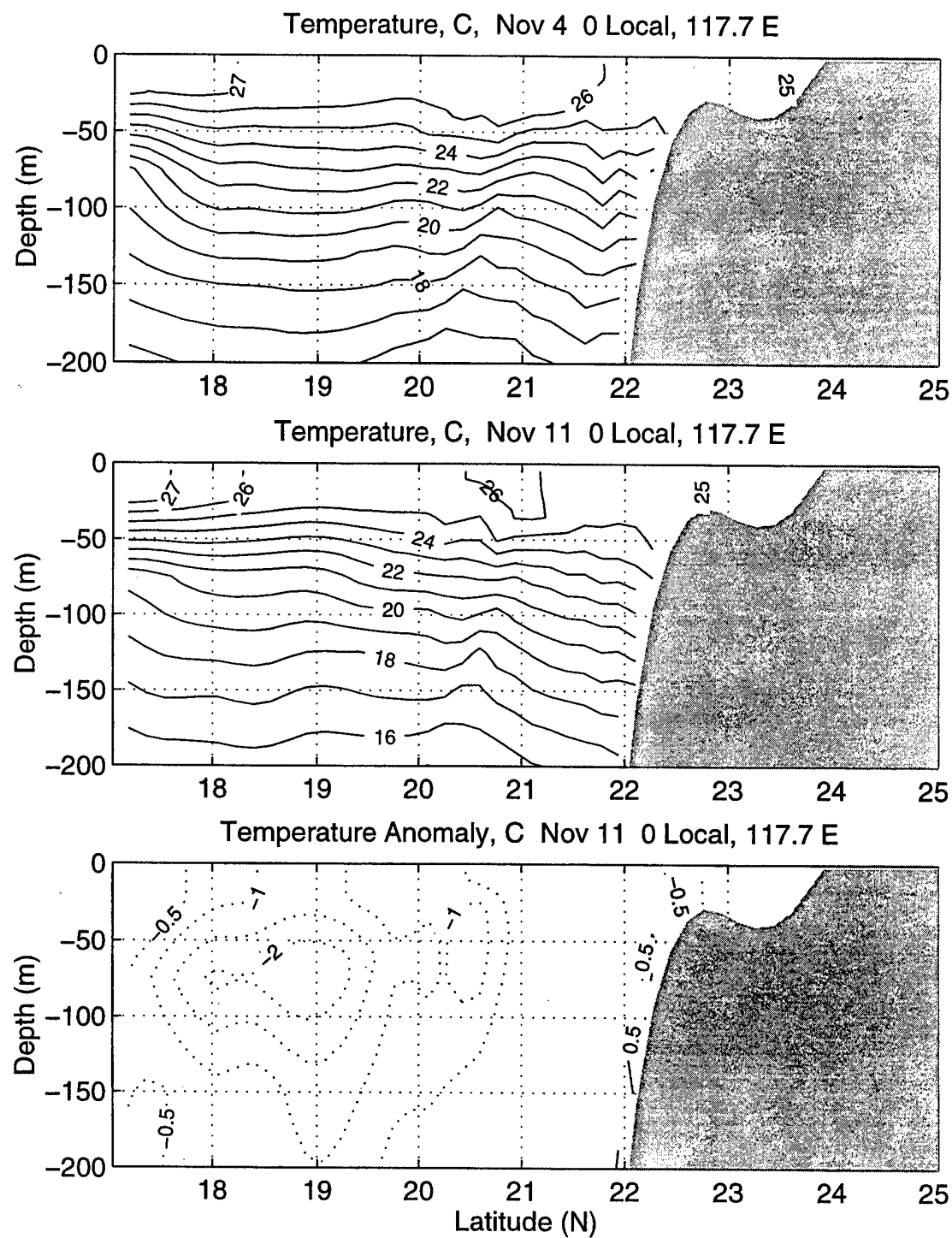


Figure 7.34. Analysis Area Two longitudinal cross section of the temperature anomaly ($^{\circ}\text{C}$) along 117.7°E for November 11, 1996. Anomaly relative to November 4 temperature model fields.

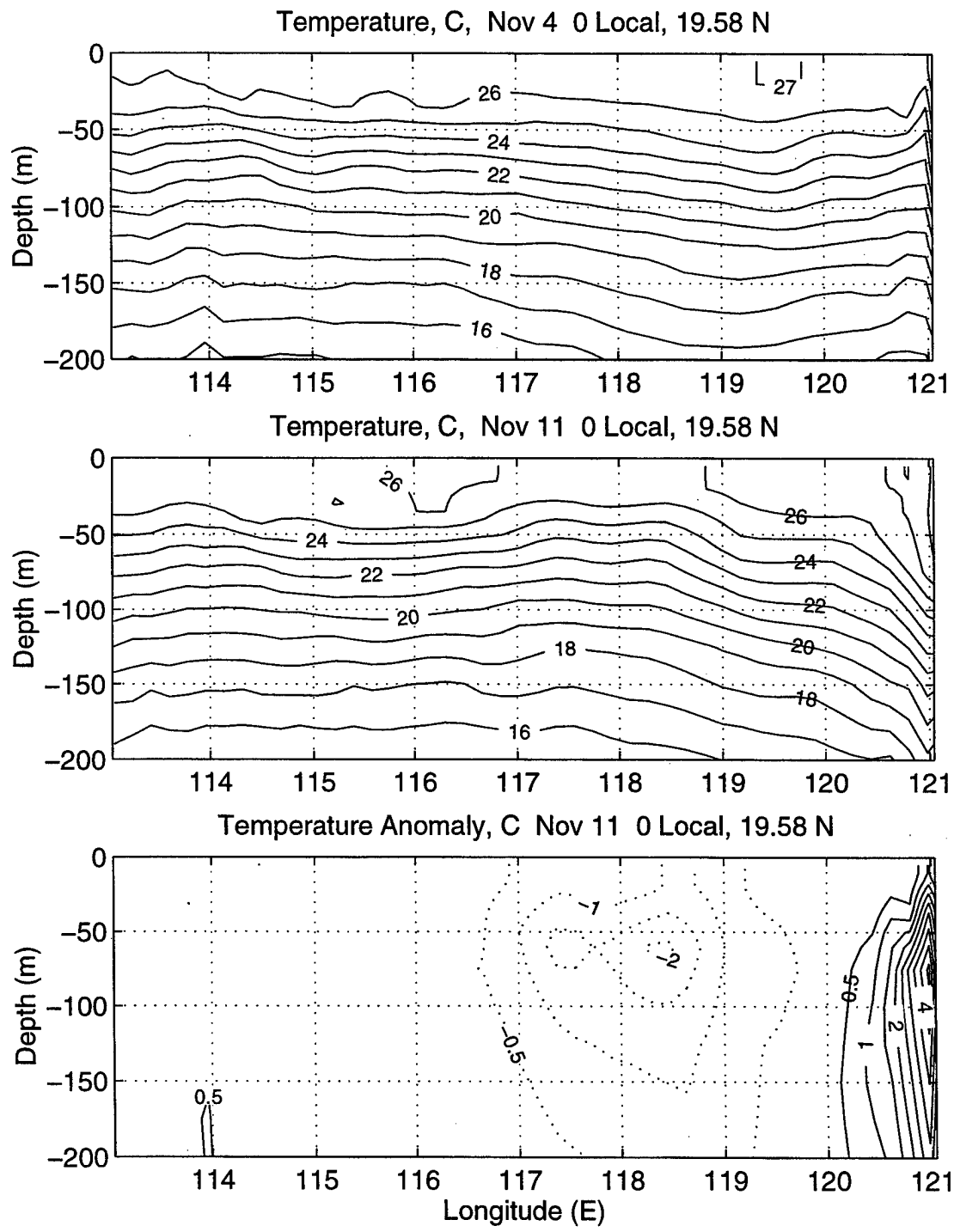


Figure 7.35. Analysis Area Two latitudinal cross section of the temperature anomaly ($^{\circ}\text{C}$) along 19.6°N for November 11, 1996. Anomaly relative to November 4 temperature model fields.

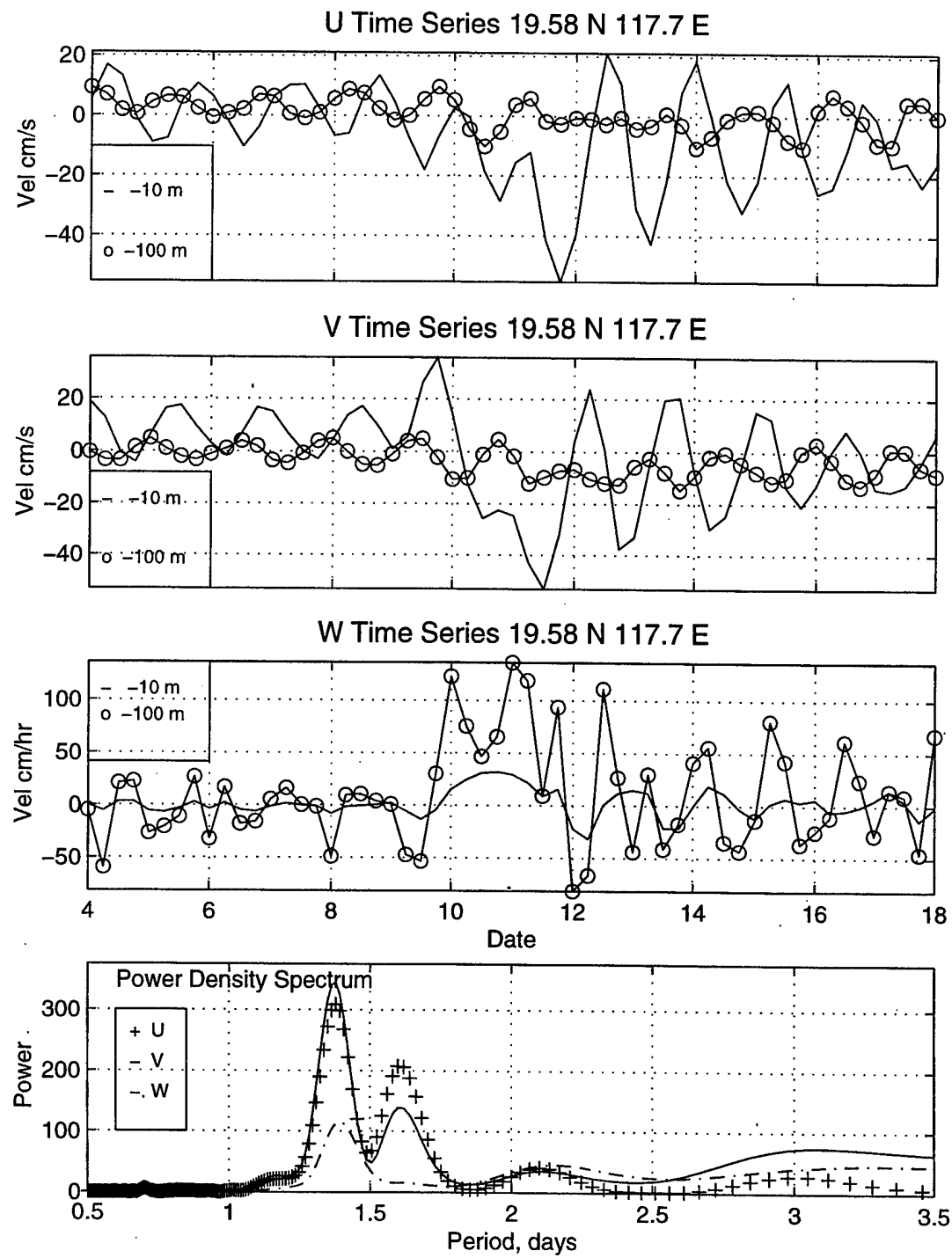


Figure 7.36. Time series and power density spectrum of model u, v and w velocities at 19.6° N, 117.7° E, from November 4 to 18.

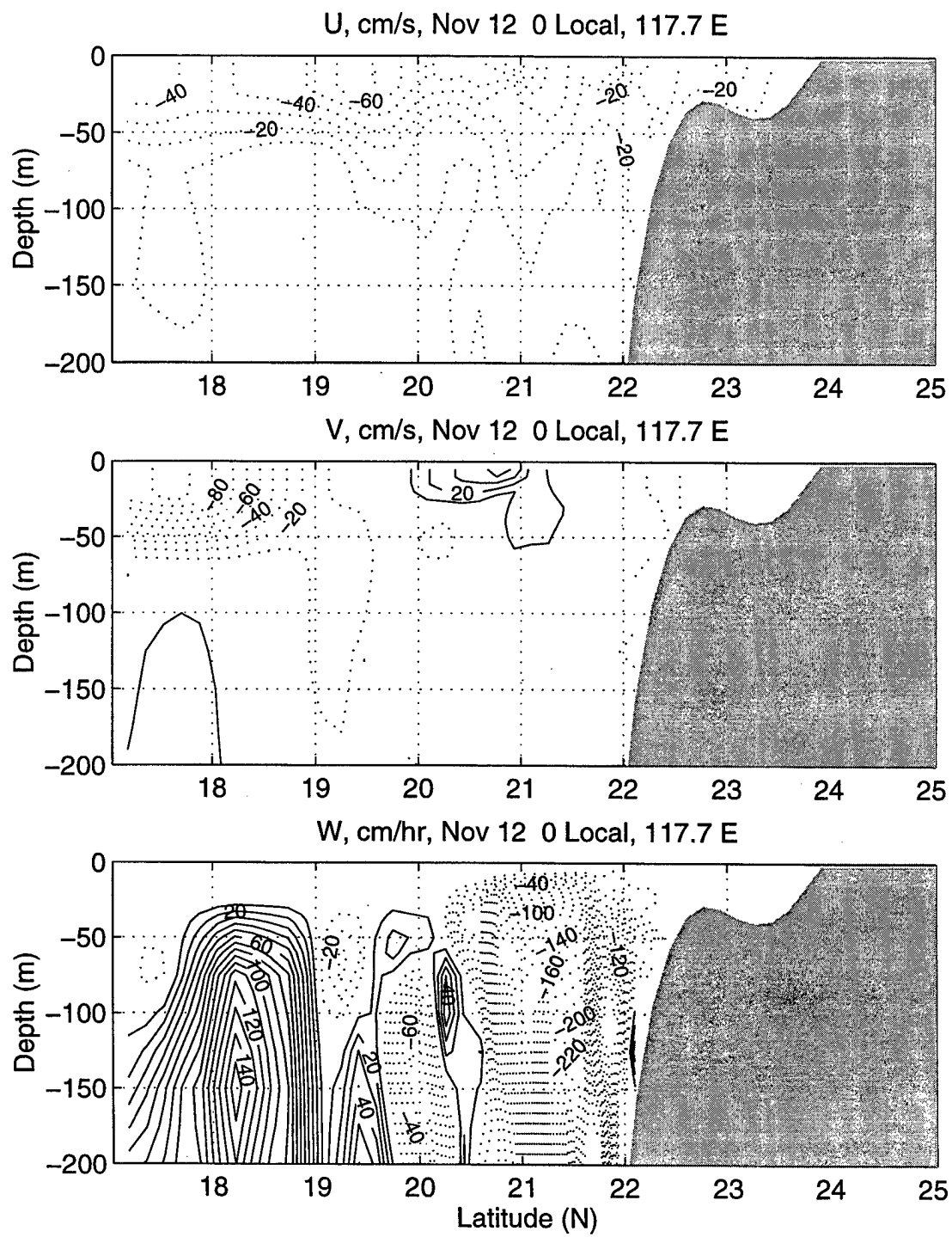


Figure 7.37. Analysis Area Two longitudinal cross section of model u, v (cm/s) and w (cm/hr) velocities along 117.7° E for November 12, 1996.

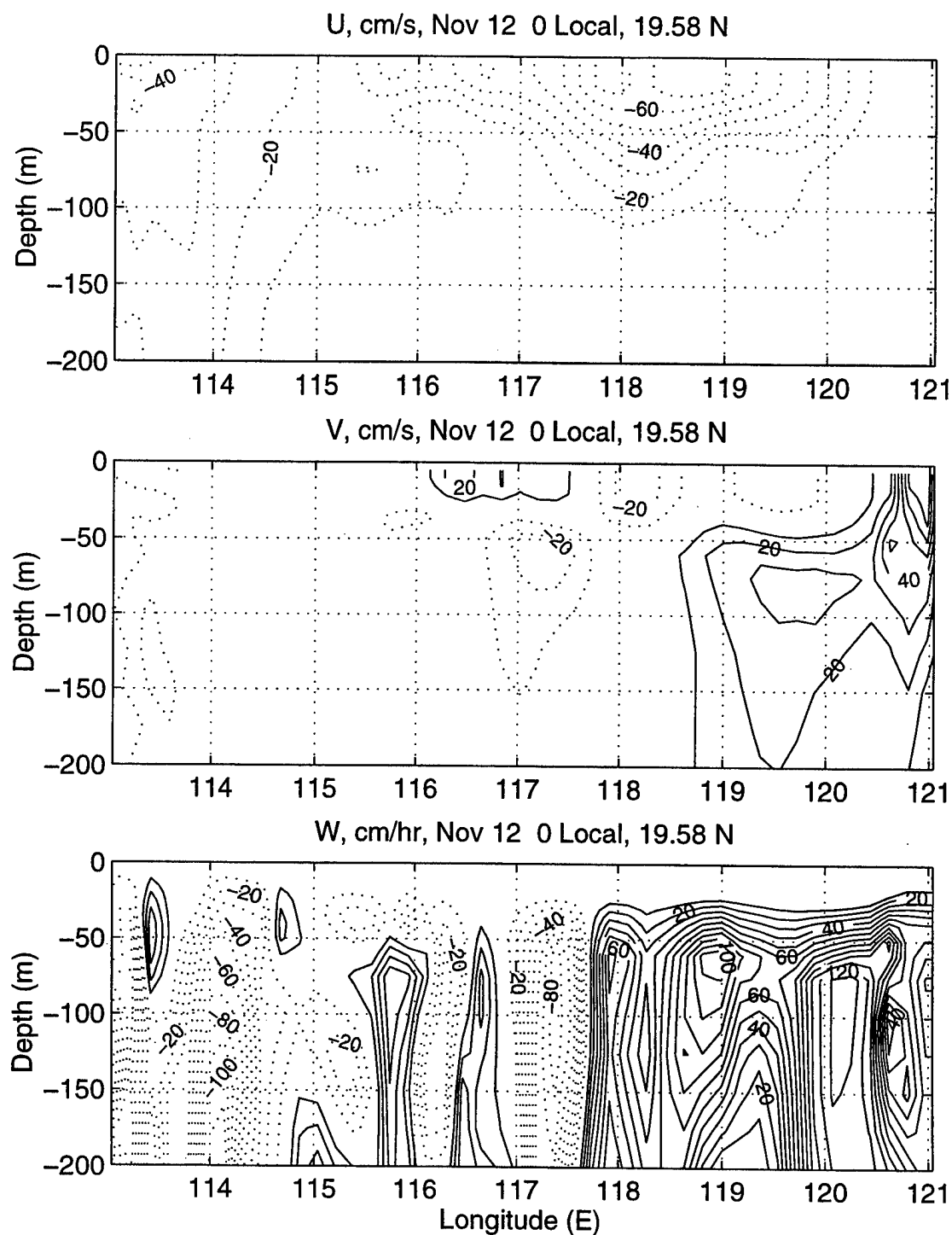


Figure 7.38. Analysis Area Two latitudinal cross section of model u, v (cm/s) and w (cm/hr) velocities along 19.6°E for November 12, 1996.

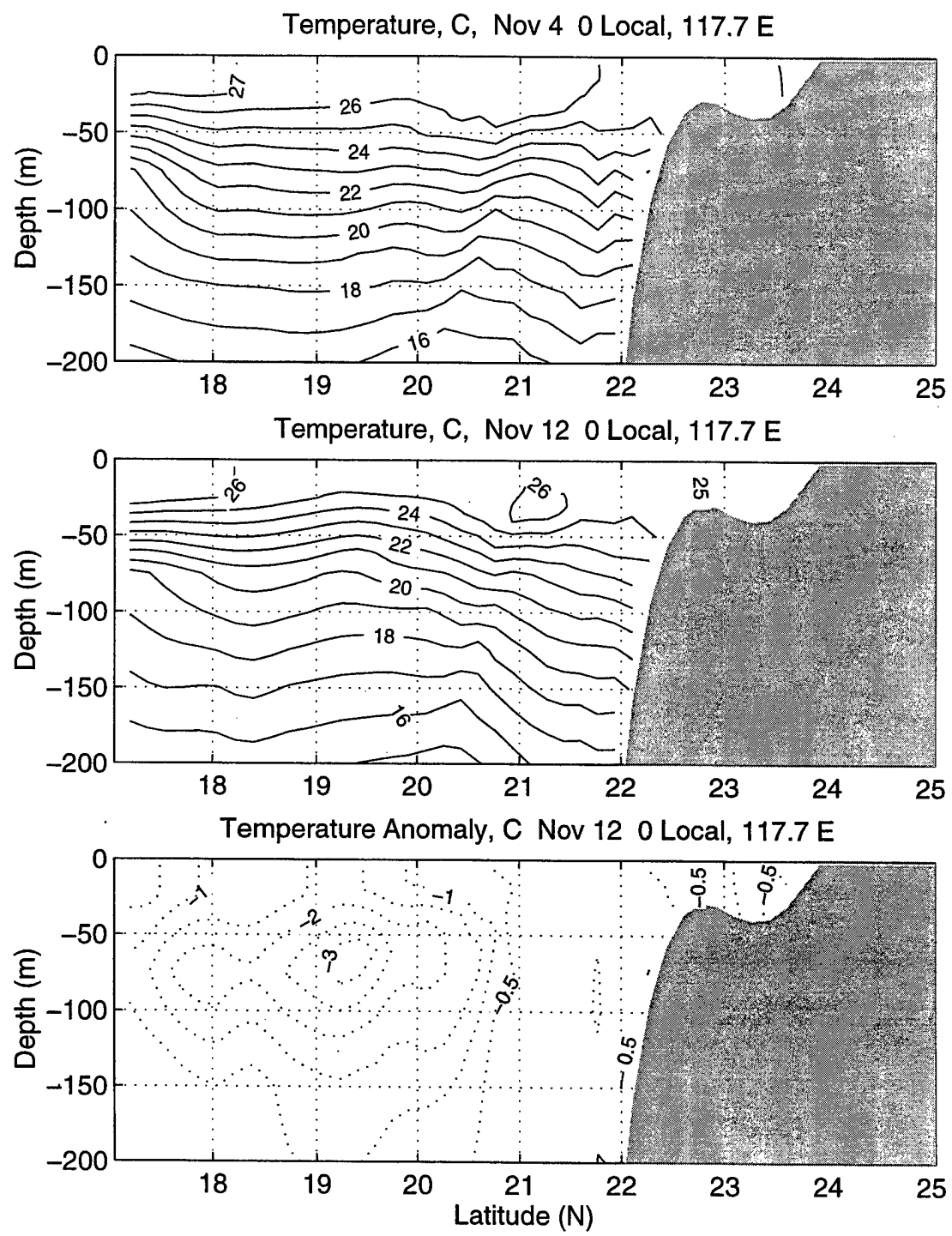


Figure 7.39. Analysis Area Two longitudinal cross section of the temperature anomaly ($^{\circ}\text{C}$) along 117.7°E for November 12, 1996. Anomaly relative to November 4 temperature model fields.

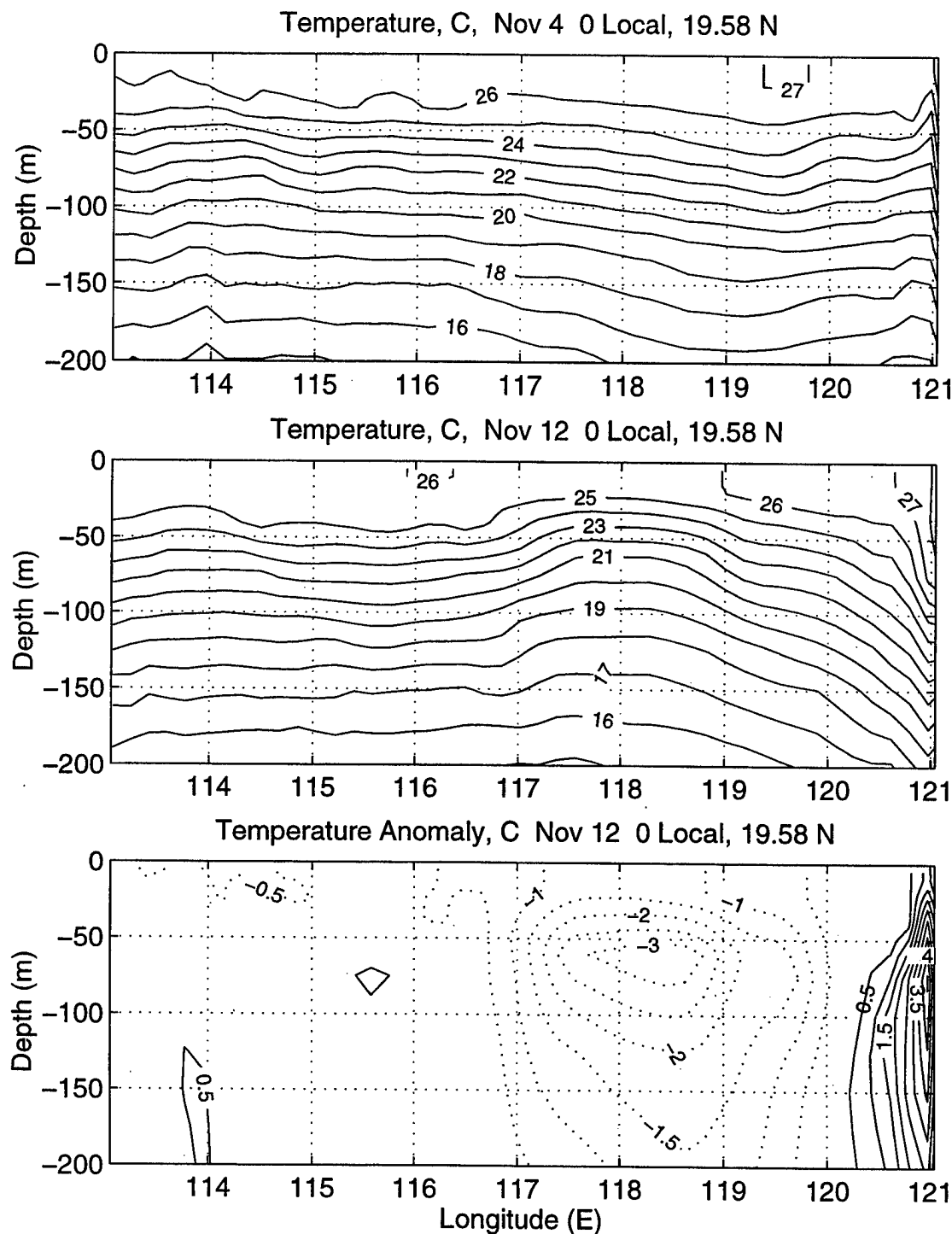


Figure 7.40. Analysis Area Two latitudinal cross section of the temperature anomaly ($^{\circ}\text{C}$) along 19.6°N for November 12, 1996. Anomaly relative to November 4 temperature model fields.

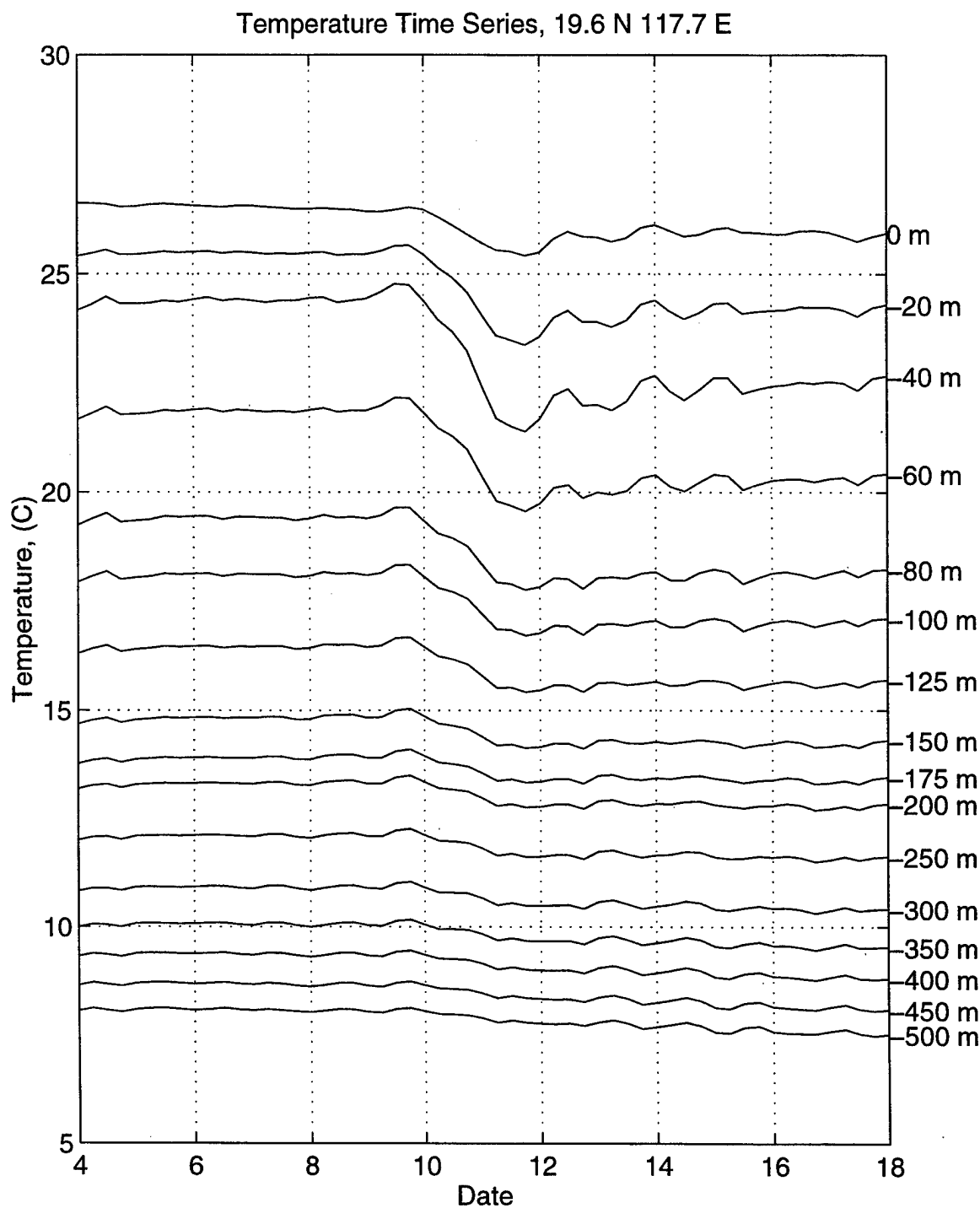


Figure 7.41. Time series of model sub-surface temperature ($^{\circ}\text{C}$) at 19.6°N , 117.7°E , from November 4 to 18.

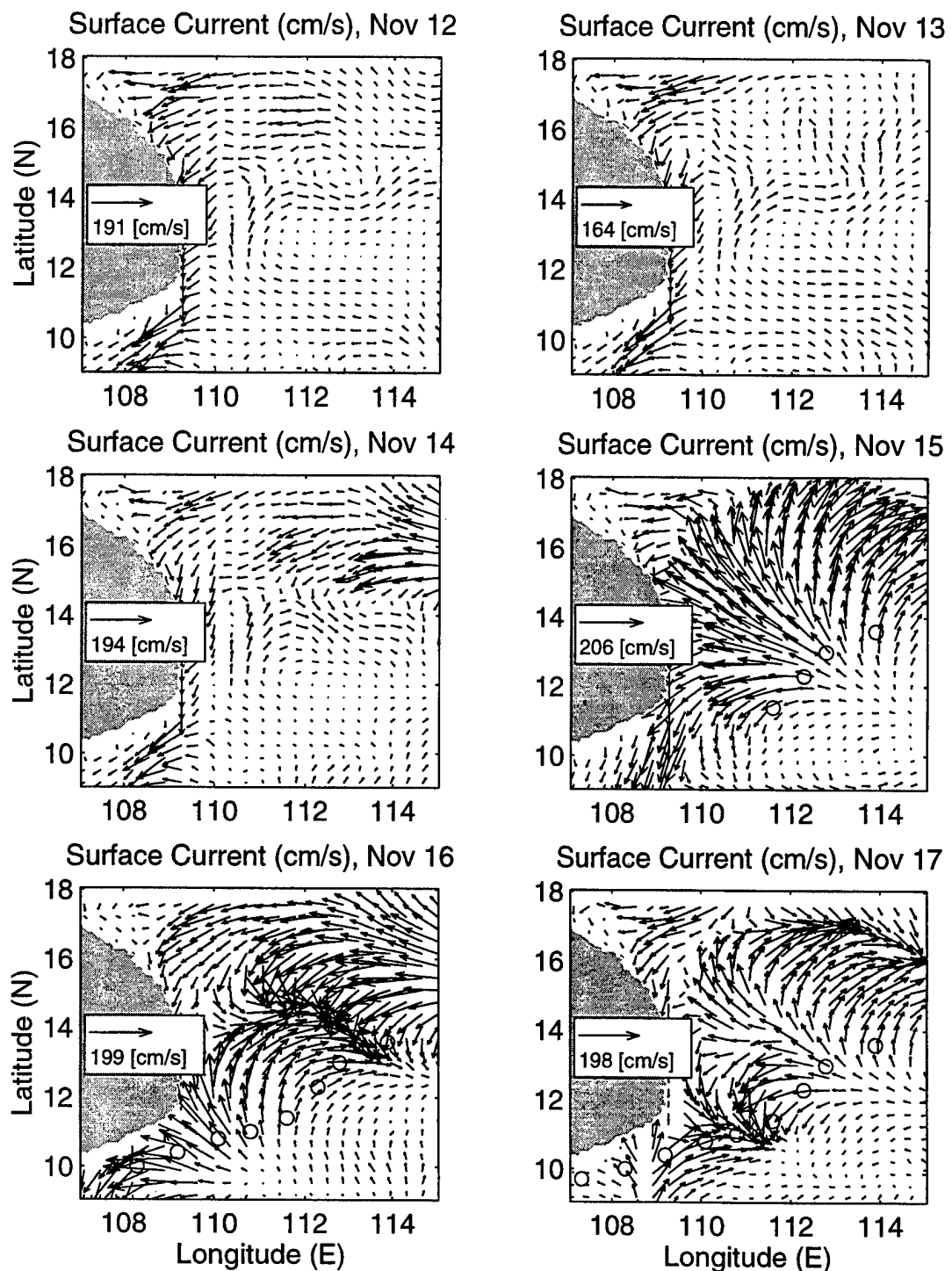


Figure 7.42. Surface current (cm/s) for Analysis Area Three, November 12 to 17, 1996.

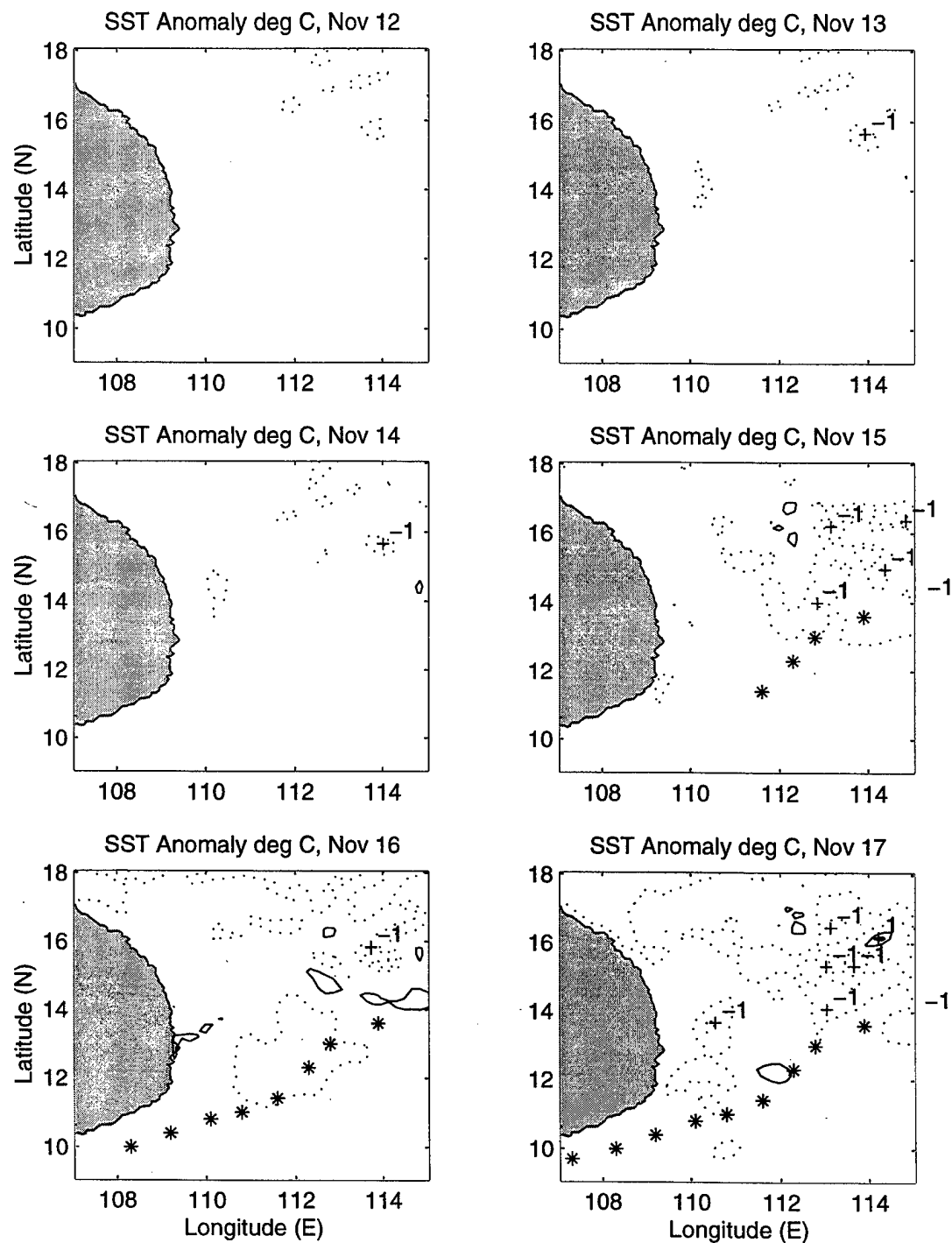


Figure 7.43. Sea surface temperature anomaly ($^{\circ}\text{C}$) for Analysis Area Three, November 12 to 17, 1996. Temperature changes relative to November 4 SST model field.

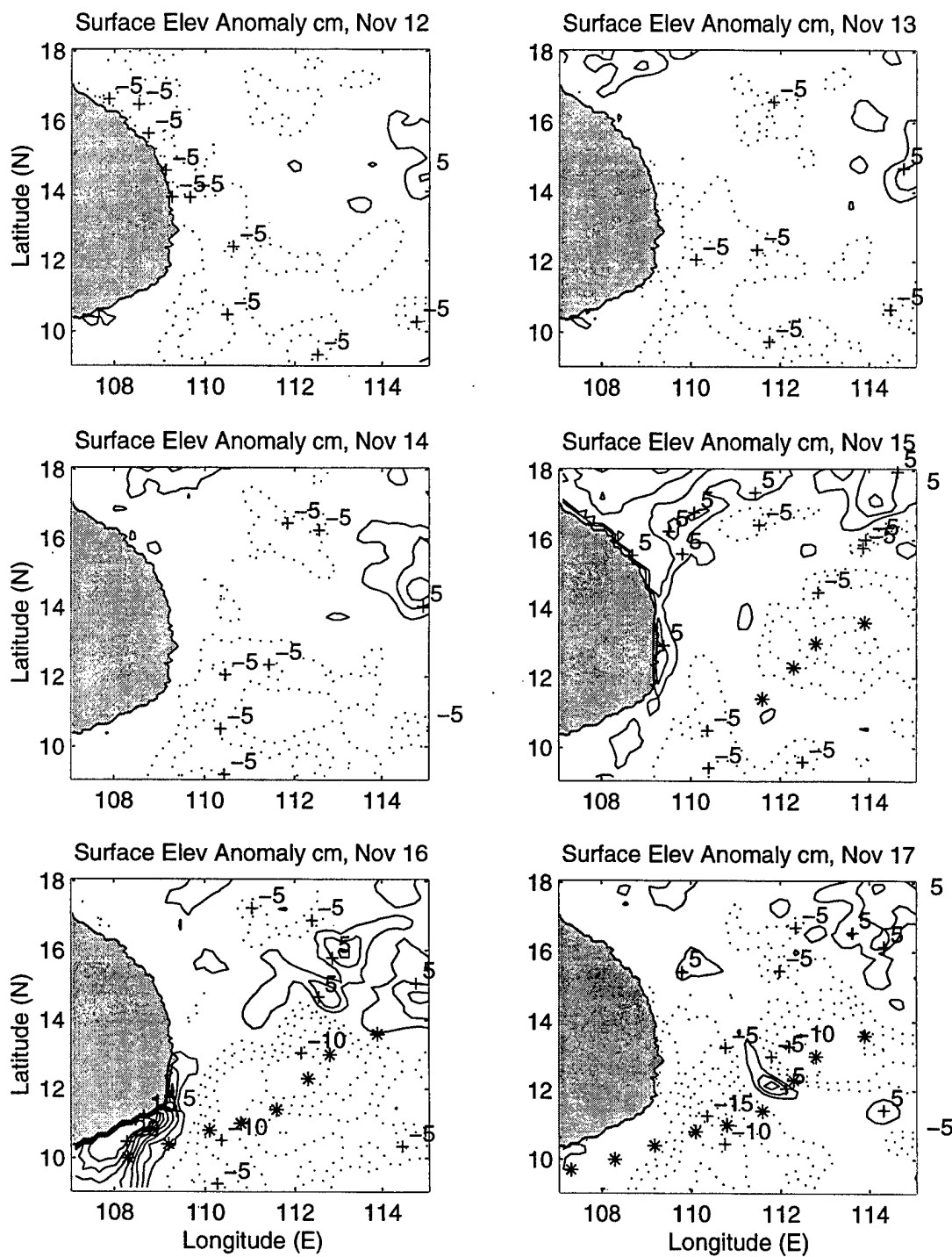


Figure 7.44. Sea surface elevation anomaly (cm) for Analysis Area Three, November 12 to 17. Elevation changes relative to November 4 sea surface elevation model field.

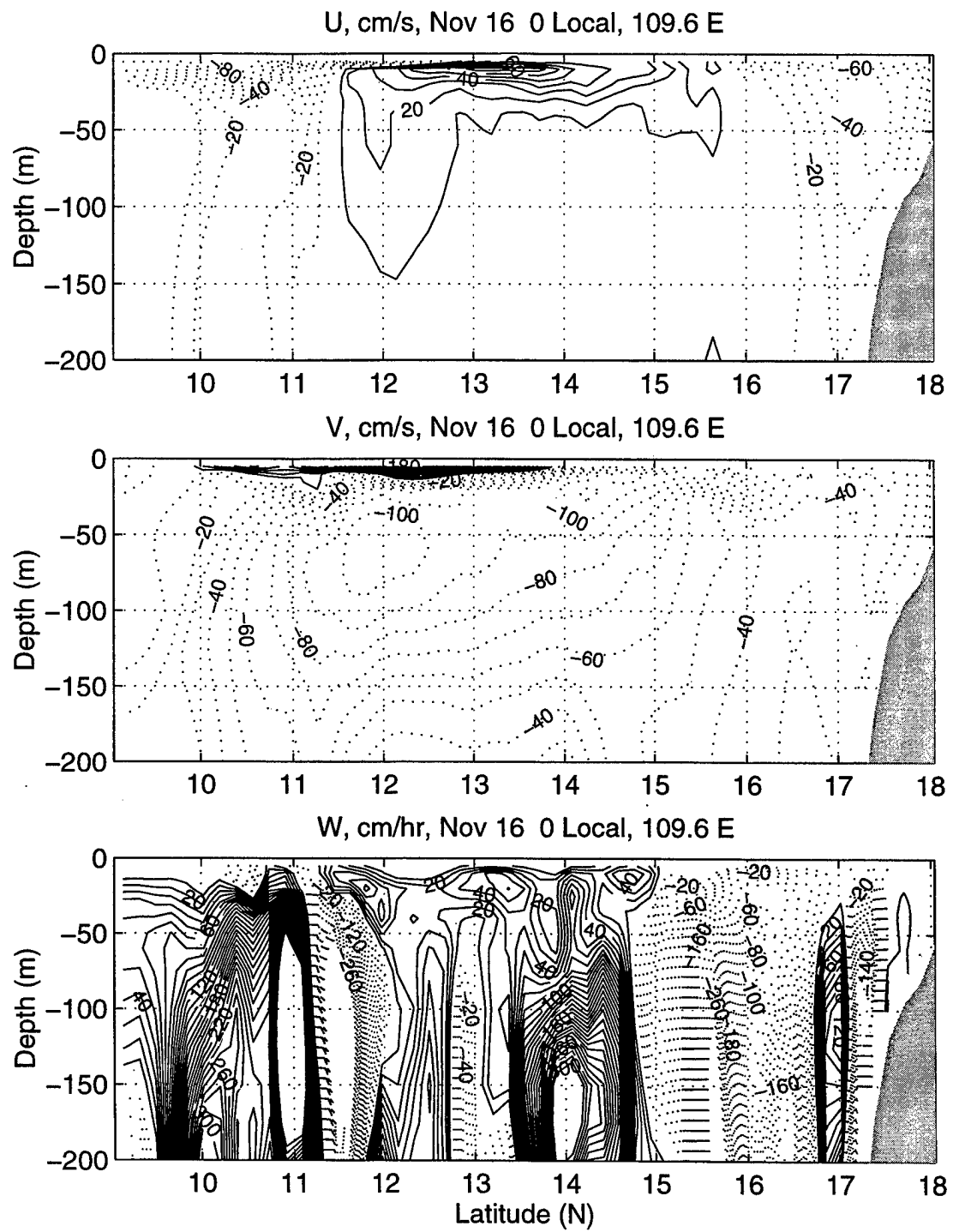


Figure 7.45. Analysis Area Three longitudinal cross section of model u, v (cm/s) and w (cm/hr) velocities along 109.6°N for November 16, 1996.

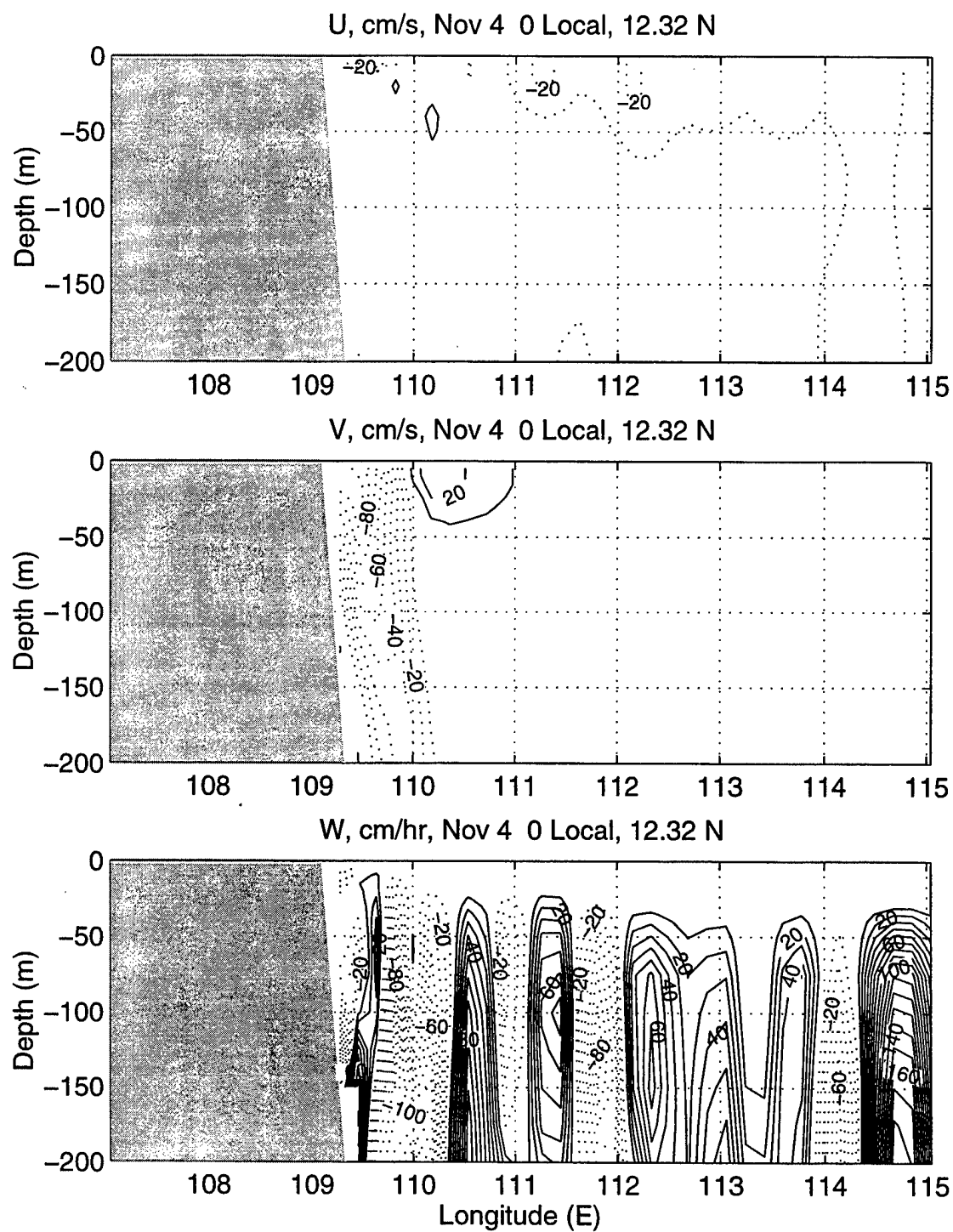


Figure 7.46. Analysis Area Three latitudinal cross section of model u , v (cm/s) and w (cm/hr) velocities along 12.3° E for November 4, 1996.

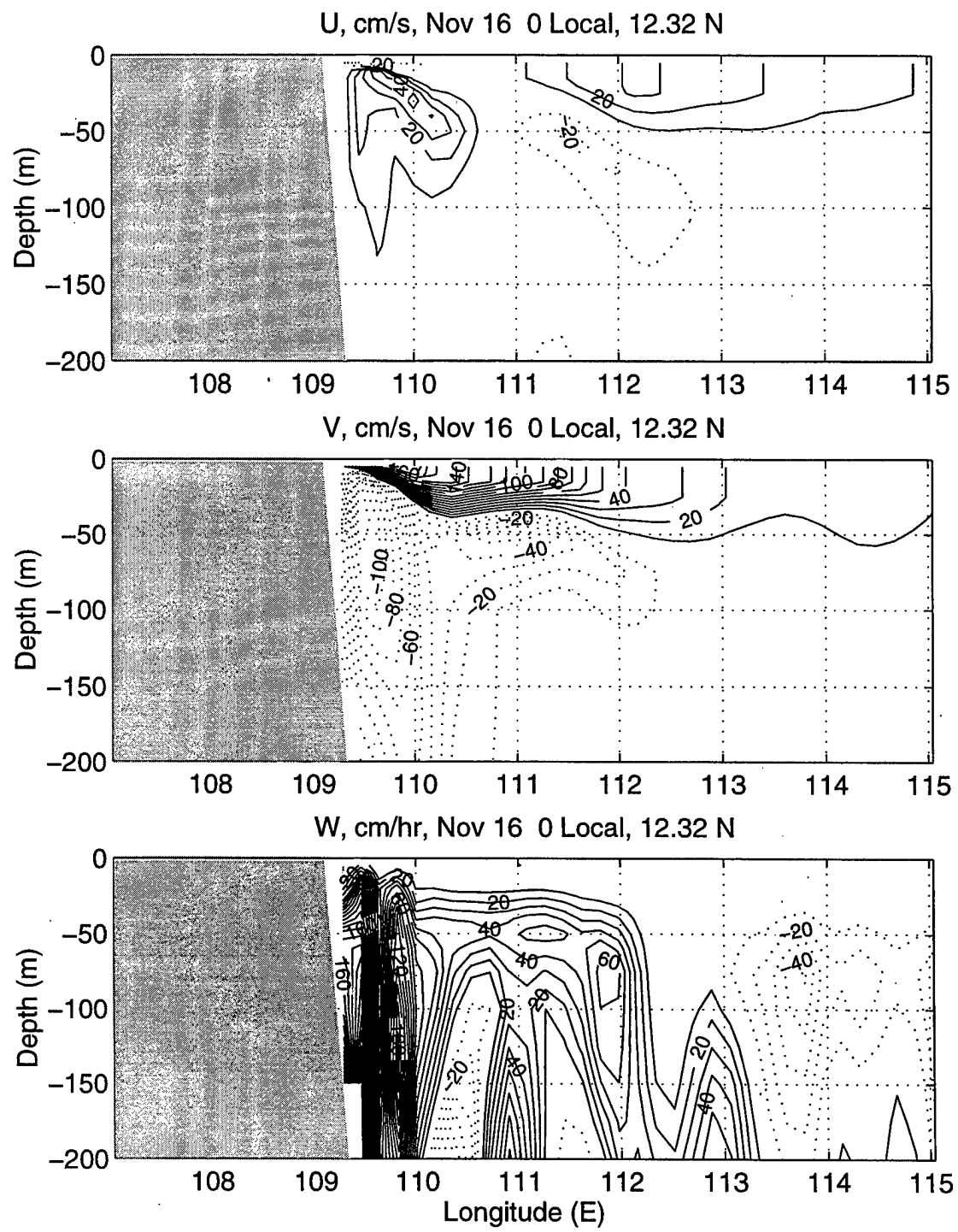


Figure 7.47. Analysis Area Three latitudinal cross section of model u , v (cm/s) and w (cm/hr) velocities along 12.3° E for November 16, 1996.

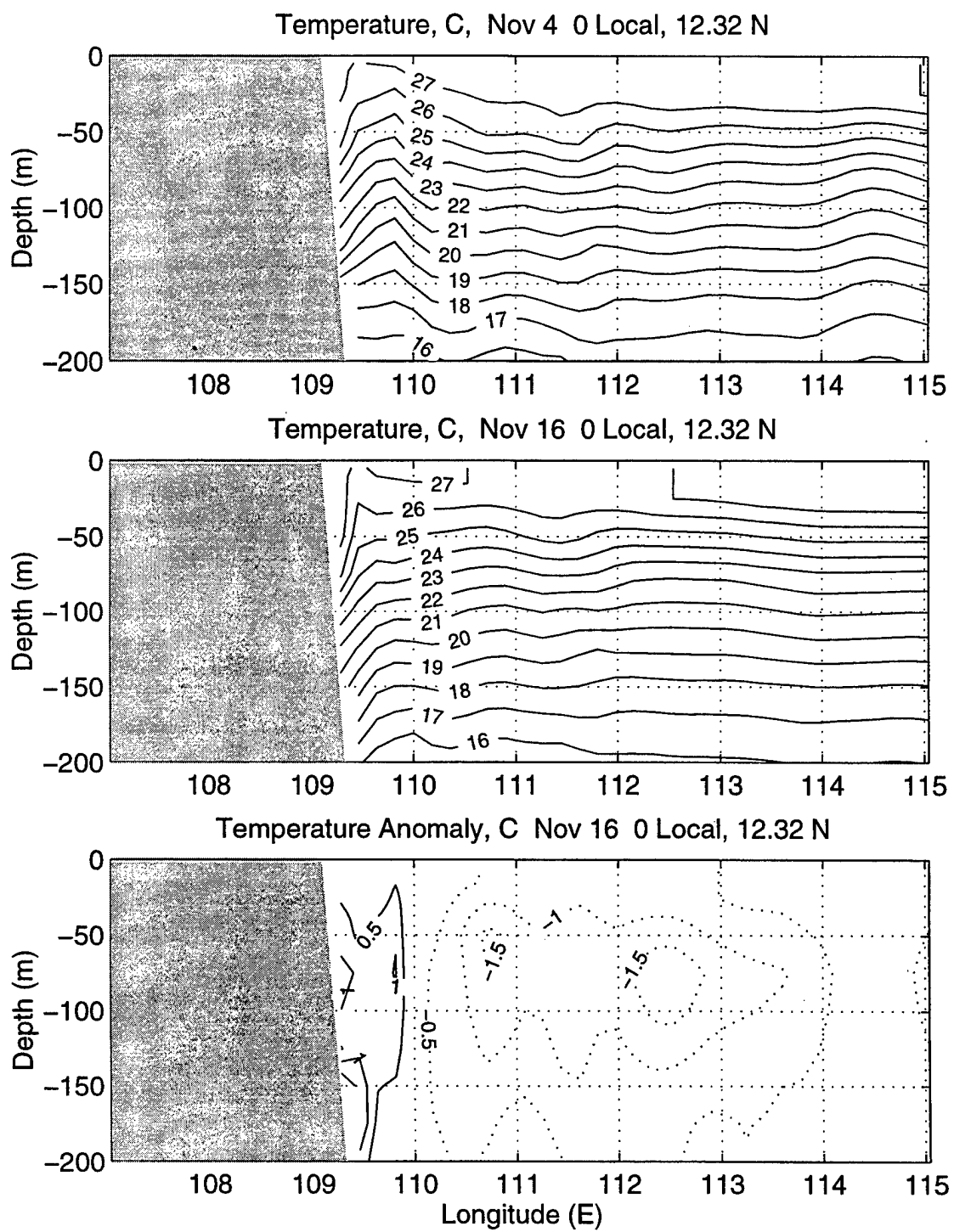


Figure 7.48. Analysis Area Three latitudinal cross section of the temperature anomaly ($^{\circ}\text{C}$) along 12.3°N for November 16, 1996. Anomaly relative to November 4 temperature model fields.

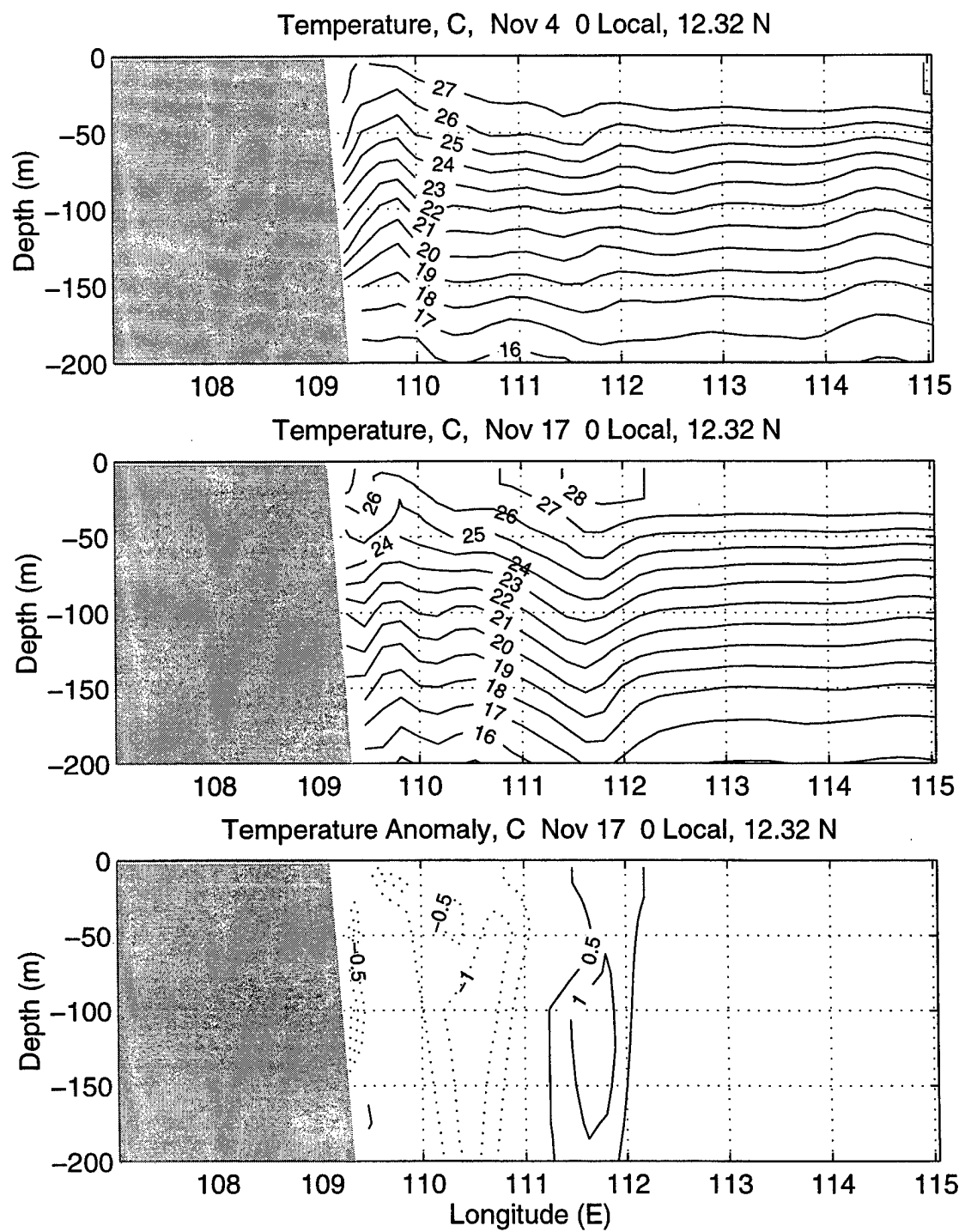


Figure 7.49. Analysis Area Three latitudinal cross section of the temperature anomaly ($^{\circ}\text{C}$) along 12.3°N for November 17, 1996. Anomaly relative to November 4 temperature model fields.

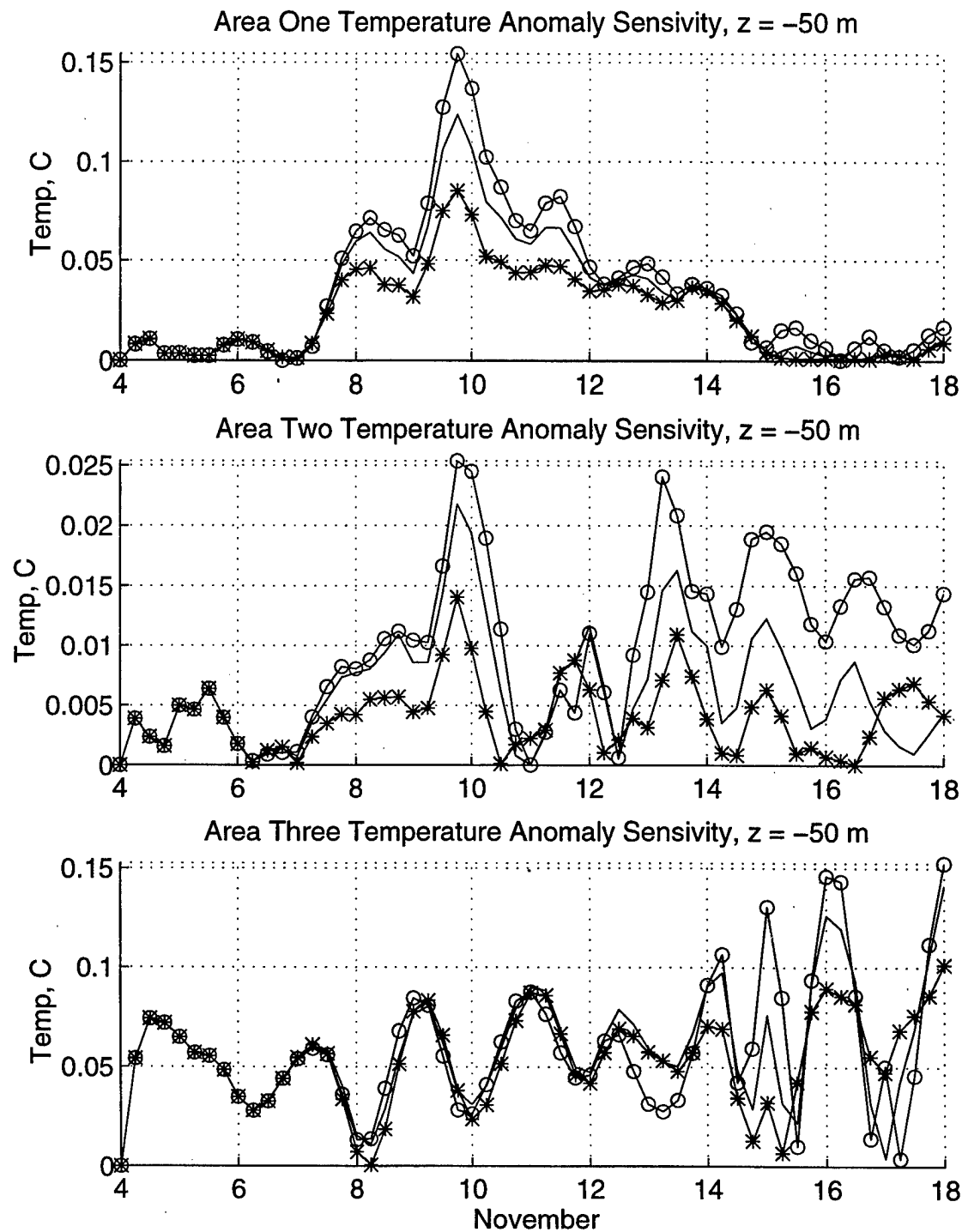


Figure 7.50. Temperature anomaly ($^{\circ}\text{C}$) at $z = -50$ m for the three analysis areas. Anomaly between main experimental run, $X = 0.15$ and sensitivity experimental runs for $X = 0.26$ (*), $X = 0.35$ (—), and $X = 0.46$ (○).

VIII. CONCLUSIONS

The South China Sea (SCS) is a dynamic and highly variable semi-enclosed sea that is subject to complex environmental forcing. The tropical cyclones that periodically move through the region produce the most significant forcing. Ocean responses generated by the wind stress of these storms include significant upper oceanic layer cooling, strong currents, high surface waves and storm surges. These responses have the potential to affect maritime and coastal operations dramatically. An understanding of these responses is therefore critical.

Researchers can only accomplish such an understanding through the retrieval and thorough analysis of oceanographic data. Because of the erratic nature of tropical cyclones, the collection of ocean data on a fine enough scale to resolve the mesoscale and sub-mesoscale features produced by tropical cyclones is nearly impossible however. Therefore, researchers must rely on numerical modeling techniques to gain an insight into these processes.

This study used the Princeton Ocean Model (POM) to investigate ocean responses generated by Tropical Cyclone Ernie, which affected the SCS from November 8 to 18, 1996. A model was developed to simulate Tropical Cyclone Ernie's wind stress forcing and used to force the POM for this fourteen day period. POM velocity, temperature, salinity and surface elevation fields were then analyzed to investigate ocean responses produced by the storm.

The model satisfactorily simulated the unique asymmetrical upper-ocean current pattern produced by a moving tropical cyclone, which researchers have seen in many past studies. The model generated strong near-inertial, anticyclonic turning upper-ocean currents to the right of the storm track. These highly divergent upper-layer currents also generated the typical bias of maximum sea surface temperature cooling to the right of the storm track. Sub-surface responses were also consistent with observations and numerical studies of other storms. The highly divergent surface currents produced strong upwelling. Maximum cooling associated with this upwelling was also found to the right of the storm track at the base of the mixed layer. The model fields depicted intense current shear between the mixed layer and thermocline, with 180° reversal of these currents. Sea surface depressions developed in the wake of the storm were also similar to studies of other storms.

The model also simulated several unique features, apparently caused by coastal interactions with storm forcing. Along the coast of Luzon storm forcing formed a sub-surface alongshore jet near the coast. Northward alongshore surface flow, produced by the divergent near-surface currents, significantly enhanced a warm anomaly off the northern tip of Luzon.

A comparison of these model responses with multi-channel sea surface temperature (MCSST), expendable bathythermograph (XBT) and satellite sea surface elevation observations was done. This comparison suggests that the model temperature and elevation fields were consistent with the actual state of the SCS.

One purpose of this thesis was to investigate the POM's ability to capture the highly dynamic ocean responses generated by Tropical Cyclone Ernie (1996). A review of these ocean responses and the available limited observations shows that the model adequately simulated the ocean responses to this tropical cyclone forcing. However, much more work in modeling ocean forcing by tropical cyclones is required to gain a more thorough insight into these responses. To improve this effort more ocean and atmosphere observations along with a more realistic atmospheric model are required. Three-dimensional observations of ocean temperature, salinity and velocity fields would allow initialization of the model with a more realistic pre-storm thermodynamic structure. Observations retrieved during the passage of a tropical cyclone would greatly improve the analysis of the ocean responses to the storm forcing. Storm forcing would also be more realistic by utilizing a coupled Ocean/Atmosphere model, such as the Coupled Ocean/Atmosphere Mesoscale Prediction System (COAMPS) under development by the United States Naval Research Laboratory at Monterey California. Use of such a system would provide more accurate wind stress forcing, through modifications of the wind field by surface frictional effects, and improved ocean/atmosphere thermal and salinity fluxes.

LIST OF REFERENCES

Bender, M.A., Ginis, A.I. and Kurihara, Y., Numerical simulations of the tropical cyclone-ocean interaction with a high resolution coupled model, *Journal of Geophysical Research*, 98, 23245-23263, 1993.

Bender, M.A. and Ginis, A.I., Real case simulations of hurricane-ocean interaction using a high resolution coupled model: Effect on hurricane intensity. Submitted to *Monthly Weather Review*, 1997.

Black, P.G., Ocean temperature changes induced by tropical cyclones. Ph.D. dissertation, The Pennsylvania State University, College Park, 278 pp., 1983.

Blumberg, A., and Mellor, G., A description of a three dimensional coastal ocean circulation model, in *Three-Dimensional Coastal Ocean Models*, edited by N.S. Heaps, American Geophysics Union, Washington D.C., 1-16, 1987.

Blumberg, F. and Mellor, G., A simulation of the circulation in the Gulf of Mexico, *Israel Journal of Earth Science*, 34, 122-144, 1985.

Carr, L.E., Barotropic vortex adjustment to asymmetrical forcing with application to tropical cyclones, Ph.D. dissertation, Naval Post Graduate School, Monterey, 143 pp, 1989.

Carr, L.E. and Elsberry, R.L., Models of tropical cyclone wind distribution and beta-effect propagation for application to tropical cyclone track forecasting, *Monthly Weather Review*, 125, 3190-3209, 1997.

Chang, S.W., Deep ocean response to hurricanes as revealed by an ocean model with a free-surface. Part 1: Asymmetrical case, *Journal of Physical Oceanography*, 15, 1847-1858, 1985.

Cheang, B.K., Short and long-range monsoon prediction in southeast Asia, in *Monsoon*, edited by Fein, J.S. and Stephens, P.L., 579-606, John Wiley, New York, 1987.

Chu, P.C., Li, C.C., Ko, D.S. and Mooers, C.N.K., Response of the South China Sea to seasonal monsoon forcing, Proceedings of the Second International Conference on Air-Sea Interaction and Meteorology and Oceanography of the Coastal Zone, American Meteorological Society, Boston, 214-215, 1994.

Chu, P.C., Huang, M.J. and Fu, E.X., Formation of the South China Sea warm core eddy in boreal spring, Proceedings of the Eighth Conference on Air-Sea Interaction, American Meteorological Society, Boston, 155-159, 1996.

Chu, P.C., Tseng, H.C., Chang, C.P. and Chen, J.M., South China Sea warm pool detected in spring from the Navy's Master Oceanographic Observational Data Set (MOODS), *Journal of Geophysical Research*, 102, 15,761-15,771, 1997.

Chu, P.C. and Chang, C.P., A case study of the South China Sea warm pool, paper presented at the *International CLIVAR-GOALS Workshop on Asian-Australian Monsoon Oceanography and Meteorology*, UCAR Joint International Climate Projects/Planning Office, Melborne, Victoria, Australia, April 10-12, 1995.

Edmons, N.L., Studies of South China Sea circulation and thermal structure using a three dimensional numerical model, Masters thesis, Naval Post Graduate School, Monterey, 74 pp, 1996.

Elsberry, R.L., Tropical cyclone motion, in *Global Perspectives of Tropical Cyclones*, edited by Elsberry, R.L., World Meteorological Organization Technical Document No. 693, 106-192, 1995.

Emanuel, K.A., The maximum intensity of hurricanes, *Journal of Atmospheric Science*, 45, 1143-1155, 1988.

Ezer, T. and Mellor, G., A numerical study of the variability and the separation of the Gulf Stream, induced by surface atmospheric forcing and lateral boundary flows, *Journal of Geophysical Research*, 22, 660-682, 1992.

Fisher, E.L., Hurricanes and the sea surface temperature fields, *Journal of Meteorology*, 15, 328-333, 1958.

Geisler, J.E., Linear theory of the response if a two layer ocean to moving hurricane, *Geophysical Fluid Dynamics*, 1, 249-272, 1970.

Ginis, I. and Sutyrin, G.G., Hurricane-generated depth-averaged currents and sea surface elevation, *Journal of Physical Oceanography*, 25, 1218-1242, 1995.

Gray, W.M., Hurricanes: Their formation, structure and likely role in the tropical circulation, in *Meteorology Over the Tropical Oceans*, edited by Shaw D.B., Royal Meteorological Society, James Glaisher House, Grenville Place, Bracknell, Berkshire, 155-218, 1979.

Gray, W.M., Tropical cyclone genesis. Department of Atmospheric Science Paper No. 323, Colorado State University, Ft Collins, Co 80523, 121 pp, 1975.

Gray, W.M., Global view of the origin of tropical disturbances and storms, *Monthly Weather Review*, 96, 669-700, 1968.

Greatbatch, R.J., On the response of the ocean to a moving storm: The nonlinear dynamics, *Journal of Physical Oceanography*, 13, 357-367, 1983.

Haney, R.L., Surface boundary conditions for ocean circulation models, *Journal of Physical Oceanography*, 1, 241-248, 1971.

Hazelworth, J.B., Water temperature variations resulting from hurricanes, *Journal of Geophysical Research*, 73, 5105-5123, 1968.

Hellerman, S. and Rosenstein, M. Normal monthly wind stress over the world ocean with error estimates, *Journal of Physical Oceanography*, 13, 1093-1104, 1983.

Huang, Qi-zhou and Wang, Wen-zhi, Current characteristics of the South China Sea, in *Oceanology of China Seas*, edited by Z. Di, L. Yuan-Bo and Z. Cheng-Kui, 39-46, Kluwer, Boston, 1994.

Johnson, A., and Withee, G.W., Ocean data buoy measurements of Hurricane Eloise, *Marine Technological Society Journal*, 12, 14-21, 1978.

Jordon, C.L., On the influence of tropical cyclones on the sea surface temperature field, *Proceedings of the Symposium on Tropical Meteorology*, New Zealand Meteorology Service, Wellington, 614-622, 1964.

Ke, Pei-hui, Huang Qi-zhou, and Chen, Fu-pei, Hong, Hua-wen, and Feng, Shi-ying, Preliminary analysis of the continental shelf circulation driven by typhoon in the Northern South China Sea, *Chinese Journal of Atmospheric Sciences*, 11(4), 497-502, 1987.

Large, W.G. and Pond, S., Open ocean momentum flux measurements in moderate to strong winds, *Journal of Physical Oceanography*, 11, 324-336, 1981.

Levitus, S., Climatological atlas of the world ocean, NOAA Professional Paper, 13, U.S. Government Printing Office, Washington D.C., 173 pp, 1984.

Li, C., A numerical simulation of seasonal circulation in the South China Sea, Masters thesis, Naval Postgraduate School, Monterey, 74 pp, 1994.

McBride, J.L., Tropical cyclone formation, in *Global Perspectives of Tropical Cyclones*, edited by Elsberry, R.L., World meteorological Organization Technical Document No. 693, 63-102, 1995.

Mellor, G., Users guide for a three-dimensional, primitive equation, numerical ocean model, Princeton University, 34 pp, 1992.

Mellor, G. and Ezer, T., A Gulf Stream model and an altimetry assimilation scheme, *Journal of Geophysical Research*, 96, 8779-8795, 1991.

Miller, C.J., A study of the filling of hurricane Donna (1960) over land, *Monthly Weather Review*, 92, 389-406, 1964.

Neumann, C.J., Global overview, Chapter 1, *Global Guide to Tropical Cyclone Forecasting*, World Meteorological Organization, Geneva, Switzerland, 1.1-1.56, 1993.

NOAA NWS, Meteorology criteria for standard project hurricane and probable maximum hurricane wind fields, Gulf of Mexico and east coast of the United States, *NOAA Technical Report NWS 23*, U.S. Department of Commerce, Washington D.C., 320 pp, 1979.

Oey, L. and Chen, P., Frontal waves upstream of a diabatic blocking: a model study, *Journal of Geophysical Research*, 21, 1643-1663, 1991.

Price, J.F., Internal wave wake of a moving storm. Part I: Scales, energy budget and observations, *Journal of Physical Oceanography*, 13, 949-965, 1983.

Price, J.F., Sanford, T.B., Forristall, G.Z., Forced stage response to a moving hurricane, *Journal of Physical Oceanography*, 24, 233-260, 1994.

Price, J.F., Upper ocean response to a hurricane, *Journal of Physical Oceanography*, 11, 153-175, 1981.

Pudov, V.D., Varfolomeyev, A.A. and Fedorov, K.N., Vertical structure of the wake of a typhoon in the upper ocean. *Oceanology*, 18, 142-146, 1978.

Ramage, C.S., Monsoon Meteorology, Academic Press, New York, 1971.

SCSIO (South China Sea Institute of Oceanology, Academia Sinica), Integrated Investigation Report on Sea Area of the South China Sea (II), *Science Press, Bejing*, pp. 183-231 (in Chinese), 1985.

Shay, L.K. and Elsberry, R.L., Near-inertial ocean current response to Hurricane Frederic, *Journal of Physical Oceanography*, 17, 1249-1269, 1987.

Shay, L.K., Chang, S.W. and Elsberry, R.L., Free surface effects on the near-inertial ocean current response to a hurricane, *Journal of Physical Oceanography*, 20, 1405-1424, 1990.

Shay, L.K., Black, P.G., Mariano, A.J., Hawkins, J.D., and Elsberry, R.L., Upper ocean response to Hurricane Gilbert, *Journal of Geophysical Research*, 97, 20227-20248, 1992.

Soong, Y.S., Hu, J.H., Ho, C.R. and Niiler, P.P., Cold-core eddy detected in South China Sea, *EOS Trans. AGU*, 345-347, 1995.

Stramma, L., Cornillon, P., and Price, J.F., Satellite observations of sea surface cooling by hurricanes, *Journal of Geophysical Research*, 91, 5031-5035, 1986.

Su, Y.S. and Weng, X.C., Water masses in China Seas, in *Oceanology of China Seas*, edited by Z. Di, L. Yuan-Bo and Z. Cheng-Kui, 3-25, Kluwer, Boston, 1994.

Tseng, H.C., South China Sea warm-core and cool-core eddies detected from the Navy's Oceanographic Observation Data Set (MOODS), Masters thesis, Naval Postgraduate School, Monterey, 1995.

U.S. Naval Pacific Meteorology and Oceanography Center/Joint Typhoon Warning Center Guam (MPMOCW/JTWC), Forecaster's handbook, *NPMOCW/JTWC Instruction 3140.1*, 125 pp., 1991.

Whithee, G.W. and Johnson, A., Data report: Buoy observations during Hurricane Eloise (September 19 to October 11, 1975), U.S. Department of Commerce, NOAA, NSTL Station Mississippi, 21 pp, 1988.

Wyrtki, K., Scientific results of marine investigations of the South China Sea and the Gulf of Thailand 1959-1961, *Naga Report*, Vol 2&3, the University of California Scripps Institution of Oceanography, 1961.

APPENDIX. TROPICAL STORM ERINE (1996) DATA

Date	Time	Latitude N	Longitude E	Course	Speed (m/s)	R ₀ (m)	R _m (m)	Max Wind Speed (m/s)
4	0	5.3	133.4	277	7.6	827600	20000	10
4	6	5.5	132.2	279	6.1	827600	20000	10
4	12	6	131.2	296	5.6	872200	20000	13
4	18	6.6	130.2	301	6.1	872200	20000	13
5	0	7.4	129.2	308	6.6	829400	20000	13
5	6	8.1	128.3	308	5.6	768000	20000	13
5	12	8.7	127.2	298	6.1	768000	20000	15
5	18	9.1	126.3	294	5.1	768000	20000	15
6	0	9.5	125.3	292	5.6	786700	20000	18
6	6	10.3	124.7	323	5.1	786700	20000	18
6	12	11.2	123.8	315	6.6	842600	20000	20
6	18	11.7	122.8	297	5.6	865300	20000	23
7	0	12	121.3	281	7.6	865300	20000	23
7	6	12.1	120.2	275	5.6	865300	20000	25
7	12	12.3	119.8	297	2	857700	20000	25
7	18	12.5	119.5	304	2	846700	20000	25
8	0	12.7	119.3	315	1.5	836000	20000	25
8	6	13.4	118.9	330	4.1	801000	20000	25
8	12	14.1	118.6	337	4.1	875600	20000	25
8	18	14.8	118.4	344	3.6	875600	46200	23
9	0	16	118.3	355	6.1	875600	110700	20
9	6	17.3	117.7	336	7.1	736000	110700	18
9	12	17.9	117.7	0	3	717500	110700	18
9	18	18.5	117.8	8	3	717600	72000	20
10	0	19.2	117.9	7	3.6	717600	72000	23
10	6	19.6	118	13	2	717600	72000	23
10	12	19.8	118	0	1	717600	72000	23
10	18	20	118.1	25	1	717600	72000	23
11	0	20.2	118.1	0	1	717600	72000	23
11	6	19.8	118.5	136	2.5	717600	72000	23
11	12	19.4	119.2	121	4.1	717600	72000	23

Date	Time	Latitude N	Longitude E	Course	Speed (m/s)	R ₀ (m)	R _m (m)	Max Wind Speed (m/s)
11	18	19.3	120	97	4.1	717600	72000	23
12	0	19	120.6	117	3	717600	72000	23
12	6	18.4	121	147	3.6	640500	72000	18
12	12	17.6	121.1	173	4.1	640500	72000	18
12	18	16.7	120.4	216	5.6	640500	72000	18
13	0	16.2	119.3	244	6.1	640500	72000	18
13	6	15.8	118.2	249	5.6	640500	72000	18
13	12	15.5	117.3	250	4.6	649000	72000	18
13	18	14.9	116.2	240	6.1	669300	72000	18
14	0	14.1	115.1	233	6.6	854200	72000	20
14	6	13.6	113.9	246	6.6	854200	72000	20
14	12	13	112.8	240	6.1	861100	39600	20
14	18	12.3	112.3	214	4.6	796900	39600	18
15	0	11.4	111.6	217	5.6	796900	39600	18
15	6	11	110.8	242	4.6	796900	39600	18
15	12	10.8	110.1	253	3.6	796900	39600	18
15	18	10.4	109.2	245	5.1	796900	39600	15
16	0	10	108.3	245	5.1	796900	39600	15
16	6	9.7	107.3	253	5.1	796900	39600	15
16	12	9.4	106.3	253	5.1	796900	39600	15
16	18	9.4	105	270	6.6	750900	39600	13
17	0	9.5	103.9	275	5.6	744300	39600	13
17	6	9.6	102.8	275	5.6	737800	39600	13
17	12	9.8	101.8	281	5.1	725300	39600	13
17	18	10.1	100.8	286	5.1	707400	39600	13
18	0	10.4	100	290	4.1	690400	39600	13
18	6	10.7	99.2	290	4.1	560000	39600	10

INITIAL DISTRIBUTION LIST

	No. Copies
1. Defense Technical Information Center	2
8725 John J. Kingman Rd., Ste 0944	
Ft. Belvoir, VA 22060-6218	
2. Dudley Knox Library	2
Naval Postgraduate School	
411 Dyer Rd.	
Monterey, CA 93943-5101	
3. Superintendent	1
Attn: Chairman, Department of Oceanography (Code OC/BF)	
Naval Postgraduate School	
Monterey, CA 93943-5002	
4. Superintendent	1
Attn: Chairman, Department of Meteorology (Code MR/WX)	
Naval Postgraduate School	
Monterey, CA 93943-5002	
5. Superintendent	1
Attn: Professor Peter C. Chu (Code OC/CU)	
Naval Postgraduate School	
Monterey, CA 93943-5002	
6. Superintendent	1
Naval Research Laboratory	
7 Grace Hopper Avenue Stop 2	
Monterey, CA 93943-5502	
7. Chairman	1
Oceanography Department	
U.S. Naval Academy	
Annapolis, MD 21402	

8.	Dr Michael Fiaderio	1
	Office of Naval Research (Code 322OM)	
	800 N. Quincy Street	
	Arlington, Va 22217	
9.	Library	1
	Scripps Institution of Oceanography	
	P.O. Box 2367	
	La Jolla, Ca 92037	
10.	Dr. Martha Head	1
	Naval Oceanographic Office (Code N53)	
	Stennis Space Center, MS 39522	
11.	Dr. Mike Carron	1
	Naval Oceanographic Office (Code N3T)	
	Stennis Space Center, MS 39522	
12.	NOAA Library	1
	7600 Sand Point Way NE	
	Building 3	
	Seattle, WA 98115	
13.	Lieutenant Commander Joseph Veneziano	1
	COMSUBLANT REP	
	PSC 821 Box 111	
	FPO AE 09421	